



LUND UNIVERSITY

X-ray - Based Studies of Structural Dynamics in Solids and Liquids

Nüske, Ralf

2011

[Link to publication](#)

Citation for published version (APA):

Nüske, R. (2011). *X-ray - Based Studies of Structural Dynamics in Solids and Liquids*. [Doctoral Thesis (compilation), Atomic Physics].

Total number of authors:

1

General rights

Unless other specific re-use rights are stated the following general rights apply:

Copyright and moral rights for the publications made accessible in the public portal are retained by the authors and/or other copyright owners and it is a condition of accessing publications that users recognise and abide by the legal requirements associated with these rights.

- Users may download and print one copy of any publication from the public portal for the purpose of private study or research.
- You may not further distribute the material or use it for any profit-making activity or commercial gain
- You may freely distribute the URL identifying the publication in the public portal

Read more about Creative commons licenses: <https://creativecommons.org/licenses/>

Take down policy

If you believe that this document breaches copyright please contact us providing details, and we will remove access to the work immediately and investigate your claim.

LUND UNIVERSITY

PO Box 117
221 00 Lund
+46 46-222 00 00

X-ray - Based Studies of Structural Dynamics in Solids and Liquids

Ralf Nüske

Lund 2011

Division of Atomic Physics
Department of Physics
Faculty of Engineering, LTH
PO Box 118, SE-221 00 LUND
SWEDEN

Lund Reports on Atomic Physics, ISSN 0281-2762
LRAP-429
ISBN 978-91-7473-084-5

© Ralf Nüske 2011
Printed in Sweden by *Media-Tryck*, Lund.
February 2011

Populärvetenskaplig sammanfattning

Våglängden för röntgenstrålning är mycket kortare än den för synligt ljus. I själva verket är den jämförbar med avståndet mellan atomer i fasta material, vilket är i storleksordningen en tiondel nanometer. Genom att använda ljus med så kort våglängd är det möjligt att studera materials struktur på atomär nivå. Spridning av röntgenstrålar har utvecklats till ett ovärderligt verktyg för att analysera bland annat gitterstrukturen hos kristaller, såväl som strukturen hos stora biologiska molekyler. Många av ett materials egenskaper ges av dess interna struktur.

Tidsupplöst röntgenspridning har visat sig vara en kraftfull metod för att studera ändringar i strukturen hos ett material på atom-nivå. En mångfald av processer kan studeras: från fasövergångar i material till vibrationer i kristallgitter och kemiska reaktionsvägar. Målet med tidsupplösta studier är att följa dessa processer i realtid.

Tidsskalan för ändringar av strukturen varierar drastiskt beroende på mekanismen. Strukturförändringar inom en enkel cell tar typiskt 100 fs. Andra viktiga strukturändringar som omfattar större grupperingar av molekyler sker på en tidsskala av pikosekunder till nanosekunder. För att starta ändringar av strukturen kan olika mekanismer användas. Laserpulser kortare än 100 fs kan produceras rutinmässigt och används för att initiera ändringar av strukturen i material. Alternativt kan korta elektriska pulser användas för att starta strukturändringar i piezoelektriska material.

I detta arbete har framför allt experimentella studier genomförts för att förbättra förståelsen av strukturförändringar i material. Vi har studerat dynamiken på pikosekundnivå kopplad till smältning och återkristallisering av en halvledare, akustisk och termisk respons hos laserexciterade fasta material, och dynamiken i strukturen hos ett piezoelektriskt material.

En kortfattad beskrivning av den teoretiska bakgrunden, de experimentella teknikerna och den nödvändiga instrumenteringen ges. Detta följs av en sammanställning av publikationerna detta arbete har resulterat i.

Abstract

The wavelength of x-ray radiation is much shorter than that of visible light. In fact, it is comparable to the distances between atoms in solids, which is on the order of one tenth of a nanometer. Using light of such a short wavelength, it is possible to study the structure of materials on the atom level. Scattering of x-rays has been developed into an invaluable tool to analyze various characteristics of matter, from the lattice structure of crystals to the structure of large biological molecules. In this way, we found that many of the properties of materials depend on their internal structure.

To learn about changes in the structure of materials on the atom-level, time resolved x-ray scattering has proven a powerful technique. A wide variety of processes can be studied: from phase transitions in materials to vibrations in crystal lattices and pathways of chemical reactions. The aim of time-resolved studies is to follow these processes in real time.

The timescale for changes in structure varies considerably depending on the underlying mechanism. Processes involving neighboring atoms typically take about 100 fs. Structure changes involving large groups of atoms or molecules occur on a timescale of picoseconds to nanoseconds. Different mechanisms can be used to trigger changes in structure. Laser pulses with a duration of less than 100 fs can be produced routinely and are used to initiate ultrafast changes in the structure. Alternatively, short electrical pulses can be used to trigger structural changes in piezo-electric materials.

In this work, the main focus has been on experimental studies in order to deepen the understanding of structural changes in matter. The picosecond dynamics involved in the melting and recrystallization of a semiconductor, acoustic and thermal response of laser-excited solids, and the dynamics in the structure of a piezo-electric material have been studied. Additionally, instrumentation required for time-resolved x-ray scattering experiments has been developed.

List of publications

This thesis is based on the following papers. They will be referred to in the text by their roman numbers.

- I** R. Nüske, C. von Korff-Schmising, A. Jurgilaitis, H. Enquist, H. Navirian, P. Sondhauss, J. Larsson, “Time-resolved x-ray scattering from laser-molten indium antimonide”, *Rev. Sci. Instrum.*, vol. 81, p. 013106, 2010
- II** H. Navirian, H. Enquist, R. Nüske, A. Jurgilaitis, C. von Korff-Schmising, P. Sondhauss, J. Larsson, “Acoustically driven ferroelastic domain switching observed by time-resolved x-ray diffraction”, *Phys. Rev. B*, vol. 81, p. 024113, 2010
- III** A. Jurgilaitis, R. Nüske, H. Enquist, H. Navirian, P. Sondhauss, J. Larsson, “X-ray diffraction from the ripple structures created by femtosecond laser pulses”, *Appl. Phys. A*, vol. 100, p. 105-112, 2010
- IV** H. Enquist, H. Navirian, R. Nüske, C. von Korff-Schmising, A. Jurgilaitis, M. Herzog, M. Bargheer, P. Sondhauss, J. Larsson, “Subpicosecond hard x-ray streak camera using single-photon counting”, *Opt. Lett.*, vol. 35, p. 3219, 2010
- V** R. Nüske, A. Jurgilaitis, S. Dastjani Farahani, M. Harb, C. von Korff-Schmising, H. Enquist, J. Gaudin, M. Störmer, L. Guerin, M. Wulff, and J. Larsson “Picosecond time-resolved x-ray reflectivity of an amorphous carbon thin film”, *to appear in Applied Physics Letters (2011)*
- VI** R. Nüske, A. Jurgilaitis, H. Enquist, M. Harb, Y. Fang, U. Håkanson, and J. Larsson, “Formation of nanoscale diamond by femtosecond laser-driven shock”, *manuscript in preparation*
- VII** M. Harb, H. Enquist, A. Jurgilaitis, R. Nüske, C. v. Korff-Schmising, J. Gaudin, S. L. Johnson, C. J. Milne, P. Beaud, E. Vorobeva, A. Caviezel, S. Mariager, G. Ingold, and J. Larsson “Picosecond dynamics of laser-induced strains in graphite”, *submitted*
- VIII** J. Gaudin, B. Keitel, A. Jurgilaitis, R. Nüske, L. Guerin, J. Larsson, K. Mann, B. Schäfer, K. Tiedtke, A. Trapp, Th. Tschentscher, F. Yang, M. Wulff, H. Sinn and B. Flöter, “Time-resolved investigation of nanometre scale deformations induced by a high flux x-ray beam”, *manuscript in preparation*

Acknowledgments

I would like to express my gratitude to all the people who supported me throughout this work. I was part of the Ultrafast X-ray Science group at the Atomic Physics Division of the Engineering Faculty at Lund University, but most of the work was done at the MAX-Lab synchrotron facility.

Foremost, I would like to thank my supervisor, Jörgen Larsson, who made it possible for me to work in this exciting field of science and welcomed me in his group. His support and guidance has helped me tremendously in the last four years.

I would like to express my gratitude to my co-supervisor Peter Sondhaus. He has always been open to inspiring discussions. I am especially grateful, that he fully continued to support me, even though he is now very involved in the planning for the MAX-IV project.

Experimental physics is a team effort, and this was truly the case in our group. I thank the members of the Ultrafast X-ray Science group for the inspiring work environment and being good friends. These are Clemens, Maher, Henrik, Hengameh, and Andrius. Special thanks go to Henrik and Maher for sharing their MATLAB expertise. Henrik helped me translating Swedish when I needed it.

I am grateful for the support I got from the personnel both at Atomic Physics and MAX-Lab. Minna helped me many times with paperwork. Special thanks go to Anders and Kurt at MAX-Lab for being very supportive whenever we needed technical help at the beamline.

I thank our collaborators at the SLS and at ESRF, especially Michael Wulff and Laurent Guerin.

The MAXLAS network has provided support for me in my first three years, for which I am grateful to. Furthermore, the MAXLAS collaboration has been successful to provide a platform for fruitful scientific discussions and good friends at the same time. I want to mention other members of the network: Nino, Marko, Jens, Jörg and Guillaume. Working in related fields of science and having similar interests has been a great opportunity for exchange of ideas and knowledge. I am thankful for this and also for just having a good time together.

At last, I want to thank my family and friends in Dresden for keeping up with me and being supportive the whole time I am away.

List of acronyms and abbreviations

CCD	charge coupled device
ERL	energy recovering linac
ESRF	European Synchrotron Radiation Facility
FEL	free electron laser
FROG	frequency-resolved optical gating
InSb	indium antimonide
IR	infrared
KDP	potassium dihydrogen phosphate
linac	linear accelerator
MCP	multi channel plate
RDF	radial distribution function
rms	root mean square
SLS	Swiss Light Source
SPPS	Sub-Picosecond Pulse Source
UV	ultraviolet

Contents

Populärvetenskaplig sammanfattning	iii
Abstract	v
List of publications	vii
Acknowledgments	ix
List of acronyms and abbreviations	xi
Contents	xiii
I Overview	1
1 Introduction	3
2 X-ray diffraction	5
2.1 Introduction	5
2.2 X-ray scattering	5
2.3 Kinematic theory of x-ray diffraction	6
2.4 Rocking curves	9
2.5 Bragg reflections from asymmetrically cut crystals	9
2.6 X-ray scattering from non-crystalline matter	10
2.7 Specular x-ray reflectivity	12
3 Time-resolved x-ray scattering	17
3.1 Laser-matter interaction	17
3.2 The Thomsen model	18
3.3 Optical phonons in bismuth	20
3.4 Non-thermal melting of InSb	21
3.5 X-ray diffraction from laser-induced ripple-structured surfaces . .	24
3.6 Ferroelectric phase transitions in KDP	25

3.7	Time-resolved specular x-ray reflectivity of an amorphous carbon thin film	26
4	Ultrafast x-ray sources	29
4.1	Introduction	29
4.2	Storage ring based x-ray sources	29
4.3	Linac-based x-ray sources	31
4.4	Laser-based x-ray sources	34
5	Beamline D611	35
5.1	Introduction	35
5.2	The x-ray optics	36
5.3	Laser system	39
5.4	Setups for time-resolved measurements	41
5.5	A setup for powder diffraction	45
6	Outlook	47
	References	49
	Comments on my contributions	57
II	Papers	61
III	Appendix - Matlab scripts	155
	Matlab scripts	157

Part I

Overview

Chapter 1

Introduction

X-ray diffraction has developed into a standard tool for the investigation of the structure of a wide variety of materials on the atomic scale. This is of interest as the optical, mechanical, and electrical properties are determined by the internal atomic structure of the material.

The aim of time-resolved x-ray diffraction is to investigate the evolution of the structure in real-time. The structural dynamics inferred from such measurements helps us to understand the mechanisms behind the structural changes and the resulting material properties.

The ultimate timescale of structure dynamics is set by the period of lattice vibrations, which is about 100 fs. The term *ultrafast x-ray diffraction* is used for studies of structural changes on that timescale. An x-ray detector with sufficient time-resolution to perform such experiments is the x-ray streak camera. New x-ray sources have been developed recently, such as free x-ray electron lasers, slicing synchrotron sources, and laser based x-ray sources. X-ray pulse durations of below 100 fs can be achieved, thus time-resolved x-ray diffraction measurements are possible by making use of the short duration of the pulses. An ultrafast laser with comparable pulse duration is used to initiate the change in structure, while the x-ray pulse serves as a probe.

In work presented in this thesis, time-resolved x-ray scattering techniques have been used to study processes with dynamics from the femtosecond till microsecond timescale.

Structural dynamics on the pico- and nanosecond timescale plays a key role, in processes such as, thermal melting and re-crystallization of solids, and the dynamics of strain induced by laser pulses in solids. It has been an aim to control the structure of a material by light or external fields. In this work, ferroelastic switching between two ferroelectric domains, triggered by an electrical pulse, could be followed. In another example, a short laser pulse was used to initiate a shock-wave mediated phase transition from hexagonal graphite to cubic diamond. The intermediate phase rhombohedral graphite has been observed using x-ray diffraction.

Chapter 2 introduces the background of x-ray diffraction. The theory of x-ray diffraction and scattering is discussed briefly.

In chapter 3, the experiments conducted in this work are described. Phase transi-

tions, such as melting and ferroelectric switching, lattice vibrations, and the dynamics of strain in solids are the subjects of interest. Models, which have been developed in this work, are discussed, describing the underlying mechanisms of the structural dynamics observed in the experiments.

In chapter 4, relevant x-ray sources are described briefly. The properties of the generated x-ray radiation from these sources are important parameters for the type of studies that can be conducted.

Chapter 5 introduces the beamline D611 at MAX-Lab, where most of the experiments were carried out. Source parameters, the instrumentation and the range of possible studies are explained. Beamline instrumentation, which has been developed in this work, is discussed in detail.

Chapter 2

X-ray diffraction

2.1 Introduction

X-ray diffraction is a widely used technique for the study of the atomic structure of materials. In this work, several different techniques based on x-ray scattering and diffraction were used for structural analysis. In this chapter, the background is presented, and the techniques used are introduced.

2.2 X-ray scattering

The interaction of x-ray photons with matter can be described in terms of several fundamental processes. As the photon energy of x-rays is not sufficient to interact with the nuclei of the atoms in the scattering medium, only the electrons need to be considered. The x-ray photon can be either absorbed or scattered. Elastic scattering, where the photon energy is unchanged, is called Thomson-scattering. Inelastic scattering is accompanied by a change in photon energy, and is therefore also called incoherent scattering. The main mechanism for inelastic scattering is Compton-scattering. The probability of these processes occurring depends mainly on the scattering medium and the x-ray energy. For silicon, inelastic scattering becomes dominant above an x-ray energy of about 30 keV, whereas in carbon, the threshold is at 18 keV [1].

In classical theory, elastic scattering from a single electron is described by the Thomson scattering equation for polarized x-rays (gaussian-type cgs units are used):

$$I_e = I_0 \frac{e^4}{m^2 c^4 R^2} \cos^2 \phi = I_0 \left(\frac{r_e \cos \phi}{R} \right)^2 \quad (2.1)$$

where ϕ is the angle between the incident and scattered beam polarization vector, r_e the classical electron radius, and R the distance from the scattering center [2]. As the x-ray wavelength is comparable to the size of the electron distribution in a typical atom, the spatial distribution of electrons in the atom must be taken into account

for. With the electron density ρ , we can introduce the atom form factor:

$$f_{\text{a}} = \int_{\text{atom}} \rho(\vec{r}) \cdot e^{i\vec{q}\cdot\vec{r}} d^3r \quad (2.2)$$

We define $\vec{q} = \vec{k} - \vec{k}_0$ as the difference between the scattered wave vector \vec{k} and the incident wave vector \vec{k}_0 as illustrated in Figure 2.1.

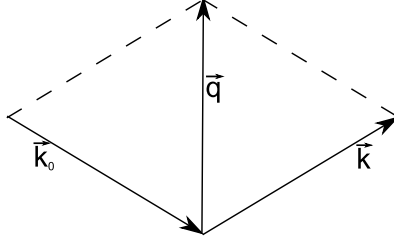


Figure 2.1: Scattering geometry. Relation between wave vectors of incident and scattered wave vectors \vec{k}_0 and \vec{k} and the scattering vector \vec{q} .

The scattering intensity from a single atom can be described as:

$$I_{\text{atom}} = I_e |f_{\text{a}}|^2 \quad (2.3)$$

2.3 Kinematic theory of x-ray diffraction

The kinematic theory of x-ray diffraction gives accurate results whenever multiple scattering and extinction of the incident x-ray beam can be neglected. For strongly scattering media, such as extended perfect crystals, dynamical x-ray diffraction theory gives better results [3]. Kinematic theory can still be applied in cases of small crystals, weakly scattering media, and systems with only local order.

For an arbitrary sample consisting of N atoms with the atom form factor f_n we can derive the scattering factor f :

$$f = \sum_{n=1}^N f_n \cdot e^{i\vec{q}\cdot\vec{r}_n} \quad (2.4)$$

The intensity of the reflected x-ray beam becomes:

$$I = I_e |f|^2 \quad (2.5)$$

For a small crystal with crystal axes $\vec{a}_1, \vec{a}_2, \vec{a}_3$, and $N = N_1 \cdot N_2 \cdot N_3$ unit cells, the scattering factor can be written as:

$$f = \sum_m f_m \cdot e^{i\vec{q}\cdot\vec{r}_m} \sum_{n_1=1}^{N_1} e^{i\vec{q}\cdot n_1 \vec{a}_1} \sum_{n_2=1}^{N_2} e^{i\vec{q}\cdot n_2 \vec{a}_2} \sum_{n_3=1}^{N_3} e^{i\vec{q}\cdot n_3 \vec{a}_3} \quad (2.6)$$

The first sum involves the atoms within the unit cell at positions \vec{r}_m . This term is specific for the crystal structure and is therefore called the structure factor F . The other terms describe the periodicity of the lattice and generally have the form of a geometric series. Therefore, the scattered intensity can be written as:

$$I = I_e |F|^2 \prod_{i=1}^3 \frac{\sin^2 \left(\frac{1}{2} N_i \vec{q} \cdot \vec{a}_i \right)}{\sin^2 \left(\frac{1}{2} \vec{q} \cdot \vec{a}_i \right)} \quad (2.7)$$

The width of the peaks is inversely proportional to the number of unit cells N . When the structure factor F becomes zero, the intensity of the scattered wave vanishes. These cases are structure specific and are called forbidden reflections. The scattered intensity has maxima when the following conditions are fulfilled:

$$\vec{q} \cdot \vec{a}_1 = 2\pi \cdot h \quad \vec{q} \cdot \vec{a}_2 = 2\pi \cdot k \quad \vec{q} \cdot \vec{a}_3 = 2\pi \cdot l \quad (2.8)$$

where h, k, l are integer numbers. Equation 2.8 is known as Laue equation. By introducing the reciprocal lattice:

$$\vec{b}_i = 2\pi \frac{\vec{a}_j \times \vec{a}_k}{\vec{a}_i \cdot (\vec{a}_j \times \vec{a}_k)}$$

the Laue equations can be rewritten as:

$$\vec{q} = \vec{G}_{hkl} \quad \vec{G}_{hkl} = h\vec{b}_1 + k\vec{b}_2 + l\vec{b}_3 \quad (2.9)$$

where \vec{G}_{hkl} is a vector in the reciprocal space of the crystal lattice.

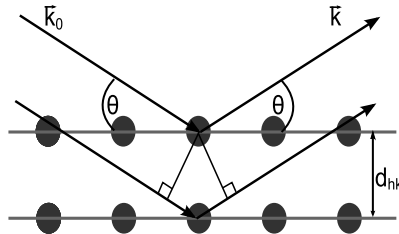


Figure 2.2: Bragg's law. Diffraction from crystallographic planes (hkl) at the Bragg angle θ . The lattice plane spacing is d_{hkl} , and the incident and scattered wave vectors are \vec{k}_0 and \vec{k}

We now introduce crystallographic planes (hkl). These are a set of parallel planes, one of which passes through the origin and another at the points \vec{a}_1/h , \vec{a}_2/k , and \vec{a}_3/l . The spacing between these planes is related to the magnitude of the corresponding reciprocal lattice vector:

$$d_{hkl} = \frac{2\pi}{|\vec{G}_{hkl}|}$$

Using the Laue equation, we can rewrite this as:

$$|\vec{q}| = \frac{4\pi \sin \theta}{\lambda} = \frac{2\pi}{d_{hkl}}$$

This is equivalent to Bragg's law:

$$2 d_{hkl} \sin \theta = \lambda \quad (2.10)$$

2.3.1 The Debye-Waller model

The intensity of the scattered x-ray beam as described in Equation 2.7 assumes a perfectly periodic crystal. Here, we introduce the Debye-Waller model, which describes the influence of statistic fluctuations on the intensity of the diffracted x-ray beam. This concept can be used for a variety of parameters that are subject to statistical fluctuations. It was first applied to describe the influence of the thermal motion of atoms on the intensity of the diffracted x-ray beam. It can also be applied to model the effect of sample surface roughness on specular x-ray reflection as described in section 2.7. This was used in Paper V .

Here, the Debye-Waller model for the thermal motion of atoms around the equilibrium position in a lattice is explained. Atoms oscillate around an average position with an amplitude depending on their thermal kinetic energy. An atom will be displaced by a distance $\vec{\delta}$ from its average position \vec{r} at a given time. The equation describing the intensity of the scattered wave is modified to:

$$I = I_e \sum_n f_n e^{i\vec{q}\cdot(\vec{r}_n + \vec{\delta}_n)} \sum_m f_m^* e^{-i\vec{q}\cdot(\vec{r}_m + \vec{\delta}_m)} \quad (2.11)$$

Introducing u_n as the component of $\vec{\delta}_n$ in the direction \vec{q} , we can express the average as:

$$I = I_e \sum_{n,m} f_n f_m^* e^{i\vec{q}\cdot(\vec{r}_n - \vec{r}_m)} \langle e^{iq(u_n - u_m)} \rangle$$

The Debye temperature factor can be expressed as:

$$e^{-2M} = e^{-q^2 \langle u^2 \rangle}$$

Assuming only one kind of atom and a gaussian distribution of $(u_n - u_m)$, the scattered intensity becomes:

$$\begin{aligned} I &= I_e \sum_{n,m} |f|^2 e^{-2M} e^{i\vec{q}\cdot(\vec{r}_n - \vec{r}_m)} \\ &+ I_e \sum_{n,m} |f|^2 e^{-2M} e^{i\vec{q}\cdot(\vec{r}_n - \vec{r}_m)} \left(e^{q^2 \langle u_n u_m \rangle} - 1 \right) \end{aligned} \quad (2.12)$$

The first term is the sharp reflection corresponding to the long range order in the crystal which is reduced in intensity by the Debye temperature factor. Since the correlation $\langle u_n u_m \rangle$ vanishes at large distances between atoms, the second term represents the diffuse contribution, called temperature diffuse scattering.

2.4 Rocking curves

A rocking curve is recorded by measuring the x-ray reflectivity as a function of the angle θ as depicted in Figure 2.2. Typical crystal properties, such as lattice constants and grain sizes, can be inferred from the position and shape of the rocking curve. An alternative to this technique, which gives equivalent information, is to instead scan the x-ray energy, while keeping the angle θ constant. This is a technique commonly used at synchrotron x-ray sources, since a broad range of x-ray energies is available. This method is used routinely at the D611 beamline at MAX-Lab. The sample and detector geometry can be kept fixed during an energy scan. The width of the rocking curve is related to the width of the equivalent energy scan:

$$\frac{\delta\theta}{\tan\theta} = \frac{\delta E}{E} \quad (2.13)$$

2.5 Bragg reflections from asymmetrically cut crystals

When the reflecting planes are not parallel to the crystal surface, this is called asymmetric diffraction geometry. This is illustrated in Figure 2.3. The angle at which the crystal is cut with respect to the diffracting planes is referred to as the asymmetry angle, ϕ . When the crystal surface normal and the incident and diffracted beams are in the same plane, the diffraction geometry is referred to as coplanar.

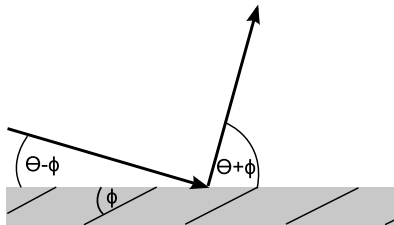


Figure 2.3: Asymmetric coplanar diffraction geometry with Bragg angle θ , asymmetry angle ϕ , and incidence angle $\theta - \phi$.

The x-ray penetration depth is determined by the absorption and extinction length of the x-ray beam and the asymmetry angle. Absorption lengths can be found in tables [1]. Extinction is important near the peak of strong Bragg reflections. The x-ray penetration depth due to absorption in the coplanar geometry can be calculated from:

$$d = \frac{l(\cos^2\phi - \cos^2\theta)}{2\cos\phi\sin\theta} \quad (2.14)$$

where l is the absorption length, θ the Bragg angle, and ϕ the asymmetry angle.

Typical values of x-ray absorption lengths in solids are on the order of a few μm . When the value of the asymmetry angle is close to, but smaller than, the Bragg angle, the incidence angle becomes small. This geometry is referred to as grazing incidence.

At grazing incidence, the x-ray penetration depth is much smaller than the x-ray absorption length.

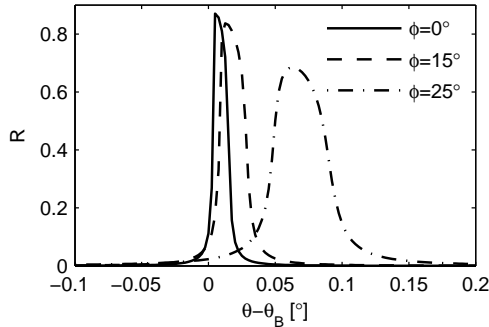


Figure 2.4: Rocking curves for InSb at 3500 eV at incidence angles of 28° (solid line), 13° (dashed line), and 3° (dotted line). Data from “Sergey Stepanov’s X-ray Server” [4].

Rocking curves for InSb with different asymmetry/incidence angles calculated using dynamic diffraction theory are shown in Figure 2.4. With decreasing incidence angle, the bandwidth of the rocking curve is increased. This is due to the reduced x-ray penetration length. Furthermore, there is an angular shift caused by refraction at the sample surface.

For an indium antimonide (InSb) crystal and an x-ray energy of 7500 eV, the absorption length is $4.2 \mu\text{m}$, whereas the x-ray penetration depth at an incidence angle of 0.9° is as small as 90 nm. This is similar to the penetration length of an infrared beam at 800 nm wavelength. The use of asymmetrically cut crystals allows the penetration depth of the x-ray beam to be tailored. For an infrared pump - x-ray probe experiment, this geometry allows a good overlap of the pumped and the probed fraction of a bulk crystal to be achieved.

2.6 X-ray scattering from non-crystalline matter

X-ray scattering is a useful tool not only for studying the structure of samples with long-range order and a high degree of orientation, such as bulk crystals, thin crystalline films and crystal powders, but also dense gases, liquids, molecules in solution, and amorphous solids. Although these samples lack long-range order and have no preferred internal orientation, they often retain a short-range or local order, which can be determined by x-ray scattering.

As a starting point, Equation 2.5 is used, which describes the scattered x-ray intensity of an arbitrary sample with atoms at position \vec{r}_n :

$$I = I_e \sum_{n,m} f_n f_m^* e^{i\vec{q} \cdot (\vec{r}_n - \vec{r}_m)} \quad (2.15)$$

From now on, we assume only one kind of atom with an atom scattering factor f . By introducing the difference vector $\vec{r}_{nm} = \vec{r}_n - \vec{r}_m$, and by separating the terms with $n = m$ in the double sum, the intensity is obtained:

$$I = I_e N f^2 + I_e \sum_n f^2 \sum_{m \neq n} e^{i\vec{q} \cdot \vec{r}_{nm}}$$

Introducing a density function $\rho_n(\vec{r}_{nm})$ such that $\rho_n dV$ is the number of atoms in the volume element dV at position \vec{r}_{nm} with respect to atom n , we can write:

$$I = I_e N f^2 + I_e \sum_n f^2 \int_{\text{sample}} \rho_n(\vec{r}_{nm}) e^{i\vec{q} \cdot \vec{r}_{nm}} dV$$

Assuming no preferred orientation in the sample, homogeneity, and short range order, the expression can be rewritten as [2]:

$$\frac{I}{I_e} = N f^2 + N f^2 \int_0^\infty 4\pi r^2 (\rho(r) - \rho_a) \frac{\sin(qr)}{qr} dr \quad (2.16)$$

Here, the value N is the total number of atoms of the sample, and ρ_a is the average density in the sample.

Since correlations of distances between atom are short range (typically less than a few atom diameter), the x-ray intensity will be distributed diffusely in space. The scattering angle 2θ is related to the absolute momentum transfer by:

$$q = \frac{4\pi \sin \theta}{\lambda}$$

The scattered intensity $I(q)$ is an observable quantity in the x-ray scattering experiment. It is common to introduce the abbreviation:

$$i(q) = \frac{I(q)/I_e - N f^2}{N f^2}$$

To calculate $i(q)$ from the scattered x-ray intensity, careful normalization and tabulated atomic scattering factors f are needed. If inelastic scattering, such as Compton scattering, makes a relevant contribution to the scattering signal, it should be subtracted. The Compton scattering cross sections are tabulated values [1]. From Equation 2.16 we can see that for large q :

$$\begin{aligned} \lim_{q \rightarrow \infty} \frac{I(q)}{I_e} &= N f^2 \\ \lim_{q \rightarrow \infty} i(q) &= 0 \end{aligned}$$

The parameter N , describing the number of scattering centers in the probed volume, has to be chosen, such that $i(q)$ converges to zero for large q . Equation 2.16 can then be rewritten as:

$$q i(q) = 4\pi \int_0^\infty r (\rho(r) - \rho_a) \sin(qr) dr \quad (2.17)$$

The equation has the form of the Fourier integral. Inverting it gives the following equation:

$$r(\rho(r) - \rho_a) = \frac{1}{2\pi^2} \int_0^\infty q i(q) \sin(qr) dq$$

The average number of atoms between distances r and $r + dr$ from the center of an atom in the sample can be derived as:

$$4\pi r^2 \rho(r) = 4\pi r^2 \rho_a + \frac{2r}{\pi} \int_0^\infty q i(q) \sin(qr) dq \quad (2.18)$$

This expression is called the Radial Distribution Function (RDF) [5]. It is evident, that in order to calculate the RDF, measurements of x-ray scattering over a range in q are required. A practical approach is to measure the diffuse scattered x-ray intensity with a large two-dimensional detector, such as an x-ray charge-coupled device (CCD). $I(q)$ can be derived from the radial distribution of the intensity. The x-ray wavelength and the maximum scattering angle that can be detected in the CCD define the limits for the range of q .

Non-physical termination satellites in the RDF occur when $i(q)$ has not converged at the truncation limit q_{\max} . The spatial resolution of the RDF is determined by the range in q :

$$\Delta r = \frac{2\pi}{q_{\max}}$$

The prevalence of atoms at certain distances from an atom center creates peaks in the RDF. These distances can be interpreted as nearest-neighbor distances. From an analysis of the peak heights, the number of atoms at the individual next-neighbor distances can be determined. These values are referred to as coordination numbers.

2.7 Specular x-ray reflectivity

Specular X-ray reflectometry is a surface sensitive method used to determine a multitude of sample parameters for thin films as well as bulk samples. Among others, the densities, surface roughnesses, and the topology of multilayered structures can be studied. The refractive index for electromagnetic radiation in the x-ray energy range is close to unity in all materials since the frequency is above that of most electronic resonances. Using the complex atom scattering factor, $f(0) = f_1 + if_2$, and the atom density in the material, ρ_a , we can write:

$$\begin{aligned} n &= 1 - \delta - i\beta \\ &= 1 - \frac{r_e}{2\pi} \lambda^2 \rho_a (f_1 + if_2) \end{aligned} \quad (2.19)$$

The real part of the refractive index is less than unity. However, the difference, δ , is small, e.g. $\delta = 3.1 \cdot 10^{-6}$ in silicon at an x-ray wavelength of $\lambda = 0.1$ nm. Since the refractive index is higher in vacuum, total external reflection from vacuum to a sample surface is possible.

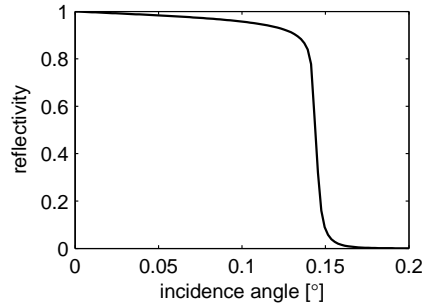


Figure 2.5: X-ray specular reflectivity of silicon at $\lambda = 0.1$ nm, no surface roughness assumed. The critical angle is $\alpha_c = 0.14^\circ$.

The change in angle of the x-ray beam crossing a sample surface can be described using Snell's law. The critical incidence angle, α_c , for total external reflection is defined such that the refracted beam would propagate along the surface:

$$\alpha_c = \sqrt{2\delta} \quad (2.20)$$

At an x-ray wavelength of 0.1 nm, the critical angle for silicon is $\alpha_c = 0.14^\circ$. Figure 2.5 illustrates the specular reflectivity of bulk silicon assuming a perfectly even interface to vacuum. Below the critical angle, the reflectivity is close to unity, whereas at α_c , the reflectivity falls abruptly. Above the critical angle, the x-ray beam propagates into the material instead of being reflected.

2.7.1 Modelling x-ray reflectivity from multi-layer structures

In the following, the model for specular x-ray reflectivity of multi-layers, which is based on Abelès matrix formalism [6], is derived. It allows to calculate the x-ray specular reflectivity of a multilayer structure. This model is based on the same principles as Darwin's matrix-based dynamic x-ray diffraction model [7].

The reflectivity of a multi-layered structure depends on material parameter such as density, interface-roughness, and layer thicknesses. Using experimental data, the model can be used to derive these important parameters. In Paper V, we report on the specular x-ray reflectivity of a thin film of amorphous carbon on a silicon substrate. Information about the thin film morphology was extracted from the measurements. The model, which is explained in the following section, was used for this. The description is kept very general here. It can be applied to more complex multi-layer samples.

First, we consider the interface between two layers with different refractive indices. Due to reflection at interfaces, two waves are present. One wave propagates towards the interface, and the other away from the interface. The electric field components of

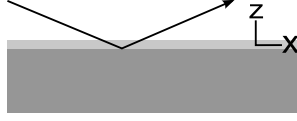


Figure 2.6: Coordinate system used in derivation of x-ray specular reflectivity from multi-layers

the two waves in layer j can be expressed as:

$$\begin{aligned} E_j(x, z) &= \left(A_j^\uparrow e^{ik_{j,z}z} + A_j^\downarrow e^{-ik_{j,z}z} \right) e^{ik_{j,x}x - i\omega t} \\ &= \left(U_j^\uparrow(z) + U_j^\downarrow(z) \right) e^{ik_{j,x}x - i\omega t} \end{aligned} \quad (2.21)$$

In layer j , A_j^\uparrow is the amplitude of the wave propagating towards increasing z , while A_j^\downarrow is the wave propagating in the opposite direction. The parameters $k_{j,x}$ and $k_{j,z}$ are the components of the wavevector in the x and z directions inside layer j . At an interface between layers j and $j+1$ with different dielectric constants, the conditions of continuity must be fulfilled:

$$\begin{aligned} U_j^\uparrow(z) + U_j^\downarrow(z) &= U_{j+1}^\uparrow(z) + U_{j+1}^\downarrow(z) \\ k_{j,z} \left(U_j^\uparrow(z) - U_j^\downarrow(z) \right) &= k_{j+1,z} \left(U_{j+1}^\uparrow(z) - U_{j+1}^\downarrow(z) \right) \end{aligned}$$

This can be rewritten in matrix notation:

$$\begin{pmatrix} U_j^\uparrow(z) \\ U_j^\downarrow(z) \end{pmatrix} = \begin{pmatrix} p_{j,j+1} & m_{j,j+1} \\ m_{j,j+1} & p_{j,j+1} \end{pmatrix} \begin{pmatrix} U_{j+1}^\uparrow(z) \\ U_{j+1}^\downarrow(z) \end{pmatrix} = \mathbf{R}_{j,j+1} \begin{pmatrix} U_{j+1}^\uparrow(z) \\ U_{j+1}^\downarrow(z) \end{pmatrix}$$

Here, we have introduced the Matrix $\mathbf{R}_{j,j+1}$, which describes the reflection at the $j, j+1$ interface. The matrix elements p and m are:

$$\begin{aligned} p_{j,j+1} &= \frac{k_{j,z} + k_{j+1,z}}{2k_{j,z}} \\ m_{j,j+1} &= \frac{k_{j,z} - k_{j+1,z}}{2k_{j,z}} \end{aligned}$$

which is equivalent to Fresnel's equations. The values of $k_{j,z}$ and $k_{j+1,z}$ at the interface between layers j and $j+1$ are calculated using Snell's law. The result depends on the refractive index in these layers. As we have seen in Equation 2.19, the refractive index for x-rays is related to the type of atoms in the layer j and its density ρ_j .

Surface roughness reduces the reflectivity at the interface:

$$\mathbf{R}_{j,j+1}^{\text{rough}} = \mathbf{R}_{j,j+1}^{\text{flat}} \cdot e^{-k_{j,z} \cdot k_{j+1,z} \cdot \sigma_{j,j+1}^2}$$

The value $\sigma_{j,j+1}$ is defined as the root-mean-square (rms) roughness of the interface between layers j and $j+1$:

$$\sigma_{j,j+1}^2 = \langle (z_{j,j+1}(x, y) - \bar{z}_{j,j+1})^2 \rangle$$

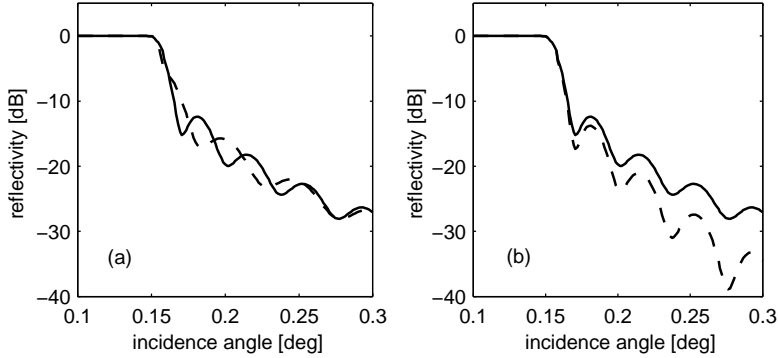


Figure 2.7: Calculated x-ray reflectivity of a thin-film system consisting of one layer of amorphous carbon on a silicon substrate. The left pane (a) compares the reflectivity for a 45 nm film (solid line) and a 35 nm film (dashed line). The right pane (b) illustrates the effect of surface roughness on the reflectivity of the 45 nm thin film: perfectly flat surface (solid line) compared to a surface roughness of 2 nm rms (dashed line).

The effect of surface roughness is described accurately provided that the lateral dimensions of the roughness features are considerably smaller than the size of the x-ray beam. The Debye-Waller type model can be applied, as it is described in Section 2.3.1.

Propagation through layer j with thickness t_j can be described in the same matrix formalism. The phases of the two plane waves traveling in the layer j change according to the layer thickness, t_j , and the wavevector, $k_{z,j}$. Absorption can be accounted for by including the imaginary part of the wavevector $k_{z,j}$ using the imaginary part of the refractive index in Equation 2.19. We introduce the propagation matrix \mathbf{T}_j :

$$\begin{pmatrix} U_j^\uparrow(z_j) \\ U_j^\downarrow(z_j) \end{pmatrix} = \begin{pmatrix} e^{ik_{z,j}t_j} & 0 \\ 0 & e^{-ik_{z,j}t_j} \end{pmatrix} \begin{pmatrix} U_{j+1}^\uparrow(z_{j+1}) \\ U_{j+1}^\downarrow(z_{j+1}) \end{pmatrix} = \mathbf{T}_j \begin{pmatrix} U_{j+1}^\uparrow(z_{j+1}) \\ U_{j+1}^\downarrow(z_{j+1}) \end{pmatrix}$$

For a complete multi-layered structure, we can express the electric field amplitudes on both sides of the structure using the matrix notation:

$$\begin{pmatrix} U_0^\uparrow \\ U_0^\downarrow \end{pmatrix} = \mathbf{R}_{0,1} \mathbf{T}_1 \mathbf{R}_{1,2} \mathbf{T}_2 \dots \mathbf{R}_{n-1,n} \begin{pmatrix} U_n^\uparrow \\ U_n^\downarrow \end{pmatrix} = \begin{pmatrix} M_{11} & M_{12} \\ M_{21} & M_{22} \end{pmatrix} \begin{pmatrix} U_n^\uparrow \\ U_n^\downarrow \end{pmatrix} \quad (2.22)$$

where U_0 is the amplitude at the surface of the multilayer structure and U_n is the amplitude at the last interface. It is necessary to multiply all the reflection and propagation matrices in the right order to describe the complete multi-layer structure. The total reflectivity from the multilayer structure is given by:

$$R_{\text{total}} = \left| \frac{U_0^\uparrow}{U_0^\downarrow} \right|^2 = \left| \frac{M_{12}}{M_{22}} \right|^2$$

where it is assumed that the multi-layer substrate absorbs the penetrating x-ray beam sufficiently, so that a reflected wave, ($U_n^\uparrow = 0$), from the back of the substrate can be neglected.

As an example, the reflectivity of a simple multilayer system has been calculated and illustrated in Figure 2.7. Interference fringes due to reflections from subsequent surfaces are clearly visible. Their period depends on the film thickness. Surface roughness reduces the reflectivity according to the Debye-Waller model.

Assuming that the material composition of each layer in the multi-layer structure is known, the thickness t_j , the density ρ_j , and surface roughness σ_j of the layers j are used as fitting parameter. The Levenberg-Marquardt algorithm for nonlinear regression [8, 9], which is integrated into MATLAB, has been used to extract these parameters from experimental data and the model described above.

Chapter 3

Time-resolved x-ray scattering

3.1 Laser-matter interaction

Femtosecond laser pulses were used to initiate structural changes in solids (Paper I and Paper III - Paper VII). Laser light couples directly to the electrons in a medium. The dynamics of the electron system can only be studied indirectly using x-ray diffraction by its effect on the lattice. A wide variety of processes can be initiated by the interaction of laser-light with matter, depending on the laser pulse and material properties. In the following, the interaction of the laser pulse with the medium and the resulting processes are discussed in a schematic overview.

In the first step, the laser pulse is absorbed by the material. In the case of a semiconductor, electrons will be promoted from the valence band to the conduction band. Nonlinear processes such as two-photon-absorption and free carrier absorption can be important contributions in the absorption of ultrashort pulses. In the second step, electron-electron scattering establishes a thermal equilibrium within the electron system, while the lattice is still at the temperature prior to laser excitation. This takes place in a time on the order of 10 fs [10]. Additionally, the diffusion of hot electrons out of the laser-excited region reduces the initial electron temperature and increases the excited volume. In the third step, the absorbed energy is transferred from the electrons to the lattice by electron-phonon coupling. The lattice temperature rises as phonon modes become occupied. A thermodynamic equilibrium between lattice and electron system, with a common temperature is established on the 1-100 ps timescale. The fourth step is the relaxation of the electron and lattice system. Electrons recombine with holes, emitting photons (radiative) or transferring energy to another carrier (Auger). Heat conduction towards colder parts of the sample decreases the lattice temperature. The timescale for this is in the 1-100 ns range.

In quantitative analysis of the lattice dynamics following laser excitation, the interaction processes described above must be taken into account carefully.

3.2 The Thomsen model

The Thomsen model [11] describes the generation of strain in a laser heated metal or semiconductor. Thermal stress due to temperature increase leads to expansion of the sample starting at the surface. This is accompanied by a strain wave traveling inwards from the sample surface. Electronic strain due to photo-generated carriers and coupling by the deformation potential is neglected in the Thomsen model. The initial temperature change ΔT decays exponentially with distance from the surface, z , according to the Beer-Lambert law:

$$\Delta T(z) = (1 - R) \frac{F}{C\xi} \cdot e^{-z/\xi} \quad (3.1)$$

where R is the sample surface reflectivity of the laser light, F the laser fluence, C the heat capacity, and ξ the absorption length of the laser light. Since ξ is negligible small compared to its lateral size, the problem can be considered quasi one-dimensional. The initial stress and following expansion will thus only be dependent on z .

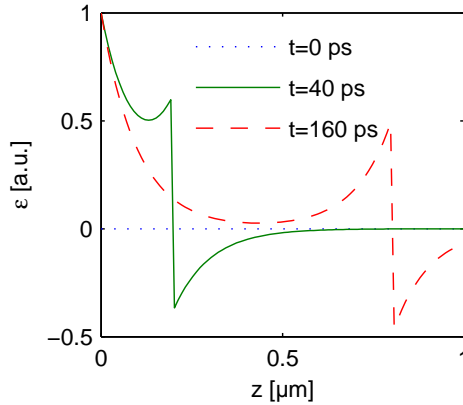


Figure 3.1: Calculated strain following laser excitation using the Thomsen model at various times: 0 ps (dotted line), 40 ps (solid line), and 160 ps (dashed line). Assumed material parameter: speed of sound $v=5$ km/s and laser absorption length $\xi = 0.1 \mu\text{m}$.

The elastic equations can be used to describe the evolution of strain in the sample:

$$\rho \frac{\partial^2 u}{\partial t^2} = \frac{\partial \sigma}{\partial z} \quad (3.2)$$

$$\sigma = 3 \frac{1-\nu}{1+\nu} B \epsilon - 3B \beta \Delta T(z) \quad (3.3)$$

where σ is the stress, u the displacement, and $\epsilon = \partial u / \partial z$ denotes the strain. The parameter ρ is the density, B the bulk modulus, ν Poisson's ratio, and β the linear expansion coefficient of the medium. As boundary condition, the stress σ can be assumed to vanish at the free surface ($z = 0$). Using the temperature profile $\Delta T(z)$

calculated in Equation 3.1, Thomsen has shown that an analytic solution of Equations 3.2 and 3.3 can be given [11]:

$$\epsilon(z, t) = \Delta T(z) \beta \frac{1 + \nu}{1 - \nu} \left(1 - \frac{1}{2} e^{-vt/\xi} - \frac{1}{2} e^{(z - |z - vt|)/\xi} \operatorname{sgn}(z - vt) \right) \quad (3.4)$$

where v is the longitudinal sound velocity. The function sgn is the sign function. Heat conduction is neglected here. To illustrate the results from Equation 3.4, the time-dependent strain profile is calculated and plotted in Figure 3.1. It is apparent that a strain wave is launched from the surface into the sample with the speed of sound v .

Temperature profiles and strain profiles calculated using the Thomsen model have been applied for modeling and simulation of the results reported in Paper I, Paper V, and Paper VII.

3.2.1 X-ray diffraction from coherent acoustic phonons

The strain wave launched from the surface into the bulk due to laser excitation, can be interpreted as a superposition of coherent acoustic phonons. Due to the steep flanks of the strain profile $\epsilon(z, t)$, the phonon modes in a wide spectral range are occupied. Sidebands in the rocking curve are created [12]:

$$\Delta \vec{k} = \vec{G} \pm \vec{q} \quad (3.5)$$

The x-ray beam is diffracted off the sample emitting or absorbing phonons with wavevector \vec{q} . The x-ray wavelength or the crystal angle can be tuned such that the Laue equation is fulfilled for a certain phonon mode \vec{q} . Since the phonons are excited coherently, the intensity of the diffracted x-ray beam will be modulated with the acoustic phonon frequency $\nu(q)$ [12, 13]. The modulation in x-ray intensity of the diffracted x-ray beam can be measured in a time-resolved x-ray diffraction experiment using an x-ray streak camera, such as that described in Section 5.4.1. The phonon frequency can be determined by Fourier-transforming the time-resolved x-ray diffraction signal. By detuning away from the Bragg condition and measuring the phonon frequency, ν , for each \vec{q} , we can determine the dispersion curve of the longitudinal acoustic phonon mode in the direction normal to the diffracting planes:

$$\omega(q) = 2\pi \cdot \nu(q) \quad (3.6)$$

A modulation effect can be seen in the experiment until the strain wave has left the volume probed by the x-ray beam. The minimum phonon frequency that can be determined from the measurements is governed by the time taken for the strain wave to leave the probed volume, and the accuracy with which the Bragg condition can be detuned. The limiting factors for this are essentially the x-ray probe depth and the width of the x-ray rocking curve. The maximum phonon frequency that can be determined is governed by the time-resolution of the x-ray diffraction experiment as well as the sensitivity of the detector and signal to noise ratio, since the signal gets weaker the larger q becomes.

3.3 Optical phonons in bismuth

The effect of coherent optical phonons on the x-ray diffraction from Bismuth was studied using the x-ray streak camera (Paper IV). The period of the A_{1g} mode in bismuth is about 300 fs. If this phonon mode is excited coherently, the integrated intensity of the (111) diffraction will be modulated accordingly. The time resolution of the subpicosecond streak camera was tested using this effect.

Bismuth crystallizes in the trigonal A7 structure with a two atom basis, which can be understood as a distorted fcc structure [14]. Excitation with a femtosecond laser pulse shifts the equilibrium positions of the basis atoms towards this cubic structure. This shift can be considered instantaneous compared to the A_{1g} phonon period. Therefore, the atoms will start to oscillate coherently around the new equilibrium position with the A_{1g} phonon frequency. This is called displacive excitation [15] and is illustrated in Figure 3.2.

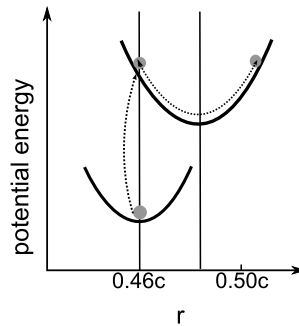


Figure 3.2: Displacive excitation of the A_{1g} phonon mode in Bismuth. Photoexcitation changes the potential energy surface and shifts the equilibrium distance between the basis atoms. r is the distance coordinate in units of the c -axis length ($c=11.8 \text{ \AA}$), the vertical lines indicate the unperturbed and the perturbed equilibrium distances.

The bismuth A_{1g} phonon mode has been studied using optical short-pulse probes [16]. The coherent atomic motion modulates the refractive index of the material. Changes in reflectivity of an optical probe pulse are measured as a function of time after excitation. The phonon frequency was determined from such a measurement in the time domain. Anharmonicity of the potential and softening under high excitation conditions were found. Since optical probes do not reveal directly structural information such as absolute amplitudes of the phonon oscillation directly, time-resolved x-ray diffraction measurements were employed to investigate this. In order to resolve the optical phonon oscillation, a femtosecond x-ray source or detectors with femtosecond time resolution are required. X-ray-based measurements of the bismuth A_{1g} phonon mode have been made using laser-plasma-based x-ray sources [17], a linac-based synchrotron x-ray source (SPPS) [18], and a slicing-based synchrotron x-ray source [19].

All these experiments were based on short IR excitation and x-ray probe pulses.

In the study presented in Paper IV, long x-ray probes and a femtosecond x-ray streak camera detector were used. The ultrafast initial change in integrated x-ray intensity after excitation could be resolved and was used to estimate the time resolution of the streak camera. Since the demonstrated time resolution was in the range 400-600 fs, the phonon oscillation could not be resolved.

3.4 Non-thermal melting of InSb

According to the Lindemann criterion, a crystal starts to melt when the lattice temperature is high that the vibrational amplitude exceeds 10% of the interatomic distances [20]. This is called thermal melting. The timescale for laser-induced thermal melting is set by the required electron-phonon coupling to a few picoseconds. If the laser fluence is sufficiently high, the excitation directly modifies the inter-atomic potential energy surface due to the dense electron-hole plasma generated [21]. The dynamics of the atoms is determined by the new potential energy surface, while the lattice temperature is unchanged during the initial picoseconds. The resulting disorder of the lattice on the timescale of a few hundred femtosecond is substantially faster than the thermal melting process. Such an ultrafast light-induced structural transition of InSb from solid to liquid has been studied by Lindenberg et al. using the Sub-Picosecond Pulse Source (SPPS) based on linac technology with a time resolution of about 100 fs [22]. A time constant of 430 fs was found for the integrated intensity change of the 111 reflection in InSb during non-thermal melting. This is consistent with continued inertial motion of the atoms with their thermal kinetic energy following laser excitation. Lindenberg et al. proposed, that the inter-atomic potential vanished completely and atoms continued to move with their respective thermal velocity. This interpretation is still the subject of debate. Zijlstra et al. recently pointed out, that the observed dynamics is consistent with a softening of transverse acoustic phonons in InSb [23], which means that the potential energy surface is merely modified. This is in agreement with earlier work by Stampfli and Bennemann [21]. Further investigations of the influence of the lattice temperature on the initial dynamics could solve this open issue.

Non-thermal melting of InSb was studied using the sub-picosecond x-ray streak camera and x-ray pulses from beamline D611 at the MAX-II electron storage ring (Paper IV). The time resolution was found to be 480 fs.

3.4.1 Diffuse X-ray scattering from laser-molten InSb

As explained above, the excitation of InSb with intense femtosecond laser pulses triggers a phase transition from the solid to the liquid phase. The threshold for non-thermal melting of InSb is at a laser fluence of about 20 mJ/cm^2 . A thin layer of liquid InSb is formed at the sample surface. The liquid is characterized by its loss of long-range order compared to the crystalline structure prior to laser excitation. To study the remaining short-range order, diffuse x-ray scattering can be employed. This technique was described in section 2.6. Zhang et al. have reported a pair correlation function for liquid InSb as a result of a molecular dynamics simulation [24]. This is

shown in Figure 3.3. They found typical correlation lengths of 0.31 nm and 0.65 nm, which can be interpreted as next- and next-next-neighbor distance in liquid InSb.

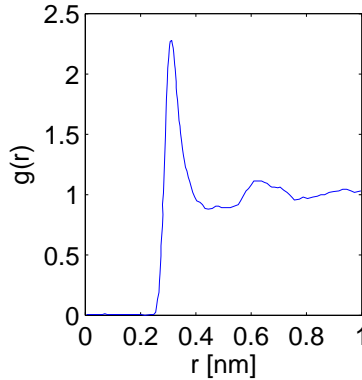


Figure 3.3: Pair correlation function $g(r)$ of liquid InSb, calculated using a molecular dynamics simulation by Zhang et al. [24]

To experimentally determine the local order in liquid InSb, diffuse x-ray scattering of laser-molten InSb was studied using the experimental setup described in Section 5.4.2. The results are reported in Paper I. The molten InSb resolidifies within about 100 ns. The crystalline bulk InSb underneath the molten layer acts as a template for re-crystallization. Therefore, the experiment could be conducted repetitively. The structure factor $S(q)$ of the liquid InSb was measured as a function of the delay between the laser pump and x-ray probe. Information about the structural dynamics of the liquid can be inferred by scanning the laser-pump with respect to the x-ray-probe delay. To obtain a full radial distribution function, a larger range of q than provided by beamline D611 would be required.

In Section 2.6 it was shown that the scattered x-ray intensity is proportional to the number of scattering centers in the sample. Therefore, the thickness of the liquid InSb film can be derived from the amplitude of the diffuse scattering signal.

Modelling thermal melting and re-crystallization following laser excitation

During the course of this work, a one-dimensional heat flow model of a transient liquid including thermal melting and re-crystallization following laser excitation was developed. The MATLAB script used for this is included in the Appendix. This model has been used to explain the dynamics of the laser-molten liquid InSb (Paper I). The model is explained below.

Thermalization of the electrons and the lattice is complete after a few picoseconds. A thin film of non-thermally molten InSb is formed and a temperature profile in the sample is established. The temperature is calculated using Thomsen's model (see Section 3.2). Since the melting temperature is exceeded, the latent heat of fusion of InSb must be included in the model. The calculated initial temperature profile $T(z, t = 0)$ was used as a starting condition for the simulation of laser-induced thermal

melting and subsequent re-crystallization of InSb. Heat conduction is accounted for and is described using the diffusion equation:

$$\frac{\partial T}{\partial t} = \alpha \frac{\partial^2 T}{\partial z^2} \quad (3.7)$$

where α is the thermal diffusivity. This differential equation 3.7 is solved numerically based on the finite element method. Figure 3.4 shows the results of the simulation for laser-molten InSb excited with a laser fluence of 45 mJ/cm^2 .

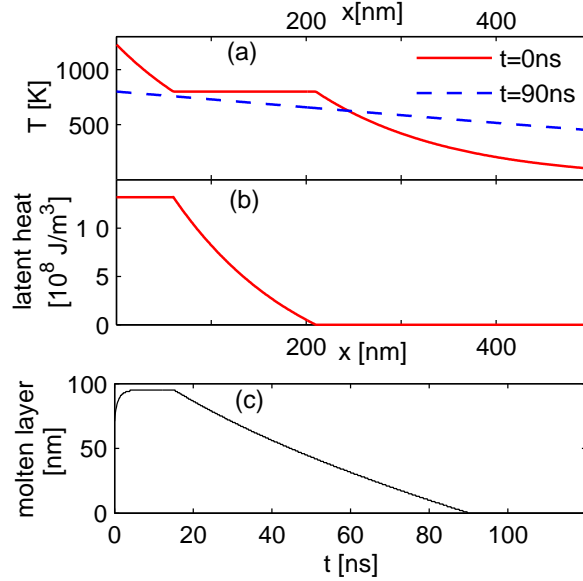


Figure 3.4: Results of simulation of the melting and resolidification of InSb following laser excitation. Panel (a) shows the depth dependency of the temperature (solid line) initially and after 90 ns (dashed line). In panel (b) the energy stored initially as latent heat is shown as a function of depth. Panel (c) shows the thickness of the molten InSb as a function of time.

The dynamics of the transient liquid can be divided into three parts. The first is non-thermal melting. A thin film of non-thermally molten InSb is formed with a thickness of about 60 nm. The timescale for this process is a few hundred femtoseconds. During this time, the structure changes from the long-range order of a crystal lattice to the short-range order of a liquid. Due to the impulsive generation of the liquid, the structure is initially in a non-equilibrium state. The formation of an equilibrium structure takes a few picoseconds [25]. The second phase is a continued thermal melting accompanied by a growth in thickness of the liquid film. It requires thermal equilibrium between the carriers and the lattice, and the conduction of excess heat deeper into the sample. The thickness of the molten layer increases until about 2 ns after excitation. The third phase is re-crystallization due to the conduction of

heat into colder parts of the sample. The thickness of the film decreases until the liquid is totally re-solidified after about 90 ns.

3.5 X-ray diffraction from laser-induced ripple-structured surfaces

Grazing incidence geometry is used to match laser excitation and x-ray probe depth, as described in Section 2.5. In a time-resolved x-ray diffraction experiment with repetitive laser excitation, the stability of the sample surface structure and crystal quality are important. Degradation of the sample surface reduces the number of useful repeated exposures.

During repetitive laser-induced melting, permanent damage builds up on the sample surface. It has been shown that for high excitation fluences, the re-solidification process yields amorphous instead of crystalline material [26].

The repetitive non-thermal melting of InSb has been proposed as a timing monitor for future short-pulse x-ray sources [27]. The sharp drop in integrated reflectivity marks the arrival time of the x-ray pulse in respect to the laser pulse. The non-thermal melting process can be used to monitor this timing from shot to shot. The long-term stability of the x-ray diffraction signal during repetitive melting has to be investigated to establish this mechanism as a timing monitor tool at user facilities.

The sample surface can be effected even at intermediate fluences. It has been shown that periodic ripple structures emerge during the repetitive melting and re-crystallization of semiconductors and metals [28–30]. This can be explained along the following lines: Part of the incident laser light is scattered by inhomogeneities in the sample surface, such as surface roughness, forming a surface wave. Due to the coherence of the laser light, the incident light wave and the surface wave create an interference pattern along the sample surface. The laser light intensity varies periodically along the surface, which causes inhomogeneous melting. This adds to the surface inhomogeneities and a periodic melting pattern forms along the surface. The repetitive inhomogeneous melting and re-crystallization form ripples, which grow gradually. The period of the interference pattern determines the spacing of the ripples created. For p-polarized light of wavelength λ , ripples will be created with periods, Λ , of:

$$\Lambda_{\pm} = \frac{\lambda}{1 \pm \theta} \quad (3.8)$$

where θ is the angle of incidence of the laser beam.

Paper III describes a study on the influence of the ripple structure on x-ray diffraction at grazing incidence. The focus of this study was on the impact of ripple formation on time-resolved x-ray diffraction experiments based on repetitive laser-induced melting. Due to the grazing x-ray incidence, the x-ray diffraction is sensitive to small changes in angle at the surface. The ripples created cause a variation in the incidence angle within the x-ray footprint on the sample. This is illustrated in Figure 3.5. The repeated melting and re-solidification process can also create amorphous material at the surface, which additionally attenuates the x-ray beam.

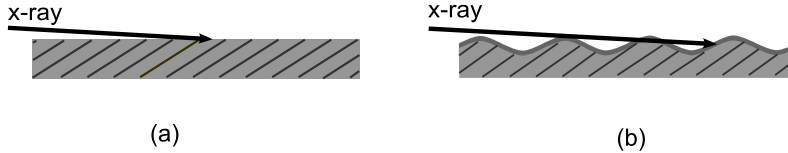


Figure 3.5: Influence of ripple structure on the x-ray diffraction geometry at grazing incidence. Panel (a) shows the unmodified sample surface. In panel (b), the surface contains ripples and a layer of amorphous material. The angle of incidence of the x-ray beam varies over the x-ray footprint.

Paper III reports on the effects of repetitive laser-melting of InSb crystals. The diffracted intensity as function of x-ray photon energy was recorded after the laser exposure and compared to energy scans from unexposed surfaces. The laser-induced ripple structure was studied using an atomic force microscope, leading to a geometric model of the sample surface. This was used to calculate curves using dynamical x-ray diffraction geometry. The influence of an absorbing layer of amorphous material was included. Due to the different angles of incidence, the shape of the energy scan curve is altered. At the slopes of the ripples, the x-ray beam can penetrate deeply into the material. This effect reduces the overlap between the laser excitation and the x-ray probe for time-resolved x-ray scattering and diffraction experiments.

In order to avoid such signal degradation, we found that after about 100000 laser shots just above the non-thermal melting threshold, this corresponds to approximately 30 s exposure time at a laser repetition rate of 4.25 kHz, the sample has to be refreshed. This was done in the melting experiment reported in Paper IV. During longer exposures without refreshing the sample, the signal was dominated by slow thermal melting dynamics. This is due to the much larger depth of the thermal melting compared to the non-thermal melting depth and the increase in x-ray penetration due to ripple growth.

3.6 Ferroelectric phase transitions in KDP

Some materials have more than one stable phase in the solid state. If a solid-to-solid phase transition is accompanied by a structural change, time-resolved x-ray diffraction can be used to follow the phase transition in real time. Ferroelectric materials exhibit strong interaction electric dipole moments between neighboring unit cells. Electric dipole-dipole interaction stabilizes the alignment of a permanent electric dipole moment along an axis in the crystal. Each domain is characterized by its net dipole moment polarization. When an external electric field is applied, the balance between the potential energy of domains with different polarizations is changed, thus facilitating phase transitions of domains from one polarization to a domain type with the opposite polarization.

Potassium dihydrogen phosphate (KDP) at room temperature has a tetragonal unit cell. At the Curie temperature of KDP, the crystal undergoes a phase transition from the paraelectric phase to the ferroelectric phase, which has an orthorhombic

unit cell and a spontaneous electric polarization. Phosphate groups are bound by hydrogen bonds within the unit cell of KDP. The potential energy surface of the hydrogen atom is double-well shaped [31]. Above the Curie temperature, the thermal energy is sufficient for the hydrogen atom to move freely between the two minima. This characterizes the paraelectric phase of KDP. Below the Curie temperature, the thermal energy is not sufficient to overcome the barrier, and two stable configurations are formed. The average position of the hydrogen atom is shifted away from the center between the phosphate groups. This is accompanied by a net dipole moment and distortion of the unit cell. These two effects are characteristic for KDP in its ferroelectric phase. The stable domain configurations have been described by Bornarel and called A+, A-, B+, and B- and M domain [32]. The unit cells corresponding to the A and B domains in KDP are depicted in Figure 3.6.

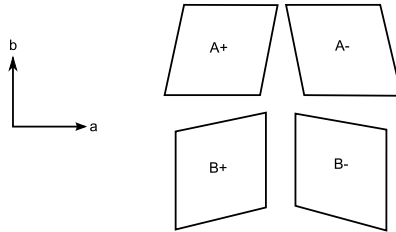


Figure 3.6: Schematic view of unit cells associated with the ferroelectric domains in KDP. a and b are the axes of the paraelectric KDP unit cell.

The domains A+ and B+, as well as A- and B-, have the same net dipole moment, but differ in the shear deformation of the unit cell. KDP has ferroelastic as well as piezoelectric properties. Transitions between the domain types can be induced by applying shear stress as well as external electric fields [33]. A ferroelectric phase transition has been observed in deuterated KDP by Larsson et al. [34].

Paper II describes the study of the ferroelastic dynamics in KDP following excitation with an electrical pulse. An electric potential was applied along the c -axis for $1 \mu\text{s}$. The resulting shear stress was released as a strain wave emanating from the sample surfaces. Strain waves released from opposite sides of the sample interfere at the center of the sample. X-ray energy scans were recorded as a function of time after excitation. Part of the ferroelastic hysteresis was recorded by measuring the shifts and amplitudes of the individual peaks associated with the domains in KDP.

3.7 Time-resolved specular x-ray reflectivity of an amorphous carbon thin film

Paper V reports on the evolution of the morphology of a thin amorphous carbon film following laser excitation, using time-resolved specular x-ray reflectivity. A schematic view of the experimental setup used for this measurement at beamline ID09B at the European Synchrotron Radiation Facility (ESRF) is illustrated in Figure 3.7.

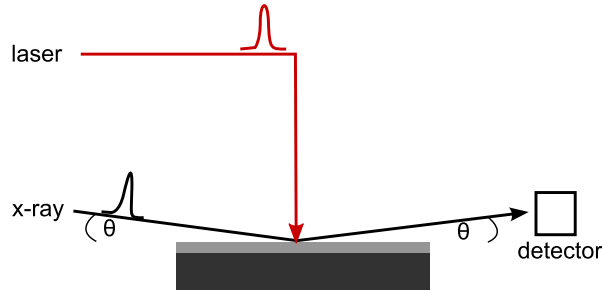


Figure 3.7: Schematic of the setup used for time-resolved specular x-ray reflectivity measurements. The reflected intensity is measured as a function of the angle θ and the time delay between the laser excitation and x-ray probe.

The theory of specular x-ray reflectivity from thin films and multi-layers was given in Section 2.7. Using this technique, the thickness, density, and surface roughness of the amorphous carbon film is determined independently. The software used to analyze the reflectivity curves and extract these parameters was developed during the course of this work and can be found in the Appendix. The parameters were extracted for each delay between laser excitation and x-ray probe. It was thus possible to determine the evolution of film morphology.

The experiment was carried out in repetitive mode in order to obtain an average over many x-ray pulses, and the laser fluence was chosen so as to be below the damage threshold of the thin film. After laser excitation, expansion of the thin film was observed, followed by relaxation. The timescale for the expansion process could not be resolved due to the limitation on the time resolution of the setup of 200 ps. The film relaxed after the expansion process with a time constant of about 1 ns.

Modeling the elastic and thermal response of a thin film following laser-excitation

In order to understand the mechanism behind the observed dynamics of the morphology of the thin film studied in Paper V, a model of the elastic and thermal response of the film and the underlying substrate was developed as a basis for simulations. As the time resolution of the experimental setup was 200 ps, a laser-induced initial temperature profile according to the Thomsen model could be assumed. This is explained in Section 3.2. Heat conduction is described using the diffusion equation 3.7. The elastic equations 3.2 describe the evolution of strain in the film and substrate due to laser-induced thermal stress. The problem based on these equations was solved numerically using the finite element method. To explain the observed fast relaxation of the thin film within 2 ns, the increase in heat conductivity of the substrate due to the high density of carriers had to be accounted for [35]. The interpretation is similar to that presented by Sondhauss et al. [36].

Chapter 4

Ultrafast x-ray sources

4.1 Introduction

In the following, x-ray sources, which are suitable for carrying out ultrafast time-resolved x-ray scattering or diffraction studies, are described briefly. Key parameters, advantages and disadvantages of the sources are discussed here.

4.2 Storage ring based x-ray sources

Electrons in a storage ring emit electromagnetic radiation when they are accelerated. The dipole magnets in the bends of the storage ring are a source of broadband radiation. The critical photon energy E_c of the dipole magnet is:

$$E_c = \frac{3\hbar c\gamma^3}{2R} \quad (4.1)$$

where R is the bending radius and γ is the relativistic parameter of the electrons stored in the ring. The emission spectrum spans from the microwave range up to higher energies, with a decrease in intensity above the critical energy. Electron storage rings optimized for synchrotron radiation, such as the MAX-II ring, are designed with a critical photon energy in the range required for the experiments. The critical photon energy of MAX-II bending magnet is at 2.3 keV.

Insertion devices are magnets placed in the straight sections between the bends of the storage ring. Wigglers or undulators consist of a row of magnets with alternating polarity. The electrons passing through an insertion device are accelerated periodically normal to the main propagation direction. The main parameter defining the insertion device is the K factor:

$$K = \frac{eB_0\lambda_u}{2\pi m_0c} \quad (4.2)$$

with B_0 the magnetic field strength, λ_u the period of the magnet, m_0 the electron rest mass. The emitted radiation is linearly polarized in the plane of motion of the

electrons. The emitted radiation of an undulator consists of harmonics of the order n with wavelengths:

$$\lambda = \frac{\lambda_u}{2n\gamma^2} \left(1 + \frac{K^2}{2} + \theta^2\gamma^2 \right) \quad (4.3)$$

where θ is the angle between the direction of observation and the propagation direction of the electron beam. In contrast to the spectrum of bending magnets, the radiation from undulators consists of lines with narrow bandwidth. The number of photons emitted from an undulator per solid angle and bandwidth interval is several orders of magnitude larger compared to bending magnet sources.

Electrons form bunches in the storage ring due to a balance of energy loss due to synchrotron radiation and the energy gain from the RF driven accelerating cavities in the ring. For a narrow phase interval of the RF field, the losses outweigh the gain, which creates a stable beam orbit. Therefore, the radiation emitted from a synchrotron is inherently pulsed. Typical electron bunch durations created in a electron storage ring are on the order of 100 ps. The duration of x-ray pulses generated in bending magnets and insertion devices in a storage ring is limited by the electron bunch duration. A fast detector, such as the streak camera described in Paper IV, is required to perform time-resolved measurements with a time resolution better than the pulse duration without additional modification to the storage ring. Two modifications to the storage ring in order to reduce the x-ray pulse duration directly are presented in the following subsections.

4.2.1 Slicing

The duration of x-ray pulses from an electron storage ring can be reduced by several orders of magnitude using direct interaction of intense femtosecond IR laser pulses with the electron bunch in the storage ring. This technique is called slicing [37] and was demonstrated by Schoenlein et al. [38].

The laser pulse co-propagates overlapping with the electron bunch in an insertion device. The insertion device is tuned to radiate with the same wavelength as the laser. This causes a modulation of the electron energy of the electrons overlapping with the laser pulse. Due to the energy modulation, this fraction of the electron bunch is spatially separated following the subsequent bending magnet. The radiation from this short bunch of electrons is extracted from the next insertion device through an aperture as a short x-ray pulse. This scheme is illustrated in figure 4.1. The created distortion in the electron bunch relaxes before the arrival of the next laser pulse due to damping mechanisms in the electron storage ring.

The generated femtosecond x-ray pulses are inherently synchronized to the laser source which facilitates laser-pump x-ray-probe time-resolved measurements. The advantages of this x-ray source are the femtosecond pulse duration, wavelength tunability, and stability. The number of x-ray photons created per pulse is typically on the order of one thousand. This is comparable to laser-based x-ray sources but many orders of magnitude lower than x-ray pulses generated from linac-based sources.

A femtosecond x-ray source based on this design is implemented at the Swiss-Light-Source (SLS) [39]. In this work, experiments studying the picosecond dynamics

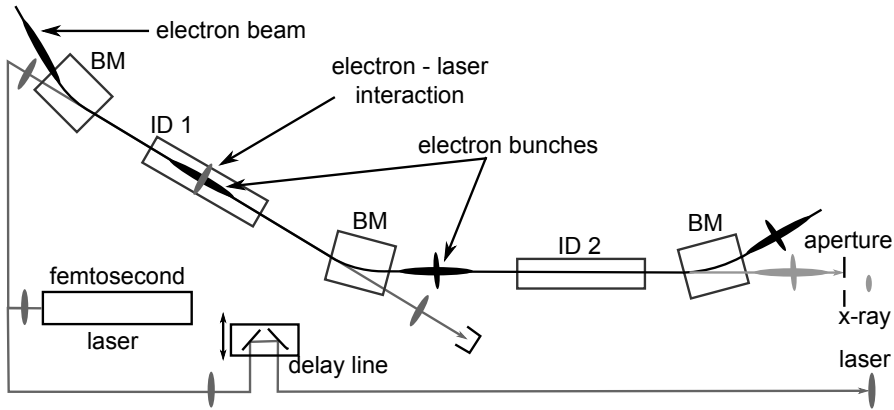


Figure 4.1: Schematic view of the slicing principle. Depicted is a section of the storage ring including bending magnets (BM) and insertion devices (ID). A femtosecond x-ray pulse is generated by modulation of a “slice” of the electron bunch using a femtosecond laser pulse in a first ID and radiation from a second ID.

of laser-induced strain in graphite have been carried out at the SLS slicing beamline. This is reported on in Paper VII .

4.2.2 Rotated bunches

Another technique to reduce the x-ray pulse duration from synchrotron sources is the rotated bunch method. It has been proposed by Zholents et al. [40], and is planned to be implemented at the Advanced Photon Source [41].

A cavity inducing a time-dependent transverse deflection of the electron bunch is installed in the electron storage ring. X-ray radiation is created in a subsequent insertion device. The deflection is canceled out with another deflection cavity after the beamline. At the insertion device, the transverse momentum components of the electrons induce divergence of the generated x-ray beam. The arrival time of the x-ray photons is related to the angles within the divergent beam. After collimation of the x-ray beam, this is equivalent to a tilted wavefront. Using an asymmetric Bragg reflection, the wavefront tilt can be corrected. This scheme is illustrated in figure 4.2.

An x-ray pulse duration of about 1 ps is expected from this source without compromising the photon flux of the beamline. Several beamlines of the storage ring in the section localized between the deflection cavities can be served with rotating bunches.

4.3 Linac-based x-ray sources

Electron bunches accelerated in a linac are not subject to the balance of synchrotron oscillations and damping by emission of synchrotron radiation, which determine the

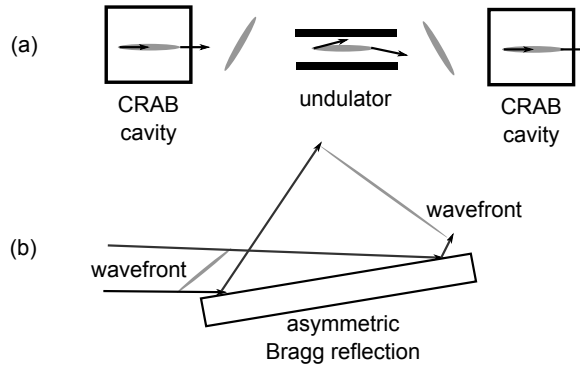


Figure 4.2: Principle of the rotated bunch method. (a) Transverse deflection is induced by cavities causing electron bunch rotation and a time-dependent divergence of the emitted x-ray beam in a insertion device between the cavities. (b) The x-ray pulse can be compressed to about 1 ps duration by compensating the wavefront tilt.

bunch length in circular accelerators, such as electron storage rings. Using bunch compression techniques, the pulse duration can be adjusted into the subpicosecond range. An undulator or wiggler after the linac section can be used to generate femtosecond x-ray radiation from the short electron bunches. The planned short-pulse-facility as part of the MAX-IV project is an example of a linac-based source of femtosecond x-ray pulses. The generated femtosecond x-ray pulses are planned to be utilized in beamlines dedicated for studies of ultrafast x-ray diffraction and scattering as well as ultrafast x-ray spectroscopy.

4.3.1 X-ray free-electron lasers

X-ray free electron lasers have been proposed as a source of short x-ray pulses with ultra-high peak brightness. All present designs are based on the self-amplified-spontaneous-emission (SASE) principle. The peak brightness of x-ray FELs is expected to be eight orders of magnitude higher than of conventional synchrotron based x-ray sources. A free-electron laser for VUV and soft x-ray based on the SASE principle was demonstrated at DESY [42]. The first hard x-ray FEL LCLS, which is also based on SASE, started operation in april 2007 [43].

A periodic magnetic field from an undulator serves as a source of radiation and as a means of coupling between the electrons and the generated radiation. As the electron bunch propagates along the undulator, the interaction of the undulator radiation with the electrons causes a density modulation of the electron bunch, which is called micro-bunching. The electrons are starting to emit x-ray radiation collectively in phase.

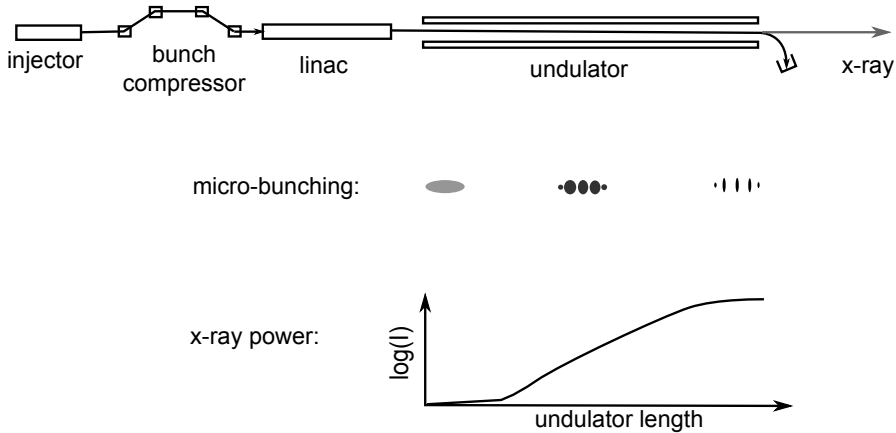


Figure 4.3: Schematic view of an x-ray FEL based on SASE. Femtosecond electron bunches with very low emittance are injected into a long undulator. The interaction of the created undulator radiation with the electron bunch itself, creates a density modulation. The x-ray power is increasing exponentially in the undulator up until a saturation length.

This in-phase emission is the cause for the high brightness and the full transverse coherence of the emitted free electron laser beam. The radiated power increases exponentially along the undulator until the end of the micro-bunching process, which is called saturation length. For x-ray FEL sources, saturation lengths are typically several tens of meters. The photon flux is scaling with the square of the electron number instead linearly as in a synchrotron source.

4.3.2 Energy-recovery linac

An energy-recovering linac (ERL) is an x-ray source operating at high repetition rate delivering femtosecond x-ray pulses into multiple beamlines simultaneously. In comparison to third generation synchrotron sources, it features low emittance, a high degree of transverse coherence, and high peak brightness. The average brightness is comparable. Successful operation of an ERL as a source of coherent IR radiation has been demonstrated at Jefferson Laboratory [44]. Recently, this principle has been put forward as an x-ray source at Cornell University [45].

Electrons are generated in a low emittance source and accelerated by a linac. After a single-pass around a ring with multiple insertion devices generating x-ray radiation, the electron bunches are entering the linac again at a decelerating phase. Thus, the kinetic energy of the electrons is returned to the electromagnetic field of the cavity. Electrons are not stored in this ring, therefore synchrotron oscillation is avoided and femtosecond electron bunches can be maintained.

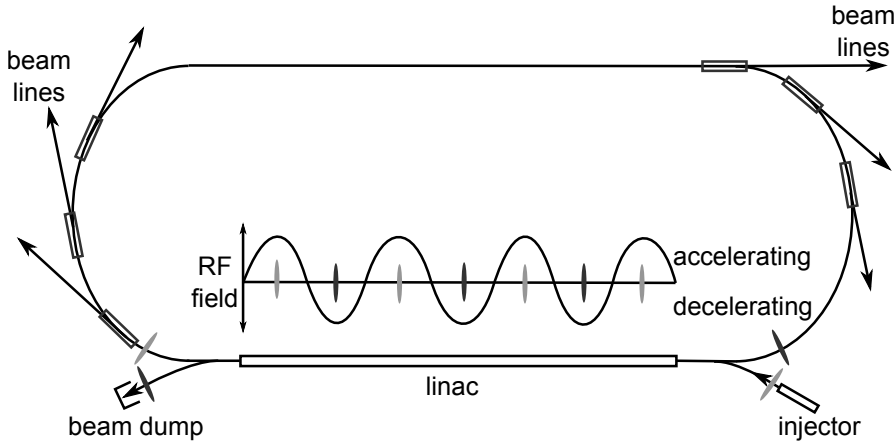


Figure 4.4: Energy recovering linac principle (schematic).

4.4 Laser-based x-ray sources

Focusing femtosecond high energy laser pulses onto a target material creates a plasma, which radiates in wide spectral range [46]. Electrons in the plasma are accelerated by the Ponderomotive force generated by the laser pulse. Bremsstrahlung and x-ray radiation of the characteristic lines of the target material are emitted due to interaction of the relativistic electrons and the atoms in the target material. If the characteristic x-ray lines are used, the wavelength can be selected by the choice of target material. The duration of the generated x-ray pulses depends on the plasma lifetime, the laser pulse properties, and the target. It has been shown, that x-ray pulses of a few hundred femtosecond duration can be produced [47]. The generated femtosecond x-ray pulses are synchronized inherently to the short pulse laser source, which helps time-resolved pump-probe x-ray diffraction experiments using this x-ray source. Disadvantages are the comparably low photon flux and the x-ray emission into a large solid angle.

Chapter 5

Beamline D611

5.1 Introduction

Beamline D611 is a bending magnet beamline at the MAX-II storage ring, which is part of the synchrotron radiation facility MAX-Lab in Lund, Sweden [48]. The key parameters of the MAX-II storage ring are listed in Table 5.1. Due to the relatively small dipole bending radius at the moderate electron beam energy of the MAX-II storage ring, the critical photon energy is in the hard x-ray range at 2.2 keV. D611 is a versatile hard x-ray diffraction beamline for time-resolved structure studies in a variety of setups. Diffraction in Bragg- and Laue-geometry, diffuse scattering, and powder diffraction experiments can be carried out.

Supplementary to the x-ray beamline, a short-pulse amplified laser system enables measurements combining IR and x-ray radiation. The laser pulses are used to trigger structural changes in a sample, which are probed with the x-ray beam.

A variety of detectors are available for time-resolved measurements. A gated 2-dimensional x-ray detection system for measuring diffuse x-ray scattering, which was implemented as part of this work, is described in Section 5.4.2 and Paper I. The time resolution of this system, typically 300 ps, is limited by the x-ray pulse duration and the synchronization jitter. An ultrafast x-ray streak camera is used for time-resolved x-ray diffraction measurements with sub-picosecond time resolution. This system

Table 5.1: Key parameters of the MAX-II storage ring

Electron energy	1.5 GeV
Ring circumference	90 m
Injection current	200 mA
Typical lifetime	20 h
Dipole magnet field	1.5 T
Critical photon energy	2.2 keV
Accelerator radio frequency	100 Mhz
Electron bunch duration	300 ps

is described in Section 5.4.1 and Paper IV . A variety of x-ray diodes allow x-ray diffraction measurements for steady state as well as time-resolved studies limited by the x-ray pulse duration. A setup for powder diffraction has been implemented in the course of this work, which is described in Section 5.5.

An alternative way to initiate structural dynamics in the sample is to apply a short electrical pulse to the sample. This was used in a piezo-electrically active sample as described in Paper II .

5.2 The x-ray optics

Figure 5.1 shows a schematic view of the core components of the x-ray beamline. Valves and beryllium windows, which protect the ring vacuum, have been omitted for clarity. The x-ray source is a bending magnet at the MAX-II storage ring. The divergence of the source is defined by an initial beryllium window to 4 mrad in the horizontal and 0.34 mrad in the vertical direction. The x-rays are focused by a gold-coated toroidal mirror to a minimum focal size of $200\ \mu\text{m}$ horizontally and $400\ \mu\text{m}$ vertically. The focal spot can be adjusted by changing the tilt angle and the vertical bending radius of the mirror. The setup allows the x-ray beam to be focused at different positions inside and outside the sample chamber for experiments in vacuum or air.

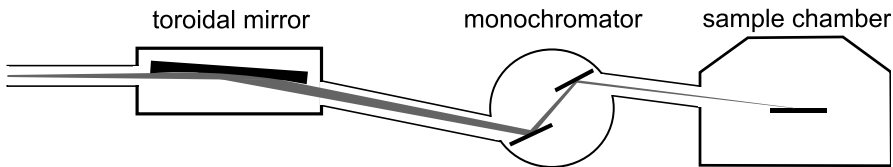


Figure 5.1: Layout of the x-ray beamline including focusing mirror, monochromator and experimental chamber.

A double-crystal monochromator is placed further downstream to select a certain part of the broad bending magnet spectrum. There are several options to monochromatize the x-ray beam: a multilayer, silicon crystals and InSb crystals. It is possible to switch between the multilayer and either silicon or InSb crystals within a few minutes using translation stages inside the monochromator chamber. The calculated reflectivity and bandwidth for these three options are given in Table 5.2.

Table 5.2: Reflectivity and bandwidth of the double crystal monochromator options available (calculated).

Monochromator option	Reflectivity	Bandwidth
Silicon 111	0.80	0.02 %
InSb 111	0.65	0.07 %
Multilayer	0.6	1% – 2%

5.2.1 InSb double-crystal monochromator

When no slits are used, the divergence at the sample position is 0.51 mrad. The x-ray energy varies by about 0.3% within the incidence angle at the sample, which is large compared to the ideal bandwidth of silicon and InSb monochromators (in a collimated x-ray beam configuration: 0.02% and 0.07%). As a result of this, the total x-ray bandwidth after the monochromator is determined by the divergence. This is illustrated in Figure 5.2.

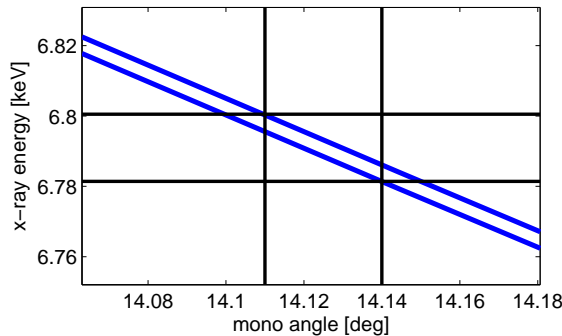


Figure 5.2: Calculated x-ray energy for the InSb crystal monochromator (divergence 0.51 mrad, and monochromator angle 14.125°). The two vertical lines indicate the beam divergence, and the horizontal lines the spread in x-ray energy. The blue curves show the ideal bandwidth of an InSb monochromator.

A good method of checking the total x-ray bandwidth downstream of the monochromator is to measure an absorption spectrum around an inner-shell edge of an absorber. The natural linewidth of these edges is sufficiently smaller than the bandwidth of crystal monochromators. The divergence induced x-ray bandwidth can be reduced by closing vertical slits upstream of the sample. The disadvantage of this is, that the x-ray flux at the sample position is reduced.

The x-ray photon flux at the sample position for both a double crystal silicon and an InSb monochromator has been calculated and is shown in Figure 5.3. Absorption in beryllium windows and the reflectivity of the gold coated mirror is accounted for. The x-ray brightness is calculated for the average electron current in the ring. It is evident, that the x-ray photon flux from an InSb monochromator is expected to be much higher throughout the spectrum of the bending magnet beamline than that from the standard silicon monochromator. This is mostly due to the higher natural bandwidth of the InSb reflection. During the course of this work, the InSb monochromator was designed, installed, aligned, and used in several experiments. The alignment procedure involved optimization of the tilt angles of both crystals in the monochromator with respect to each other.

Silicon is superior to other monochromator crystals when cryogenically cooled crystals are required. Heat-induced strain in silicon is small at the temperature of liquid nitrogen (77 K). Since the x-ray heat load at bending magnet beamlines at

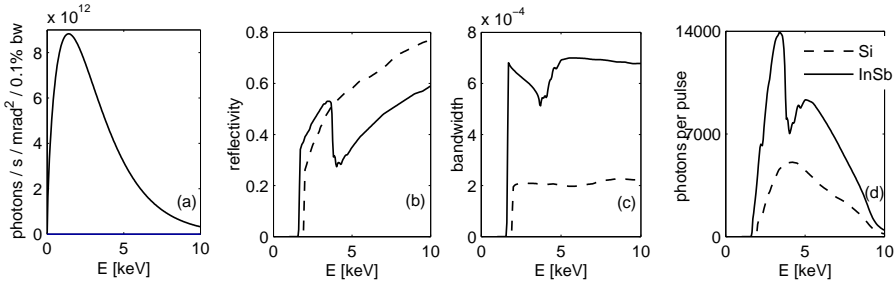


Figure 5.3: X-ray throughput. Dashed lines: silicon crystal monochromator, solid lines: InSb crystal monochromator. Brightness (a) of a bending magnet source at MAX-II. Reflectivity (b) and bandwidth (c) of the double-crystal monochromator. Number of photons per pulse (d) at sample position.

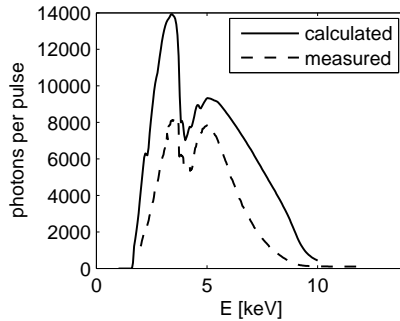


Figure 5.4: Comparison of the calculated x-ray photon flux with a measurement after installation of the InSb monochromator at beamline D611.

the MAX-II storage ring is only a few watts, cryogenic cooling is not required, and alternatives to silicon crystals can be considered.

If the sample is of the same crystal type as the monochromator crystal in single-crystal diffraction studies, the bandwidth caused by divergence will have no effect. Within the divergent beam, the Bragg condition for diffraction from the sample is fulfilled for all angles. Therefore, measured rocking curves of InSb crystals using an InSb monochromator will retain the ideal narrow width, independent of the beam divergence. On the other hand, studies employing techniques such as x-ray spectroscopy, powder diffraction, or diffuse x-ray scattering will be affected by divergence-induced bandwidth. The choice of monochromator crystal type is unimportant for the resolution in q-space of these experiments, as long as the x-ray divergence is not reduced. In short, most experiments performed at the D611 beamline benefit from the increased x-ray flux of the InSb monochromator compared to the more common silicon monochromator, while not suffering from the larger natural bandwidth.

The calculated x-ray flux of the monochromator based on the InSb crystal at the D611 beamline was compared to a measurement scanning the complete energy range

available at the beamline after the InSb monochromator was installed. The results are displayed in Figure 5.4. The measurements were performed with calibrated PIN-type x-ray diodes. The diode current was converted into absolute values of the photon flux. Reasonable agreement was found between the calculated and measured values. Overall, the x-ray flux is substantially higher than that which could be achieved using a standard silicon crystal monochromator. Previous to the installation of the new InSb monochromator, a full-range energy scan of the monochromator was not possible without step-by-step realignment of the crystal pitch angle.

5.3 Laser system

The laser system at beamline D611 is located in a separate hutch. It includes a titanium-sapphire-based ultrafast laser oscillator and amplifier. Both are manufactured by KMLabs. External mechanical delay stages allow the time delay of the various beams to be varied. An overview of this can be seen in Figure 5.5.

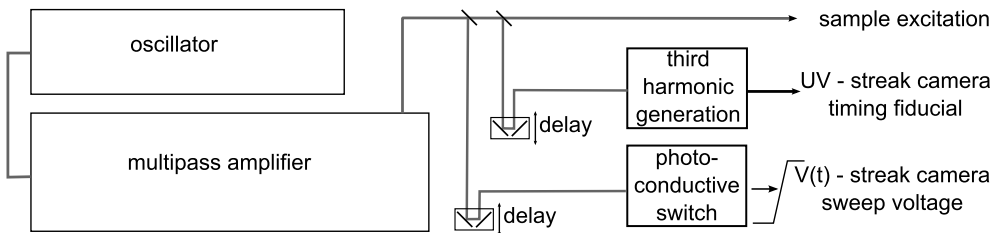


Figure 5.5: Schematic overview of the laser system including laser oscillator and amplifier. The main beam is split into three parts with adjustable delays.

The oscillator is a passively mode-locked titanium-sapphire laser. It is pumped by a cw solid-state laser (Coherent Verdi). To facilitate measurements combining a laser and x-rays, the output of the oscillator is synchronized to the train of x-ray pulses at the beamline. This is explained further in Section 5.3.1. Detailed figures of the oscillator are listed in Table 5.3.

Table 5.3: key parameter of the ultrafast titanium-sapphire laser oscillator

Average power	500 mW
Repetition rate	100 MHz
Center wavelength	780 nm
Bandwidth	40 nm
Pulse duration	100 fs
Fourier-transform limit	25 fs
Chirp parameter	3.9

The temporal intensity and phase of the oscillator pulses are inferred from frequency-resolved optical gating (FROG) measurements. The results are plotted in Figure 5.6. The oscillator pulse duration was determined from these results.

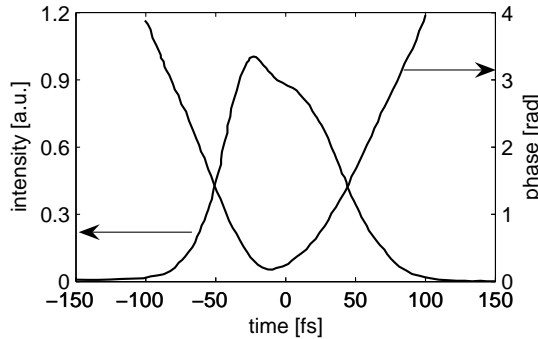


Figure 5.6: Temporal intensity and phase of the laser pulses from the ultrafast titanium-sapphire laser oscillator. Calculated from a measured FROG trace.

The oscillator is used to generate the seed beam for the laser amplifier, which is based on chirped-pulse amplification. The input pulses are stretched to about 200 ps duration using a grating stretcher, and the repetition frequency is reduced to an adjustable rate in the kHz range by a Pockels cell. A Q-switched, diode-pumped solid-state laser (Coherent Corona) pumps the cryogenically cooled multi-pass amplifier module. The last element in the amplifier is a grating compressor which shortens the duration of the pulses to about 45 fs (measured using FROG). The main characteristics of the amplifier system are listed in Table 5.4.

Table 5.4: key parameter of the ultrafast titanium-sapphire laser amplifier

Repetition rate	4-8 kHz
Typical pulse energy	1 mJ
Typical average power	5 W
Center wavelength	780 nm
Bandwidth	35 nm
Pulse duration	45 fs

The beam is split into three arms, all of which are sent into the x-ray hutch. The power of each can be set using a half-wave plate and a polarizing beam splitter. Mechanical delay lines allow the time delay of each beam to be set separately. A schematic view of the various beams is given in Figure 5.5. The main fraction of the amplifier output is used to excite the sample and trigger a transient structure change. A second beam is used in a photo-conductive switch to generate a voltage surge. The third beam is converted by a third harmonic generator into UV pulses, used for timing. These two beams are used for the x-ray streak camera, which is a time-resolving x-ray detector. This device is explained in detail in Section 5.4.1.

5.3.1 Synchronization

The oscillator is synchronized to the x-ray pulse train from the MAX-II storage ring. The repetition rates of the two sources are matched to facilitate time-resolved experiments involving IR and x-ray radiation. This is achieved by regulating the repetition rate of the laser oscillator. The repetition rate is determined by the cavity length. One end mirror is mounted on a piezoelectric crystal for rapid adjustment, and the mirror mount is fixed onto a translation stage for slow movements. A schematic view of the synchronization circuit is given in Figure 5.7.

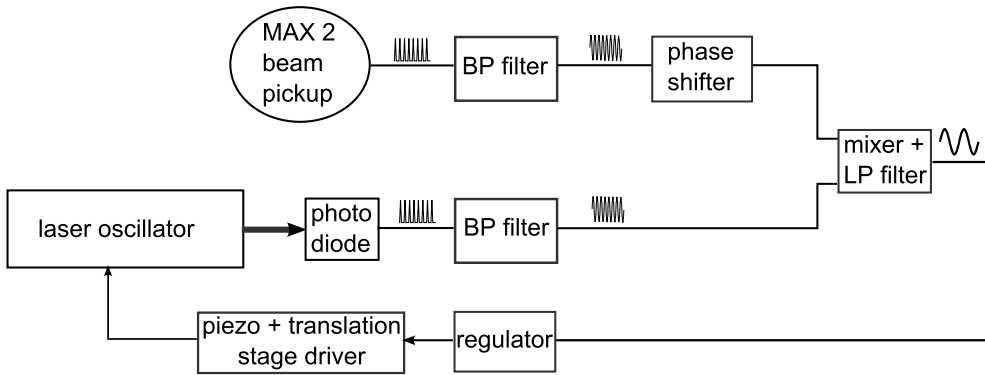


Figure 5.7: Schematic view of the system synchronizing the laser oscillator to the x-ray pulse train. BP = band-pass, LP = low-pass.

The output of the oscillator is measured using a sufficiently fast photodiode, and the x-ray reference signal originates from a beam pickup in the MAX-II storage ring. Both signals are fed into a mixer. The resulting error signal represents the frequency mismatch. A regulating circuit, which is connected to the actuator's piezo crystal and translation stage, is set to remove the error signal. When the regulator is activated, the frequencies of the two sources are matched, and the phase is kept constant. The amplitude of the remaining error signal is a measure of the jitter between the laser and the x-ray source. Using a 3 GHz reference, a synchronization jitter of 170 fs can be achieved, which is much smaller than the x-ray pulse-duration, and thus sufficiently small. It is possible to set the delay between the laser and x-ray pulses. This is done using a voltage-controlled phase shifter, installed at one of the mixer inputs. Since the repetition rate is 100 MHz, a delay of 0-10 ns can be set by introducing a phase shift of $0-2\pi$.

5.4 Setups for time-resolved measurements

5.4.1 An ultrafast x-ray streak camera for time-resolved x-ray diffraction

To improve the time-resolution beyond the limit set by the x-ray pulse duration, the beamline is equipped with an x-ray streak camera. This type of detector has proven

invaluable in various time-resolved x-ray diffraction experiments [12, 13, 27, 34, 49–57]. A schematic overview is given in Figure 5.8. Impinging x-ray photons create electrons along a slit-shaped photo cathode. In the cathode material, an x-ray photon generates hot primary electrons and, following this, a cascade of secondary electrons. The x-ray beam strikes the cathode at grazing incidence in order to match the x-ray absorption depth with the escape depth of the secondary photoelectrons [58], thus increasing the number of electrons extracted. The electron yield and energy distribution have been characterized for a variety of cathode materials [59, 60]. After acceleration by an anode mesh, the electrons pass through a pair of sweep plates. An electric field varying in time, applied between the sweep plates, deflects electrons depending on their arrival time. A photo conductive switch triggered by the laser beam generates the sweep voltage [61, 62]. The voltage at the photo conductive switch is reversed within a few nanoseconds after laser excitation. This voltage ramp is inherently synchronized to the laser beam exciting the sample. To accommodate the difference in electron velocity and electric sweep signal, a meander-line-shaped structure is used to apply the sweep voltage. A subsequent magnet lens focuses the electrons onto a multichannel-plate and phosphor based detector. A fast CCD camera with embedded image processing capability is used to capture the signal, thus enabling single-shot readout and analysis.

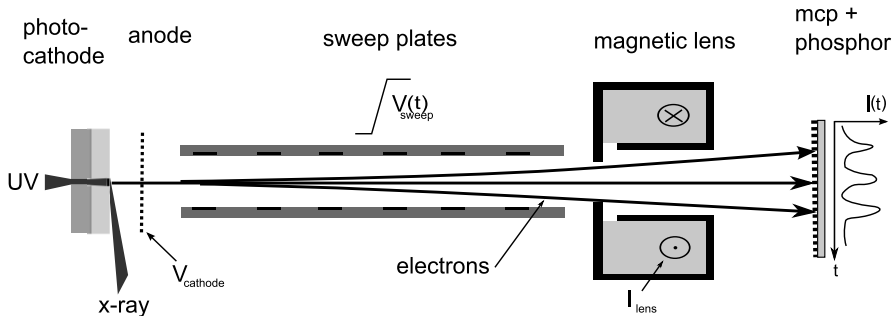


Figure 5.8: Schematics of the streak camera as it is used at beamline D611. See text for description.

The time resolution of this detector depends on several factors. The photo cathode material used is cesium iodide, which has a secondary electron energy spread of 1.5 eV [59]. After acceleration of the electrons, this will create an electron bunch with a duration of:

$$\Delta t \approx \frac{1}{E} \frac{\sqrt{2m_e \epsilon}}{e} \quad (5.1)$$

with E standing for the acceleration field strength and ϵ for the energy spread of the photo electrons. Assuming an acceleration field strength of 10 kV/mm, Equation 5.1 predicts the duration of the resulting electron bunch to be approximately 400 fs. Other factors determining the time resolution are the width of the photo cathode, the sweep voltage, and the jitter. It has been shown that jitter can be reduced to 50 fs by stabilizing the laser used to trigger the photoconductive switch [63].

The time resolution can be drastically improved by analyzing each sweep independently [64,65]. This method requires that a sufficiently large number of photoelectrons can be detected and analyzed for each x-ray photon. Thus, the x-ray photon arrival time can be determined more accurately. A timing fiducial is required for every shot in this technique, which is implemented using a third-harmonic beam of the laser. The photo electron yield was increased by utilizing grazing incidence at the photo cathode. Sub-picosecond time resolution for hard x-rays has been achieved. The implementation of these features and the performance of the streak camera are described in Paper IV .

5.4.2 Setup for time-resolved diffuse x-ray scattering

An overview of diffuse x-ray scattering from non-crystalline media can be found in Section 2.6. To measure the x-ray scattering pattern for samples without long-range order, an x-ray imaging detector is required. Typical samples are liquids, amorphous solids, or molecules in solution. To resolve structural dynamics in these samples, a time-resolved x-ray imaging scheme is necessary. Chemical reactions in molecules or re-arrangement of the local order in solids and liquids usually take place on the femtosecond or picosecond timescale. Using pulsed laser excitation and x-ray probing by diffuse scattering, an experiment can be performed with sufficient time resolution. The pulse duration of an ultrafast laser is on the order of 100 fs, whereas the x-ray pulse duration depends on the source. Typical values are in the range between 300 ps (synchrotron source) and 100 fs (slicing-, LINAC-based sources, laser plasma). For synchrotron sources, both synchronization of the laser to the x-ray source and gated detection are necessary. Snapshots of the structure are recorded. The structural dynamics can be resolved by scanning the excitation-probe delay.

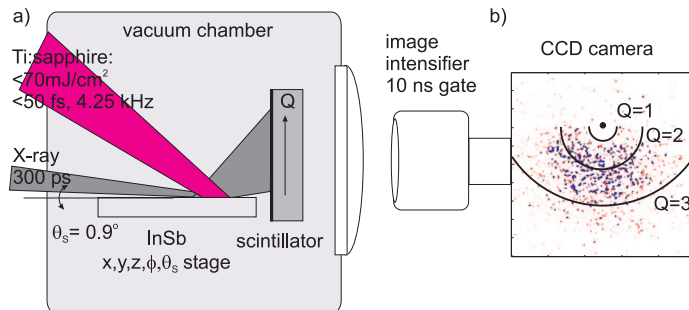


Figure 5.9: Overview of the setup used for time-resolved diffuse scattering at beamline D611. Figure from Paper I

In the course of this work, a time-resolved diffuse scattering setup was implemented at beamline D611, and the first experiment was performed. A schematic overview of the setup is given in Figure 5.9. The time resolution is limited by the duration of the x-ray pulses from the MAX-II storage ring, which is about 300 ps. The laser is synchronized to the x-ray source with a jitter of about 10 ps, which is sufficiently small compared to the x-ray pulse duration. The sample is excited by the laser pulses.

X-rays, scattered off the sample, are converted into visible photons by a scintillator plate. The lifetime of the scintillator must be sufficiently short to avoid pile-up effects arising from consecutive x-ray pulses. The interval between x-ray pulses from MAX-II is 10 ns, thus the 2.1 ns lifetime of the BC-408, Saint-Gobain plastic scintillator is sufficient to discriminate between different x-ray pulses. Since the excitation rate of 4.25 kHz, which is set by the laser, is different from the x-ray probe repetition rate (100 MHz), a gating mechanism is required to select individual x-ray pulses. This is achieved by using a gated image intensifier (Hamamatsu C9546), which images the scintillator plate. The image intensifier consists of a photo cathode followed by a multichannel plate (MCP) and a phosphor screen. Gating is achieved by applying a short voltage pulse to either the cathode or the MCP, therefore gain exists only during the selected time interval. The gate duration of the image intensifier can be as short as 3 ns, thus individual x-ray pulses can be singled out. A CCD camera in averaging mode is used to read out images. Alternatively, if single shot analysis is required, a sufficiently short exposure time (to include only one x-ray pulse) has to be chosen, and the exposure of the CCD must be synchronized. A schematic overview of the timing system and gating is given in Figure 5.10. The delay between laser excitation and the x-ray probe is set using the phase shifter, which is part of the laser synchronization system described in Section 5.3.1, with an accuracy of about 20 ps (synchronization jitter).

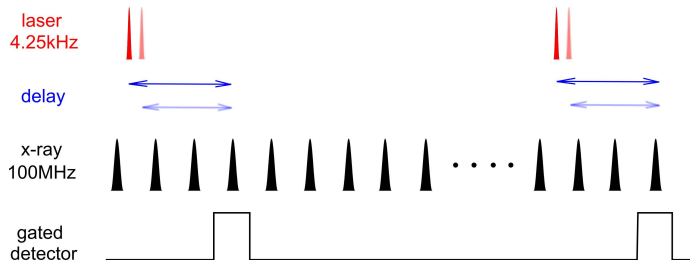


Figure 5.10: Timing system for the time-resolved diffuse scattering setup based on a gated detector. As an example two different laser-x-ray delays are shown.

The detection system was installed at beamline D611, and the first experiment using this setup studying the phase transition from crystalline to liquid InSb was performed (Paper I). Since the time resolution was limited to 300 ps, the structural dynamics during the non-thermal melting process following laser excitation could not be resolved. The scattering from the liquid InSb after thermalization was studied and the subsequent regrowth into the solid phase was observed and explained by heat conduction. A model based on heat conduction and melting in InSb, which includes the latent heat in the liquid, has been developed to describe the thermal melting and resolidification dynamics after laser excitation. A computer simulation based on this model was conducted to verify the model. A good agreement was found with experimental data. The source code for this computer simulation is listed in the Appendix.

Improvement of the time resolution of this detection scheme to the 100 fs range for diffuse x-ray scattering requires shorter x-ray pulses, such as those provided by LINAC- or slicing-based x-ray sources. The same gating and timing scheme can be used. Induced temporal smearing resulting from the crossed beam geometry has to be carefully avoided. A co-linear pump-probe geometry or tilted laser wavefronts are possible solutions to this problem.

5.5 A setup for powder diffraction

A powder diffraction setup was developed and implemented at beamline D611 during the course of this work.

Samples in the form of powders or polycrystalline solids can be studied using x-ray powder diffraction (the Debye-Scherrer method). A schematic overview of the setup is shown in Figure 5.11. A bulk solid sample is exposed to the x-ray beam at grazing incidence. To facilitate this, the x-ray spot size is reduced by closing the x-ray slits located close to the sample. The grazing incidence geometry was used to increase the surface sensitivity when bulk solid samples were studied.

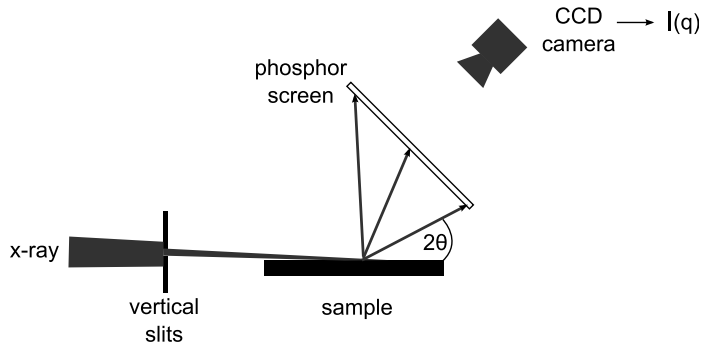


Figure 5.11: Overview of the setup for powder diffraction at beamline D611.

Diffracted x-rays impinge onto a phosphor screen, which converts the energy into visible light that can be recorded using a CCD camera. Each diffraction order of the species probed by the x-ray beam creates a conical shaped beam diffracted from the sample. The diffraction angles are determined by Bragg's law (Equation 2.10), from which the lattice constants can be determined. To further analyze the structure of the sample studied using powder diffraction, the refinement method presented by Rietfeld can be applied [66].

A MATLAB script for the analysis of the diffraction pattern recorded with a detector under an oblique angle, as depicted in figure 5.11, has been developed and applied in this work. The source code of the script can be found in the Appendix.

In the study reported in Paper VI, this setup was used to determine the structure of carbon based polymorphs generated by a laser-induced shockwave at a graphite crystal surface. Highly oriented graphite was excited using laser pulses with 80 mJ/cm^2 fluence and 100 fs duration. To investigate the structures created by the

shockwave launched from the sample surface after laser excitation, powder diffraction at grazing incidence and Raman spectroscopy were employed. It was shown that a phase transition from the hexagonal phase of graphite to the rhombohedral phase was triggered. A further analysis using Raman spectroscopy revealed, that nanoscale cubic diamonds were created locally at the sample surface.

Chapter 6

Outlook

Experiments studying ultrafast structural dynamics have so far been restricted to a few model systems. An early successful study was on the non-thermal melting process in InSb. Later, phonons in bismuth crystals and in superlattices were studied. All these model systems offer comparably high x-ray reflectivity, strong signal modulation and the possibility to acquire data repetitively, thus making the studies feasible at the time.

In April 2009, first lasing was observed at the first hard x-ray free electron laser, the Linear Coherent Light Source (LCLS), at the Stanford Linear Accelerator Center. Towards the end of 2010, the first experimental runs of the x-ray pump-probe instrument at the LCLS started. The main scope of this instrument are investigations of ultrafast structural dynamics using x-ray scattering or diffraction. The unprecedented high-intensity hard x-ray beam combined with pulse durations below 100 fs will enable studies of the ultrafast dynamics of more and more complex systems. With such high intensities it is now possible to carry out measurements in a single shot meaning that non-reversible dynamics can be studied.

So far, the LCLS is a unique source, and therefore access to users is very limited. Ultrafast structural dynamics of weakly scattering samples can be investigated. As interest in the research community is growing rapidly, new bright sources of ultrashort x-ray pulses are emerging. The European X-FEL at DESY in Hamburg is expected to start operations in 2014, and x-ray free-electron lasers are planned at SPring8 in Japan and the Paul-Scherrer-Institute in Switzerland. The linac-based short-pulse x-ray source SPF at MAX-Lab is planned to start operating as early as 2013.

One example of an experiment well suited for these sources would be the study of the structure of liquid carbon. It is difficult to melt graphite using conventional heating. But it can be molten non-thermally using an intense, short laser pulse. A large fraction of the bonds in graphite are broken, triggering a solid-to-liquid phase transition. The elusive transient state of liquid carbon could be captured by an x-ray pulse immediately after excitation. The graphite sample will be permanently damaged by the excitation pulse, therefore the structural dynamics will have to be captured using a single-pulse scheme.

So far, coherent excitation of optical phonons has mainly been realized indirectly

using electronic transitions, for example, in bismuth. Using short THz pulses, optical phonon modes in crystals can be excited directly. The pathways of structural dynamics that are coupled to optical phonon modes can be elucidated directly using a short-pulse x-ray probe.

It was predicted that free-electron laser-based sources have the potential to deliver x-ray pulses with duration as short as 1 fs. This can open up the possibility of direct studies of the dynamics of electrons in atoms and molecules using x-rays.

References

- [1] E. Prince, *International Tables for Crystallography*, vol. C. Kluwer Academic Publishers, 2004.
- [2] B. E. Warren, *X-Ray Diffraction*. Dover Publications, 1969.
- [3] B. W. Batterman and H. Cole, “Dynamical diffraction of x-rays by perfect crystals,” *Rev. Mod. Phys.*, vol. 36, no. 3, pp. 681–&, 1964.
- [4] S. Stepanov, “Sergey stepanov’s x-ray server.” <http://sergey.gmca.aps.anl.gov/>.
- [5] F. Zernicke and J. A. Prins, “Die Beugung von Röntgenstrahlen in Flüssigkeiten als Effekt der Molekülanordnung,” *Zeit. Physik*, vol. 41, p. 184, 1927.
- [6] F. Abelès, “La théorie générale des couches minces,” *J. Phys. Radium*, vol. 11, pp. 307–309, 1950.
- [7] C. Darwin, “The theory of x-ray reflexion. part ii.,” *Philos. Mag.*, vol. 27, pp. 675–690, 1914.
- [8] K. Levenberg, “A method for the solution of certain non-linear problems in least squares,” *The Quarterly of Applied Mathematics*, vol. 2, pp. 164–168, 1944.
- [9] D. Marquardt, “An algorithm for least-squares estimation of nonlinear parameters,” *Journal on Applied Mathematics*, vol. 11, pp. 431–441, 1963.
- [10] E. J. Yoffa, “Dynamics of dense laser-induced plasmas,” *Phys. Rev. B*, vol. 21, no. 6, pp. 2415–2425, 1980.
- [11] C. Thomsen, H. T. Grahn, H. J. Maris, and J. Tauc, “Surface generation and detection of phonons by picosecond light-pulses,” *Phys. Rev. B*, vol. 34, no. 6, pp. 4129–4138, 1986.
- [12] J. Larsson, A. Allen, P. H. Bucksbaum, R. W. Falcone, A. Lindenberg, G. Naylor, T. Missalla, D. A. Reis, K. Scheidt, A. Sjogren, P. Sondhauss, M. Wulff, and J. S. Wark, “Picosecond X-ray diffraction studies of laser-excited acoustic phonons in insb,” *Appl. Phys. A-Mater. Sci. Process.*, vol. 75, no. 4, pp. 467–478, 2002.

- [13] A. M. Lindenberg, I. Kang, S. L. Johnson, T. Missalla, P. A. Heimann, Z. Chang, J. Larsson, P. H. Bucksbaum, H. C. Kapteyn, H. A. Padmore, R. W. Lee, J. S. Wark, and R. W. Falcone, “Time-resolved X-ray diffraction from coherent phonons during a laser-induced phase transition,” *Phys. Rev. Lett.*, vol. 84, no. 1, pp. 111–114, 2000.
- [14] P. Fischer, I. Sosnowska, and M. Szymanski, “Debye-waller factor and thermal-expansion of arsenic, antimony and bismuth,” *J. Phys-c-solid. State. Phys.*, vol. 11, no. 6, pp. 1043–1051, 1978.
- [15] H. J. Zeiger, J. Vidal, T. K. Cheng, E. P. Ippen, G. Dresselhaus, and M. S. Dresselhaus, “Theory for dispersive excitation of coherent phonons,” *Phys. Rev. B*, vol. 45, no. 2, pp. 768–778, 1992.
- [16] M. Hase, M. Kitajima, S. Nakashima, and K. Mizoguchi, “Dynamics of coherent anharmonic phonons in bismuth using high density photoexcitation,” *Phys. Rev. Lett.*, vol. 88, no. 6, p. 067401, 2002.
- [17] K. Sokolowski-Tinten, C. Blome, J. Blums, A. Cavalleri, C. Dietrich, A. Tarasevitch, I. Uschmann, E. Forster, M. Kammler, M. H. von Hoegen, and D. von der Linde, “Femtosecond X-ray measurement of coherent lattice vibrations near the Lindemann stability limit,” *Nature*, vol. 422, no. 6929, pp. 287–289, 2003.
- [18] D. M. Fritz, D. A. Reis, B. Adams, R. A. Akre, J. Arthur, C. Blome, P. H. Bucksbaum, A. L. Cavalieri, S. Engemann, S. Fahy, R. W. Falcone, P. H. Fuoss, K. J. Gaffney, M. J. George, J. Hajdu, M. P. Hertlein, P. B. Hillyard, M. H. V. Hoegen, M. Kammler, J. Kaspar, R. Kienberger, P. Krejčík, S. H. Lee, A. M. Lindenberg, B. McFarland, D. Meyer, T. Montagne, E. D. Murray, A. J. Nelson, M. Nicoul, R. Pahl, J. Rudati, H. Schlarb, D. P. Siddons, K. Sokolowski-Tinten, T. Tschentscher, D. von der Linde, and J. B. Hastings, “Ultrafast bond softening in bismuth: Mapping a solid’s interatomic potential with x-rays,” *Science*, vol. 315, no. 5812, pp. 633–636, 2007.
- [19] S. L. Johnson, P. Beaud, C. J. Milne, F. S. Krasniqi, E. S. Zijlstra, M. E. Garcia, M. Kaiser, D. Grolimund, R. Abela, and G. Ingold, “Nanoscale depth-resolved coherent femtosecond motion in laser-excited bismuth,” *Phys. Rev. Lett.*, vol. 100, no. 15, p. 155501, 2008.
- [20] F. A. Lindemann, “The calculation of molecular vibration frequencies,” *Physik. Z.*, vol. 11, pp. 609–612, 1910.
- [21] P. Stampfli and K. H. Bennemann, “Time-dependence of the laser-induced femtosecond lattice instability of Si and GaAs - role of longitudinal optical distortions,” *Phys. Rev. B*, vol. 49, no. 11, pp. 7299–7305, 1994.
- [22] A. M. Lindenberg, J. Larsson, K. Sokolowski-Tinten, K. J. Gaffney, C. Blome, O. Synnørgren, J. Sheppard, C. Caleman, A. G. MacPhee, D. Weinstein, D. P. Lowney, T. K. Allison, T. Matthews, R. W. Falcone, A. L. Cavalieri, D. M. Fritz, S. H. Lee, P. H. Bucksbaum, D. A. Reis, J. Rudati, P. H. Fuoss,

- C. C. Kao, D. P. Siddons, R. Pahl, J. Als-Nielsen, S. Duesterer, R. Ischebeck, H. Schlarb, H. Schulte-Schrepping, T. Tschentscher, J. Schneider, D. von der Linde, O. Hignette, F. Sette, H. N. Chapman, R. W. Lee, T. N. Hansen, S. Techert, J. S. Wark, M. Bergh, G. Hultdt, D. van der Spoel, N. Timneanu, J. Hajdu, R. A. Akre, E. Bong, P. Krejčík, J. Arthur, S. Brennan, K. Luening, and J. B. Hastings, "Atomic-scale visualization of inertial dynamics," *Science*, vol. 308, no. 5720, pp. 392–395, 2005.
- [23] E. S. Zijlstra, J. Walkenhorst, and M. E. Garcia, "Anharmonic noninertial lattice dynamics during ultrafast nonthermal melting of insb," *Phys. Rev. Lett.*, vol. 101, no. 13, p. 135701, 2008.
- [24] C. Q. Zhang, Y. H. Wei, and C. F. Zhu, "Structural and electronic properties of liquid InSb alloy: An ab initio molecular-dynamics simulation," *Chem. Phys. Lett.*, vol. 408, no. 4-6, pp. 348–353, 2005.
- [25] A. M. Lindenberg, S. Engemann, K. J. Gaffney, K. Sokolowski-Tinten, J. Larsson, P. B. Hillyard, D. A. Reis, D. M. Fritz, J. Arthur, R. A. Akre, M. J. George, A. Deb, P. H. Bucksbaum, J. Hajdu, D. A. Meyer, M. Nicoul, C. Blome, T. Tschentscher, A. L. Cavalieri, R. W. Falcone, S. H. Lee, R. Pahl, J. Rudati, P. H. Fuoss, A. J. Nelson, P. Krejčík, D. P. Siddons, P. Lorazo, and J. B. Hastings, "X-ray diffuse scattering measurements of nucleation dynamics at femtosecond resolution," *Phys. Rev. Lett.*, vol. 100, no. 13, p. 135502, 2008.
- [26] M. Harbst, T. N. Hansen, C. Caleman, W. K. Fullagar, P. Jonsson, P. Sondhaus, O. Synnergren, and J. Larsson, "Studies of resolidification of non-thermally molten InSb using time-resolved X-ray diffraction," *Appl. Phys. A-Mater. Sci. Process.*, vol. 81, no. 5, pp. 893–900, 2005.
- [27] H. Navirian, H. Enquist, T. N. Hansen, A. Mikkelsen, P. Sondhaus, A. Srivastava, A. A. Zakharov, and J. Larsson, "Repetitive ultrafast melting of InSb as an x-ray timing diagnostic," *J. Appl. Phys.*, vol. 103, no. 10, p. 103510, 2008.
- [28] G. S. Zhou, P. M. Fauchet, and A. E. Siegman, "Growth of spontaneous periodic surface-structures on solids during laser illumination," *Phys. Rev. B*, vol. 26, no. 10, pp. 5366–5381, 1982.
- [29] P. M. Fauchet and A. E. Siegman, "Surface ripples on silicon and gallium-arsenide under picosecond laser illumination," *Appl. Phys. Lett.*, vol. 40, no. 9, pp. 824–826, 1982.
- [30] J. E. Sipe, J. F. Young, J. S. Preston, and H. M. Vandriel, "Laser-induced periodic surface-structure .1. theory," *Phys. Rev. B*, vol. 27, no. 2, pp. 1141–1154, 1983.
- [31] R. J. Nelmes, Z. Tun, and W. F. Kuhs, "A compilation of accurate structural parameters for kdp and dkdp, and a users guide to their crystal-structures," *Ferroelectrics*, vol. 71, no. 1-4, pp. 125–141, 1987.

- [32] J. Bornarel, “Domains in kh₂po₄,” *Ferroelectrics*, vol. 71, no. 1-4, pp. 255–268, 1987.
- [33] E. K. H. Salje, *Phase transitions in ferroelastic and co-elastic crystals*. Cambridge University Press, 1990.
- [34] J. Larsson, P. Sondhauss, O. Synnergren, M. Harbst, P. A. Heimann, A. M. Lindenberg, and J. S. Wark, “Time-resolved X-ray diffraction study of the ferroelectric phase-transition in dkdp,” *Chem. Phys.*, vol. 299, no. 2-3, pp. 157–161, 2004.
- [35] J. F. Young and H. M. van Driel, “Ambipolar diffusion of high-density electrons and holes in ge, si, and gaas - many-body effects,” *Phys. Rev. B*, vol. 26, no. 4, pp. 2145–2158, 1982.
- [36] P. Sondhauss, O. Synnergren, T. N. Hansen, S. E. Canton, H. Enquist, A. Srivastava, and J. Larsson, “Metal-like heat conduction in laser-excited InSb probed by picosecond time-resolved x-ray diffraction,” *Phys. Rev. B*, vol. 78, no. 11, p. 115202, 2008.
- [37] A. A. Zholents and M. S. Zolotarev, “Femtosecond x-ray pulses of synchrotron radiation,” *Phys. Rev. Lett.*, vol. 76, pp. 912–915, Feb 1996.
- [38] R. Schoenlein, S. Chattopadhyay, H. Chong, T. Glover, P. Heimann, C. Shank, A. Zholents, and M. Zolotarev, “Generation of femtosecond pulses of synchrotron radiation,” *Science*, vol. 287, pp. 2237–2240, MAR 24 2000.
- [39] G. Ingold, P. Beaud, S. Johnson, A. Streun, T. Schmidt, R. Abela, A. Al-Adwan, D. Abramsohn, M. Böge, D. Grolimund, A. Keller, F. Krasniqi, L. Rivkin, M. Rohrer, T. Schilcher, T. Schmidt, V. Schlott, L. Schulz, F. van der Veen, and D. Zimoch, “Sub-picosecond tunable hard x-ray undulator source for laser/x-ray pump-probe experiments,” *AIP Conference Proceedings*, vol. 879, no. 1, pp. 1198–1201, 2007.
- [40] A. Zholents, P. Heimann, M. Zolotarev, and J. Byrd, “Generation of subpicosecond x-ray pulses using rf orbit deflection,” *Nuclear Instruments and Methods in Physics Research Section A: Accelerators, Spectrometers, Detectors and Associated Equipment*, vol. 425, no. 1-2, pp. 385 – 389, 1999.
- [41] K. Harkay, M. Borland, Y. Chae, G. Decker, R. Dejus, L. Emery, W. Guo, D. Horan, K. Kim, R. Kustom, D. Mills, S. Milton, A. Nassiri, G. Pile, V. Sajaev, S. Shastri, G. Waldschmidt, M. White, B. Yang, and A. Zholents, “Generation of short x-ray pulses using crab cavities at the advanced photon source,” in *2005 IEEE Particle Accelerator Conference (PAC), Vol. 1-4*, IEEE Particle Accelerator Conference, (345 E 47TH ST, NEW YORK, NY 10017 USA), pp. 2514–2516, IEEE, IEEE, 2005. 21st Particle Accelerator Conference (PAC), Knoxville, TN, MAY 16-20, 2005.

- [42] J. Andruszkow, B. Aune, V. Ayvazyan, N. Baboi, R. Bakker, V. Balakin, D. Barni, A. Bazhan, M. Bernard, A. Bosotti, J. Bourdon, W. Brefeld, R. Brinkmann, S. Buhler, J. Carneiro, M. Castellano, P. Castro, L. Catani, S. Chel, Y. Cho, S. Choroba, E. Colby, W. Decking, P. Den Hartog, M. Desmons, M. Dohlus, D. Edwards, H. Edwards, B. Faatz, J. Feldhaus, M. Ferrario, M. Fitch, K. Flottmann, M. Fouaidy, A. Gamp, T. Garvey, C. Gerth, M. Geitz, E. Gluskin, V. Gretchko, U. Hahn, W. Hartung, D. Hubert, M. Huning, R. Ischebek, M. Jablonka, J. Joly, M. Juillard, T. Junquera, P. Jurkiewicz, A. Kabel, J. Kahl, H. Kaiser, T. Kamps, V. Katelev, J. Kirchgessner, M. Korfer, L. Kravchuk, G. Kreps, J. Krzywinski, T. Lokajczyk, R. Lange, B. Leblond, M. Leenen, J. Lesrel, M. Liepe, A. Liero, T. Limberg, R. Lorenz, L. Hua, L. Hai, C. Magne, M. Maslov, G. Materlik, A. Matheisen, J. Menzel, P. Michelato, W. Moller, A. Mosnier, U. Muller, O. Napoly, A. Novokhatski, M. Omeich, H. Padamsee, C. Pagani, F. Peters, B. Petersen, P. Pierini, J. Pfluger, P. Piot, B. Ngoc, L. Plucinski, D. Proch, K. Rehlich, S. Reiche, D. Reschke, I. Reyzl, J. Rosenzweig, J. Rossbach, S. Roth, E. Saldin, W. Sandner, Z. Sanok, H. Schlarb, G. Schmidt, P. Schmuser, J. Schneider, E. Schneidmiller, H. Schreiber, S. Schreiber, P. Schutt, J. Sekutowicz, L. Serafini, D. Sertore, S. Setzer, S. Simrock, B. Sonntag, B. Sparr, F. Stephan, V. Sytchev, S. Tazzari, F. Tazzioli, M. Tigner, M. Timm, M. Tonutti, E. Trakhtenberg, R. Treusch, D. Trines, V. Verzilov, T. Vielitz, V. Vogel, G. Von Walter, R. Wanzenberg, T. Weiland, H. Weise, J. Weisend, M. Wendt, M. Werner, M. White, I. Will, S. Wolff, M. Yurkov, K. Zapfe, P. Zhogolev, and F. Zhou, “First observation of self-amplified spontaneous emission in a free-electron laser at 109 nm wavelength,” *Phys. Rev. Lett.*, vol. 85, pp. 3825–3829, OCT 30 2000.
- [43] P. Emma, R. Akre, J. Arthur, R. Bionta, C. Bostedt, J. Bozek, A. Brachmann, P. Bucksbaum, R. Coffee, F. J. Decker, Y. Ding, D. Dowell, S. Edstrom, A. Fisher, J. Frisch, S. Gilevich, J. Hastings, G. Hays, P. Hering, Z. Huang, R. Iverson, H. Loos, M. Messerschmidt, A. Miahnahri, S. Moeller, H. D. Nuhn, G. Pile, D. Ratner, J. Rzepiela, D. Schultz, T. Smith, P. Stefan, H. Tompkins, J. Turner, J. Welch, W. White, J. Wu, G. Yocky, and J. Galayda, “First lasing and operation of an angstrom-wavelength free-electron laser,” *Nat. Photonics*, vol. 4, pp. 641–647, SEP 2010.
- [44] G. R. Neil, C. L. Bohn, S. V. Benson, G. Biallas, D. Douglas, H. F. Dylla, R. Evans, J. Fugitt, A. Grippo, J. Gubeli, R. Hill, K. Jordan, R. Li, L. Merminga, P. Piot, J. Preble, M. Shinn, T. Siggins, R. Walker, and B. Yunn, “Sustained kilowatt lasing in a free-electron laser with same-cell energy recovery,” *Phys. Rev. Lett.*, vol. 84, pp. 662–665, Jan 2000.
- [45] S. Gruner, D. Bilderback, I. Bazarov, K. Finkelstein, G. Krafft, L. Merminga, H. Padamsee, Q. Shen, C. Sinclair, and M. Tigner, “Energy recovery linacs as synchrotron radiation sources (invited),” *Rev. Sci. Instrum.*, vol. 73, pp. 1402–1406, MAR 2002. 12th National Synchrotron Radiation Instrumentation Conference, MADISON, WISCONSIN, AUG 22, 2001.

- [46] M. M. Murnane, H. C. Kapteyn, M. D. Rosen, and R. W. Falcone, "Ultrafast x-ray pulses from laser-produced plasmas," *Science*, vol. 251, no. 4993, pp. 531–536, 1991.
- [47] T. Feurer, A. Morak, I. Uschmann, C. Ziener, H. Schwöerer, C. Reich, P. Gibbon, E. Forster, R. Sauerbrey, K. Ortner, and C. R. Becker, "Femtosecond silicon K alpha pulses from laser-produced plasmas," *Phys. Rev. E*, vol. 65, no. 1, p. 016412, 2002.
- [48] A. Andersson, M. Eriksson, L. J. Lindgren, P. Rojssel, and S. Werin, "The max-ii synchrotron-radiation storage-ring," *Nucl. Instrum. Methods Phys. Res. Sect. A-Accel. Spectrom. Dect. Assoc. Equip.*, vol. 343, no. 2-3, pp. 644–649, 1994.
- [49] J. Larsson, Z. Chang, E. Judd, P. J. Schuck, R. W. Falcone, P. A. Heimann, H. A. Padmore, H. C. Kapteyn, P. H. Bucksbaum, M. M. Murnane, R. W. Lee, A. Machacek, J. S. Wark, X. Liu, and B. Shan, "Ultrafast x-ray diffraction using a streak-camera detector in averaging mode," *Opt. Lett.*, vol. 22, no. 13, pp. 1012–1014, 1997.
- [50] J. Larsson, P. A. Heimann, A. M. Lindenberg, P. J. Schuck, P. H. Bucksbaum, R. W. Lee, H. A. Padmore, J. S. Wark, and R. W. Falcone, "Ultrafast structural changes measured by time-resolved X-ray diffraction," *Appl. Phys. A-Mater. Sci. Process.*, vol. 66, no. 6, pp. 587–591, 1998.
- [51] A. H. Chin, R. W. Schoenlein, T. E. Glover, P. Balling, W. P. Leemans, and C. V. Shank, "Ultrafast structural dynamics in InSb probed by time-resolved x-ray diffraction," *Phys. Rev. Lett.*, vol. 83, no. 2, pp. 336–339, 1999.
- [52] J. Larsson, "Laser and synchrotron radiation pump-probe x-ray diffraction experiments," *Meas. Sci. Technol.*, vol. 12, no. 11, pp. 1835–1840, 2001.
- [53] A. M. Lindenberg, I. Kang, S. L. Johnson, R. W. Falcone, P. A. Heimann, Z. Chang, R. W. Lee, and J. S. Wark, "Coherent control of phonons probed by time-resolved x-ray diffraction," *Opt. Lett.*, vol. 27, no. 10, pp. 869–871, 2002.
- [54] M. F. DeCamp, D. A. Reis, A. Cavalieri, P. H. Bucksbaum, R. Clarke, R. Merlin, E. M. Dufresne, D. A. Arms, A. M. Lindenberg, A. G. MacPhee, Z. Chang, B. Lings, J. S. Wark, and S. Fahy, "Transient strain driven by a dense electron-hole plasma," *Phys. Rev. Lett.*, vol. 91, no. 16, p. 165502, 2003.
- [55] P. Sondhaus, J. Larsson, M. Harbst, G. A. Naylor, A. Plech, K. Scheidt, O. Synnergren, M. Wulff, and J. S. Wark, "Picosecond x-ray studies of coherent folded acoustic phonons in a multiple quantum well," *Phys. Rev. Lett.*, vol. 94, no. 12, p. 125509, 2005.
- [56] O. Synnergren, T. N. Hansen, S. Canton, H. Enquist, P. Sondhaus, A. Srivastava, and J. Larsson, "Coherent phonon control," *Appl. Phys. Lett.*, vol. 90, no. 17, p. 171929, 2007.

-
- [57] H. Enquist, H. Navirian, T. N. Hansen, A. M. Lindenberg, P. Sondhauss, O. Synergren, J. S. Wark, and J. Larsson, "Large acoustic transients induced by non-thermal melting of insb," *Phys. Rev. Lett.*, vol. 98, no. 22, p. 225502, 2007.
- [58] D. P. Lowney, P. A. Heimann, H. A. Padmore, E. M. Gullikson, A. G. MacPhee, and R. W. Falcone, "Characterization of CsI photocathodes at grazing incidence for use in a unit quantum efficiency x-ray streak camera," *Rev. Sci. Instrum.*, vol. 75, no. 10, pp. 3131–3137, 2004.
- [59] B. L. Henke, J. P. Knauer, and K. Premaratne, "The characterization of x-ray photo-cathodes in the 0.1-10-keV photon energy region," *J. Appl. Phys.*, vol. 52, no. 3, pp. 1509–1520, 1981.
- [60] E. B. Saloman, J. S. Pearlman, and B. L. Henke, "Evaluation of high-efficiency CsI and CuI photo-cathodes for soft-x-ray diagnostics," *Appl. Optics*, vol. 19, no. 5, pp. 749–753, 1980.
- [61] P. Lefur and D. H. Auston, "Kilovolt picosecond optoelectronic switch and pockels cell," *Appl. Phys. Lett.*, vol. 28, no. 1, pp. 21–23, 1976.
- [62] G. Mourou and W. Knox, "A picosecond jitter streak camera," *Appl. Phys. Lett.*, vol. 36, no. 8, pp. 623–626, 1980.
- [63] J. Y. Liu, J. Wang, B. Shan, C. Wang, and Z. H. Chang, "An accumulative x-ray streak camera with sub-600-fs temporal resolution and 50-fs timing jitter," *Appl. Phys. Lett.*, vol. 82, no. 20, pp. 3553–3555, 2003.
- [64] M. M. Murnane, H. C. Kapteyn, and R. W. Falcone, "X-ray streak camera with 2-ps response," *Appl. Phys. Lett.*, vol. 56, no. 20, pp. 1948–1950, 1990.
- [65] J. Larsson, "Ultrafast, jitter-free x-ray streak camera that uses single-photon counting," *Opt. Lett.*, vol. 26, no. 5, pp. 295–297, 2001.
- [66] H. M. Rietveld, "A profile refinement method for nuclear and magnetic structures," *J. Appl. Crystallogr.*, vol. 2, pp. 65–&, 1969.

Comments on my participation

In addition to my contributions to the studies presented above, I have worked on improvements and maintenance of various systems at the D611 beamline at MAX-Lab. I have contributed substantially to the implementation of a new InSb-based x-ray monochromator, thus improving the performance of the beamline. During the course of my work, the existing x-ray streak camera has been modified to achieve sub-picosecond time-resolution. I spent considerable time developing and implementing new detectors at the beamline, such as the time-resolved diffuse x-ray scattering detector presented in Paper I , and the powder diffraction setup described in Paper VI .

Paper I

A new concept to carry out time-resolved diffuse x-ray scattering measurements at a synchrotron x-ray source was demonstrated. The melting and resolidification of InSb following laser excitation was investigated.

I was responsible for implementing the new setup at beamline D611, which was used in this experiment. I was involved in the measurements and data analysis, developed the model and performed the simulations, and wrote large parts of the manuscript.

Paper II

A ferroelectric sample below its Curie temperature was excited using electrical pulses. The resulting stress caused acoustic pulses, influencing the polarization state of the domains in the sample.

I took part in setting up the experiment and carrying out the measurements. I contributed to writing the manuscript.

Paper III

In this study, the influence of the surface structure created by repetitive melting of InSb with short laser pulses was investigated. It was found that ripples were formed

at the surface, affecting x-ray diffraction. This effect is important for x-ray diffraction experiments based on repetitive melting.

I participated in the x-ray diffraction measurements and data analysis. I performed the atomic force microscopy measurements to characterize the sample surface. I contributed to the manuscript.

Paper IV

The improvements in the x-ray streak camera are reported here. A sub-picosecond time resolution and improved quantum efficiency were achieved using a cesium iodide photocathode at grazing incidence and real-time, single-shot data analysis. The performance of the setup was demonstrated with time-resolved x-ray diffraction experiments to study non-thermal melting of InSb and coherent optical phonons in bismuth.

I took part in the development of the subpicosecond x-ray streak camera. I participated in measurements, data analysis, and contributed to the manuscript.

Paper V

In this paper, a concept for measuring time-resolved specular x-ray reflectivity is described. The time resolution was improved from the millisecond to the picosecond range compared to previous experiments. The evolution of the structure of a thin film of amorphous carbon following short-pulse laser excitation was studied, and was interpreted as the result of thermal strain generated by laser excitation and the subsequent relaxation due to the diffusion of heat.

I participated in the measurements and did most of the data analysis. This included the development of software to extract structural information from x-ray reflectivity measurements of multi-layer samples. To understand the changes in thin film structure induced by laser excitation, I developed a model and conducted simulations of the elastic and thermal properties of the sample. I was responsible for the preparation of the manuscript.

Paper VI

I participated in the measurements and did most of the data analysis. This included the development of software to extract structural information from x-ray reflectivity measurements of multi-layer samples. To understand the changes in thin film structure induced by laser excitation, I developed a model and conducted simulations of the elastic and thermal properties of the sample. I was responsible for the preparation of the manuscript.

I participated in the x-ray diffraction measurements and performed the Raman spectroscopy measurements. I analyzed the data and wrote the first draft of the manuscript.

Paper VII

This paper describes the evolution of strain generated by short laser pulses in a graphite crystal using grazing incidence, femtosecond time-resolved x-ray diffraction.

I participated in the measurements and contributed to the manuscript.

Paper VIII

This paper reports on the evolution of surface deformation of x-ray optics induced by the absorption of intense x-ray pulses. This is of importance for the application of x-ray optics in a free electron laser based x-ray source. A surface deformation affects the wavefront of a laser pulse reflected of the surface. The experiment was carried out time-resolved in a x-ray pump - laser probe scheme.

I took part in the measurements at ID09/ESRF and I contributed to writing the manuscript.

Part II

Papers

Paper I

Time-resolved x-ray scattering from laser-molten indium antimonide

R. Nüske, C. v. Korff Schmising, A. Jurgilaitis, H. Enquist, H. Navirian,
P. Sondhauss, and J. Larsson

Department of Physics, Atomic Physics Division, Lund University, P.O. Box 118, Lund SE-221 00, Sweden

(Received 13 November 2009; accepted 16 December 2009; published online 22 January 2010)

We demonstrate a concept to study transient liquids with picosecond time-resolved x-ray scattering in a high-repetition-rate configuration. Femtosecond laser excitation of crystalline indium antimonide (InSb) induces ultrafast melting, which leads to a loss of the long-range order. The remaining local correlations of the liquid result in broad x-ray diffraction rings, which are measured as a function of delay time. After 2 ns the liquid structure factor shows close agreement with that of equilibrated liquid InSb. The measured decay of the liquid scattering intensity corresponds to the resolidification rate of 1 m/s in InSb. © 2010 American Institute of Physics.

[doi:10.1063/1.3290418]

I. INTRODUCTION

Significant advances have been made in picosecond and subpicosecond time-resolved x-ray scattering techniques during the past decade. Experimental efforts have mainly been focused on the observation of nonthermal melting^{1–3} and optical and acoustic phonon motion^{4–8} in *crystalline* solids, while x-ray studies of transient states of *disordered* materials, e.g., liquids, have remained a greater experimental challenge. In contrast to strong Bragg reflections from crystalline material, the liquid state exhibits only weak x-ray scattering amplitudes due to the short correlation length of the disordered structure. The broad features of the liquid structure factor give insight into nearest-neighbor distances and occupation numbers, i.e., directly encode the local structure. Time-resolved liquid x-ray scattering experiments have allowed precise measurements of the reaction pathway of molecules in solution,^{9–12} and have shed light on the dynamic structural changes of liquid water.¹³ The emergence of the liquid phase of InSb after laser-driven nonthermal melting was recently captured directly with femtosecond resolution at the SPPS at the SLAC National Accelerator Laboratory.¹⁴ This study focused on potential voids and ablated material which occur in the scattering pattern at low momentum transfer vectors. It was found that the liquid is formed within 1 ps. Simultaneously, Bragg peaks, indicative of an ordered lattice, disappeared.

In this letter we demonstrate the possibility of carrying out laser-pump/x-ray probe experiments using a two-dimensional (2D) detector at a synchrotron radiation facility with 10 ns bunch spacing and a uniform filling pattern, and report on laser-molten InSb and its subsequent regrowth with a temporal resolution of 400 ps.

II. SETUP FOR TIME-RESOLVED X-RAY SCATTERING

The time-resolved, liquid scattering experiment was carried out at beam line D611 at the MAX-laboratory synchrotron radiation facility in Lund, Sweden. X rays from a bending magnet of the 1.5 GeV MAX-II storage ring are focused

by a toroidal gold-coated mirror and reduced in aperture by a set of slits. The small x-ray incident angle ($\theta_s = 0.9 \pm 0.05^\circ$) leads to an elongated x-ray footprint of $0.1 \times 3.0 \text{ mm}^2$. The x-ray divergence is $3 \times 0.7 \text{ m rad}^2$ (horizontal-vertical), and a multilayer monochromator allows the energy to be set to $E_{x \text{ ray}} = 7.5 \text{ keV}$ with a bandwidth of $\Delta E_{x \text{ ray}}/E_{x \text{ ray}} = 10^{-2}$. A single x-ray probe pulse at the sample contains about 700 photons, and has a duration of approximately 300 ps.

A Ti:Al₂O₃-based femtosecond laser system, operating at a repetition rate of 4.25 kHz, with a 790 nm center wavelength, 4.5 W average power and 45 fs pulse duration, was used for excitation. The optical pump beam was focused by two cylindrical lenses to a spot size of $0.3 \times 4.0 \text{ mm}^2$ [(full width at half maximum (FWHM))] which, assuming a Gaussian beam shape, yielded a fluence of 45 mJ/cm^2 incident on the sample. The laser pulses are synchronized to a particular electron bunch in the storage ring with a jitter below 10 ps.

A. Detection system

To study the diffuse scattering of the liquid phase of InSb a single-photon-counting detection system was designed and set up as shown in Fig. 1. The scattered x rays are converted into visible radiation (center wavelength $\lambda = 425 \text{ nm}$) in a 2-mm-thick plastic scintillator (Saint Gobain, BC-408). The scintillator features a 2.1 ns decay time ($1/e$), and a 0.9 ns rise time (10%–90%), which corresponds to a total 2.5 ns pulse width (FWHM). The conversion efficiency was measured and found to be 60 photons per single 7.5 keV x-ray photon. The spatial resolution of the scintillator for x-ray detection is limited due to the deviations from normal incidence for x rays onto the scintillator and its thickness. This effect sets a lower limit for the Q resolution of the detector. In our case, the spatial resolution is 0.27 mm close to the beamstop, and 2.8 mm at the outer edge of the scintillator. This corresponds to $0.02\text{--}0.20 \text{ \AA}^{-1}$. The Q resolution in our experiment is limited to 0.4 \AA^{-1} at $Q = 3 \text{ \AA}^{-1}$ due to the size of the x-ray spot. A thin aluminum coating ($< 500 \text{ nm}$) on the front of the scintillator blocks any stray light from the pump beam and reflects the generated visible

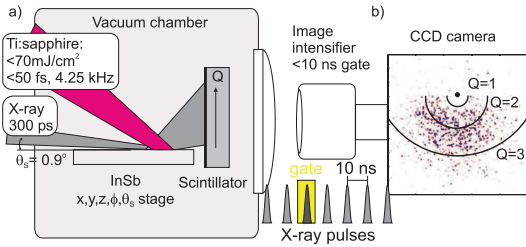


FIG. 1. (Color online) (a) Concept of the time-resolved liquid x-ray scattering setup. The broad scattering rings of liquid InSb are detected by a plastic scintillator. An image intensifier is used to electronically gate single x-ray bunches to achieve a time resolution of one x-ray bunch length plus the timing jitter between the x rays and laser radiation, i.e., approximately 350 ps. b) A typical 2D image of the liquid structure factor at $t=2$ ns; the lines indicate the equivalent scattering vectors, Q .

light toward the detection system. The generated photons from the scintillator are collected with a lens of 7.5 cm focal length and 15 cm diameter at 30 cm distance and imaged onto the photocathode of an image intensifier unit (Hamamatsu C9546). This results in a collection efficiency of 1.4%. The overall image magnification from the scintillator onto the charge-coupled device (CCD) is 1/9. The spatial resolution of the intensifier unit is 45 Lp/mm.

The image intensifier provides signal amplification and has a gating mode with gate times as short as 3 ns, i.e., it allows the selection of a single x-ray bunch synchronized to the laser repetition rate at 4.25 kHz. The minimum available gate time would be short enough to gate out single bunches at synchrotrons with rf frequencies up to 500 MHz, and 2 ns bunch spacing respectively. A scintillator with a sufficiently short pulse width, such as barium fluoride, would be required in this case.

To reach single x-ray photon sensitivity, a second (identical) image intensifier was connected in series, which allowed single, clearly distinguishable scattered x-ray photons to be counted. The maximum photon gain of the intensifier units at the emission wavelength of the scintillator (425 nm) is 3.8×10^3 . The first intensifier was set to gating mode with high gain (900 V), and the second image intensifier was set to moderate gain (700 V) in continuous mode. The accessible voltage range is 600–1000 V.

The 2D scattered intensity is recorded using a thermoelectrically cooled Electron Multiplying CCD camera (Andor iXon). The sensor was cooled to -70 °C and the electron multiplying gain factor was set to 100. In conjunction with the gain from the image intensifiers, single x-ray photon sensitivity was reached. The CCD pixel size is $8\ \mu\text{m}$, the chip area is $8 \times 8\ \text{mm}^2$.

The gain of the detector is sufficient to clearly detect single x-ray photon events. A single photon counting algorithm is used in the data analysis, which limits the signal-to-noise ratio to the shot noise level.

A realistic estimate for the quantum efficiencies of the components can be done as follows: The x-ray absorption at 7.5 keV in the scintillator is 64% and it converts on average into 60 photons, of which 1.4% is collected with the lens. The optical components used transmit in total 74% of the

photons at the scintillators emission wavelength 425 nm. The image intensifier is specified with a quantum efficiency of 10% at the emission wavelength of the scintillator. All in all, it results in a total of 3.9%.

We determined the overall quantum efficiency of the detector using a strongly attenuated Bragg reflection of InSb. The x-ray flux before the scintillator is measured using a calibrated Si x-ray diode (AXUV100GX, International Radiation Detectors) and compared to the x-ray count rate on the 2D detector when the diode is removed. The overall detection efficiency (i.e., the ratio between scattered and detected photons) is measured to be 3.2%.

This detection technique eliminates the necessity for x-ray choppers to select a single x-ray pulse for time resolved x-ray scattering experiments.¹⁵ A hybrid or single bunch filling pattern in the storage ring is not required. It offers a unique alternative to the gateable area pixel array detector PILATUS (gate time 150 ns), which was recently tested in time-resolved x-ray experiments.¹⁶

III. EXPERIMENTAL RESULTS

An InSb wafer [asymmetrically cut at -17° to the (1 1 1) planes] is mounted on a motorized xyz stage, which also allows θ_s and the azimuthal angle φ to be set remotely. The grazing incident geometry allows the x-ray penetration depth, $\xi_{x\text{ ray}} (\approx 90\ \text{nm}$ for $\theta_s=0.9^\circ$ and $E_{x\text{ ray}}=7.5\ \text{keV}$) and the melting depth ξ_{melt} to be matched.¹⁴

Over 100 short exposures with an acquisition times of 5 s alternating with “laser on” and “laser off” settings were measured. This means that the same surface area was molten more than 10^6 times. In order to investigate if this repetitive melting affects the data, we measured the total counts as a function of measuring time. We observed a moderate sublinear increase ($\propto t^{0.6}$) in the total counts as a function of measuring time. In high-repetition-rate melting experiments with moderate melting fluences ($<45\ \text{mJ/cm}^2$) the only observed degeneration is the emergence of small ripple structures below 100 nm in height.¹⁷ Such small surface structures do not adversely affect the scattering geometry, i.e., the matching of the x ray and laser penetration depth.

To control the spatial and temporal overlap of the x-ray probe and the optical pump, the decrease of the intensity of a strong Bragg reflection, e.g., (1 1 1) at $Q=1.68\ \text{\AA}^{-1}$, is monitored. The Bragg condition for different reflections is fulfilled by changing the azimuth angle φ and/or tuning the x-ray energy.¹⁸ We tuned the x-ray energy to 5.4 keV on resonance with the (1 1 1) Bragg reflection from the asymmetrically cut InSb crystal. The gate of the image intensifier is set to include a single x-ray bunch shortly after excitation. If the overlap is good, a decrease in scattered intensity of about 40% is easily detected during an integration time of several seconds. This technique is also used to determine the time-delay zero. During the measurement of the scattering signal from liquid InSb, the Bragg reflection used for the overlap check was attenuated beyond the point where it could be detected, by tuning the x-ray energy off resonance to 7.5 keV. Figure 1(b) shows an example of an image of the difference signal of the integrated laser on and laser off mea-

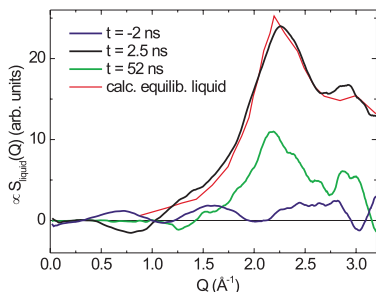


FIG. 2. (Color online) Liquid structure factor $S(Q)$ at various time delays: -2 , $+2.5$, and 52 ns in respect to the laser pulse. Good agreement is seen with an *ab initio* calculation of equilibrated liquid InSb (solid line) (Ref. 19).

measurements. The black lines indicate equivalent scattering vectors Q , where $Q = 4\pi \cdot \sin(\theta) / \lambda$, with the scattering angle 2θ and the x-ray wavelength λ . Q space is calibrated by recording several low-indexed Bragg reflections of InSb. Integration yields the scattering intensity as a function of Q , which is shown in Fig. 2 for different time delays: 2 ns prior, 2.5 ns after, and 52 ns after the laser excitation. Here, the measured number of photons is corrected for the atomic form factor squared and, hence, yields a value directly proportional to the structure factor $S(Q)$. The first broad diffraction ring has its maximum at $Q = 2.2 \text{ \AA}^{-1}$. This is in excellent agreement with an *ab initio* calculation for liquid InSb (red line) for $1 < Q < 3 \text{ \AA}^{-1}$.¹⁹ However, the shoulder at approximately $Q = 3 \text{ \AA}^{-1}$ is more pronounced in the measurement.

Figure 3 shows the integrated scattering intensity for the main and the second peak at $Q = 3 \text{ \AA}^{-1}$ (inset) as a function of delay time. The intensity of the main peak increases more slowly than the temporal resolution of the experiment, and reaches a maximum after approximately 2 ns. It then falls to zero within 100 ns. The integrated scattering intensity of the second peak shows identical temporal behavior within the margin of uncertainty.

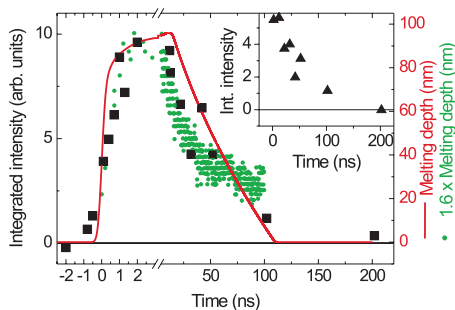


FIG. 3. (Color online) Integrated structure factor $S(Q)$ as a function of time delay. The squares and triangles (inset) correspond to the integrated structure factors of the peak at $Q = 2.2 \text{ \AA}^{-1}$ and $Q = 3 \text{ \AA}^{-1}$, respectively. The melting depth as a function of time (solid line) was calculated using a 1D heat flow equation and reproduces the initial, noninstantaneous melting and the subsequent regrowth of InSb well. Experimental melting depths extracted from a nonthermal melting experiment conducted at a laser fluence of 36 mJ/cm^2 are also shown (dots) (Ref. 21).

IV. DISCUSSION

The good agreement between the integrated, scattered intensity and previously measured and calculated structure factors of equilibrated liquid InSb (Ref. 19) suggests that already after 2 ns the laser-formed liquid has a local structure similar to that of thermalized liquid InSb. Figure 2 shows background-corrected integrated, scattering intensities. The curve for a x-ray bunch 2 ns prior the laser excitation represents the overall noise level for this experiment, since the sample had sufficient time to resolidify and thermalize after the previous laser pulse. The curve for the delay of 2.5 ns shows the integrated scattering intensity from the liquid InSb when it is close to its maximum. After 52 ns the signal has dropped due to resolidification.

The shoulder of the structure factor at $Q = 3 \text{ \AA}^{-1}$ originates from the second nearest neighbor, at $r = 4.3 \text{ \AA}$, of the crystalline zinc blende structure of InSb, and has been interpreted as a covalent Sb–Sb bond in liquid InSb.¹⁹ This pronounced feature is well reproduced in our time-resolved measurements; its decay time unambiguously shows that it indeed arises from liquid InSb (cf. inset of Fig. 3). Because outer coordination shells generally disappear with increasing temperature,²⁰ this feature strongly corroborates the rapid thermalization of laser-molten InSb, i.e., within approximately 2 ns. More precisely, the temporal evolution of the scattering intensity is well explained by a simple one-dimensional (1D) heat flow model (red line in Fig. 3). Noting, that up to the probe depth, $\xi_{x \text{ ray}} \approx 90 \text{ nm}$, the liquid scattering intensity is, to a first approximation, directly proportional to the melting depth, the model identifies the following four time regions of the transient liquid InSb. First, the energy deposited by the laser excitation leads to ultrafast, nonthermal melting of a surface layer with a thickness of $\xi_{\text{melt}} \approx 50 \pm 10 \text{ nm}$.¹ In the second time region, the initial, high temperature gradient then results in rapid redistribution of energy and to subsequent thermal melting of deeper lying layers. This thermally molten volume contributes significantly to the measured scattered intensity, and leads to a noninstantaneous increase within approximately 2 ns. The high standard enthalpy of fusion of InSb initially causes an approximately 130-nm-thick layer at the constant melting temperature, $T_{\text{melt}} = 800 \text{ K}$, directly below the molten surface layer, ξ_{melt} . This delays the conduction of heat and causes the plateau seen in the melting depth in the third time region between 3 and 15 ns. The decrease in the liquid scattering intensity during the subsequent fourth time region corresponds to the resolidification of InSb at a rate of approximately 1 m/s. The model shows best agreement with the measurements when a static sample temperature of 600 K is assumed.²¹ In previous laser-induced melting experiments the formation of the liquid state was inferred by studying the ultrafast decrease of intensity in Bragg reflections,^{1,21} providing complementary information about time-dependent melting depths. Data from Harbst *et al.*²¹ are shown in Fig. 3 as green dots. We attribute the smaller melting depth reported by Harbst *et al.* compared to the simulation of the present experimental conditions to weaker laser excitation

(36 mJ/cm² compared to 45 mJ/cm² in this study). The temporal characteristics reported by Harbst *et al.* are in excellent agreement with our data.

V. SUMMARY

In conclusion, we have demonstrated that time-resolved x-ray scattering experiments on laser-molten disordered InSb can be carried out at a synchrotron radiation facility with a uniform bunch fill pattern. Excellent agreement with previously determined liquid structure factors has been shown. The measured rise and decay times of the liquid scattering amplitude correspond to continued thermal melting and subsequent resolidification, respectively.

ACKNOWLEDGMENTS

The authors would like to thank the Swedish Research Council (VR), the Knut and Alice Wallenberg Foundation, the Crafoord Foundation, the Carl Trygger Foundation, and the European Commission via the Marie Curie Programme for their financial support.

- ¹A. Rouse, C. Rischel, S. Fourmaux, I. Uschmann, S. Sebban, G. Grillon, P. Balcou, E. Foster, J. P. Geindre, P. Audebert, J. C. Gauthier, and D. Hulin, *Nature (London)* **410**, 65 (2001).
- ²K. Sokolowski-Tinten, C. Blome, C. Dietrich, A. Tarasevitch, M. H. von Hoegen, D. von der Linde, A. Cavalleri, J. Squier, and M. Kammler, *Phys. Rev. Lett.* **87**, 225701 (2001).
- ³A. M. Lindenberg, J. Larsson, K. Sokolowski-Tinten, K. J. Gaffney, C. Blome, O. Synnergren, J. Sheppard, C. Caleman, A. G. MacPhee, D. Weinstein, D. P. Lowney, T. K. Allison, T. Matthews, R. W. Falcone, A. L. Cavalieri, D. M. Fritz, S. H. Lee, P. H. Bucksbaum, D. A. Reis, J. Rudati, P. H. Fuoss, C. C. Kao, D. P. Siddons, R. Pahl, J. Als-Nielsen, S. Duesterer, R. Ischebeck, H. Schlarb, H. Schulte-Schrepping, T. Tschentscher, J. Schneider, D. von der Linde, O. Hignette, F. Sette, H. N. Chapman, R. W. Lee, T. N. Hansen, S. Teichert, J. S. Wark, M. Bergh, G. Huld, D. van der Spoel, N. Timneanu, J. Hajdu, R. A. Akre, E. Bong, P. Krejcik, J. Arthur, S. Brennan, K. Luening, and J. B. Hastings, *Science* **308**, 392 (2005).
- ⁴A. M. Lindenberg, I. Kang, S. L. Johnson, T. Missalla, P. A. Heimann, Z. Chang, J. Larsson, P. H. Bucksbaum, H. C. Kapteyn, H. A. Padmore, R. W. Lee, J. S. Wark, and R. W. Falcone, *Phys. Rev. Lett.* **84**, 111 (2000).
- ⁵K. Sokolowski-Tinten, C. Blome, J. Blums, A. Cavalleri, C. Dietrich, A. Tarasevitch, I. Uschmann, E. Forster, M. Kammler, M. Horn-von Hoegen, and D. von der Linde, *Nature (London)* **422**, 287 (2003).
- ⁶M. Bargheer, N. Zhavoronkov, Y. Gritsai, J. C. Woo, D. S. Kim, M. Woerner, and T. Elsaesser, *Science* **306**, 1771 (2004).
- ⁷P. Beaud, S. L. Johnson, A. Streun, R. Abela, D. Abramsohn, D. Grolimund, F. Krasniqi, T. Schmidt, V. Schlott, and G. Ingold, *Phys. Rev. Lett.* **99**, 174801 (2007).
- ⁸C. von Korff Schmising, M. Bargheer, M. Kiel, N. Zhavoronkov, M. Woerner, T. Elsaesser, I. Vrejoiu, D. Hesse, and M. Alexe, *Phys. Rev. Lett.* **98**, 257601 (2007).
- ⁹A. Plech, M. Wulff, S. Bratos, F. Mirloup, R. Vuilleumier, F. Schotte, and P. A. Anfinrud, *Phys. Rev. Lett.* **92**, 125505 (2004).
- ¹⁰H. Ihee, M. Lorenc, T. K. Kim, Q. Y. Kong, M. Cammarata, J. H. Lee, S. Bratos, and M. Wulff, *Science* **309**, 1223 (2005).
- ¹¹J. Vincent, M. Andersson, M. Eklund, A. B. Wohri, M. Odelius, E. Malmberg, Q. Kong, M. Wulff, R. Neutze, and J. Davidsson, *J. Chem. Phys.* **130**, 154502 (2009).
- ¹²M. Christensen, K. Haldrup, K. Bechgaard, R. Feidenhans'l, Q. Kong, M. Cammarata, M. L. Russo, M. Wulff, N. Harrit, and M. M. Nielsen, *J. Am. Chem. Soc.* **131**, 502 (2009).
- ¹³A. M. Lindenberg, Y. Acremann, D. P. Lowney, P. A. Heimann, T. K. Allison, T. Matthews, and R. W. Falcone, *J. Chem. Phys.* **122**, 204507 (2005).
- ¹⁴A. M. Lindenberg, S. Engemann, K. J. Gaffney, K. Sokolowski-Tinten, J. Larsson, P. B. Hillyard, D. A. Reis, D. M. Fritz, J. Arthur, R. A. Akre, M. J. George, A. Deb, P. H. Bucksbaum, J. Hajdu, D. A. Meyer, M. Nicoul, C. Blome, Th. Tschentscher, A. L. Cavalieri, R. W. Falcone, S. H. Lee, R. Pahl, J. Rudati, P. H. Fuoss, A. J. Nelson, P. Krejcik, D. P. Siddons, P. Lorazo, and J. B. Hastings, *Phys. Rev. Lett.* **100**, 135502 (2008).
- ¹⁵M. Cammarata, L. Eybert, F. Ewald, W. Reichenbach, M. Wulff, P. Aninrud, F. Schlotte, A. Plech, Q. Kong, M. Lorenc, B. Lindenau, J. Rübiger, and S. Polachowski, *Rev. Sci. Instrum.* **80**, 015101 (2009).
- ¹⁶T. Ejdrup, H. T. Lemke, K. Haldrup, T. N. Nielsen, D. A. Arms, D. A. Walko, A. Miceli, E. C. Landahl, E. M. Dufresne, and M. M. Nielsen, *J. Synchrotron Radiat.* **16**, 387 (2009).
- ¹⁷H. Navirian, H. Enquist, T. N. Hansen, A. Mikkelsen, P. Sondhaus, A. Srivastava, A. A. Zakharov, and J. Larsson, *J. Appl. Phys.* **103**, 103510 (2008).
- ¹⁸J. Larsson, O. Synnergren, T. N. Hansen, K. Sokolowski-Tinten, S. Werin, C. Caleman, J. Hajdu, J. Sheppard, J. S. Wark, A. M. Lindenberg, K. J. Gaffney, and J. B. Hastings, *Second International Conference on Photo-Induced Phase Transitions: Cooperative, Nonlinear and Functional Properties, Journal of Physics Conference Series*, Opportunities and Challenges Using Short-Pulse X-Ray Sources Vol. 21, edited by M. Buron and E. Collet (Institute of Physics, Bristol, 2005).
- ¹⁹C. Q. Zhang, Y. H. Wei, and C. F. Zhu, *Chem. Phys. Lett.* **408**, 348 (2005).
- ²⁰Q. Wang, C. X. Li, Z. H. Wu, L. W. Wang, X. J. Niu, W. S. Yan, Y. N. Xie, S. Q. Wei, and K. Q. Lu, *J. Chem. Phys.* **128**, 224501 (2008).
- ²¹M. Harbst, T. N. Hansen, C. Caleman, W. K. Fullagar, P. Jonsson, P. Sondhaus, O. Synnergren, and J. Larsson, *Appl. Phys. A: Mater. Sci. Process.* **81**, 893 (2005).

Paper II

Acoustically driven ferroelastic domain switching observed by time-resolved x-ray diffraction

H. Navirian, H. Enquist, R. Nüske, A. Jurgilaitis, C. v. Korff Schmising, P. Sondhauss, and J. Larsson*

Department of Physics, Lund University, P.O. Box 118, SE-221 00 Lund, Sweden

(Received 3 November 2009; revised manuscript received 9 December 2009; published 26 January 2010)

Domain polarization switching in potassium dihydrogen phosphate (KH_2PO_4 , KDP) induced by a propagating strain wave has been observed with time-resolved x-ray diffraction. A pulsed electric field with amplitude of 6 kV/cm and duration of 1 μs was applied along the crystallographic c axis. The field-induced strain waves emanating from the sample surfaces are the result of the converse piezoelectric effect. In the center of the probed surface two waves interfered constructively inducing ferroelastic domain switching, in the absence of an external electric field, at a delay of 3 μs , corresponding to acoustic propagation at a velocity found to be 1500 m/s.

DOI: 10.1103/PhysRevB.81.024113

PACS number(s): 77.65.-j, 61.05.cp, 77.80.Fm, 77.84.Fa

I. INTRODUCTION

Ferroelectric crystals have many applications in both science and technology. They are used, e.g., as components in computer memories,¹ as electro-optical devices,^{2,3} and microsensors.⁴ The relation between the microscopic structure of ferroelectrics and the observed mesoscopic and macroscopic properties has been studied. Optical techniques have been used to study the domain structure and the effects of external electric field, stress, and temperature.⁵⁻⁸

Potassium dihydrogen phosphate (KH_2PO_4 , KDP) was one of the first ferroelectric materials to be discovered, and the theoretical modeling of ferroelectrics is based on studies of this material.^{9,10} Experimental studies of KDP and isomorphs have included optical techniques,¹¹ x-ray scattering,¹² electron-spin resonance,¹³ and neutron scattering.¹⁴ Recently, the piezoelectric effect in paraelectric KDP at room temperature was studied at a third-generation synchrotron facility by Van Reeuwijk *et al.*¹⁵ Grigoriev *et al.*^{16,17} measured the domain dynamics of thin films of $[\text{Pb}(\text{Zr}, \text{Ti})\text{O}_3]$, also known as PZT, which is ferroelectric at room temperature.

In the present work, time-resolved x-ray diffraction was used to study how high-amplitude strain waves induce ferroelastic domain switching in KDP just below the Curie temperature (T_C). Our work does not only demonstrate that it is possible to achieve sufficient amplitudes to induce domain switching but also demonstrates a way to measure the stress-strain relationship in ferroelastic materials. The acoustic strain waves were induced using the converse piezoelectric effect in a manner similar to that used by Van Reeuwijk *et al.* Close to T_C , the piezoelectric modulus is orders of magnitude higher than at room temperature, resulting in large-amplitude Rayleigh waves emanating from the corners when an electric pulse is applied. These strain waves have been observed to induce domain polarization switching. Rayleigh waves both rotate and strain the lattice planes. In the center of a surface though, the rotational components of Rayleigh waves coming from opposite ends compensate each other and only strain remains. This has been confirmed in simulations that are discussed later.

At room-temperature KDP has tetragonal symmetry and belongs to the space group $\bar{I}42d$. When the crystal is cooled below T_C , it undergoes a phase transition to the ferroelectric

phase, which has an orthorhombic symmetry and belongs to the $Fdd2$ space group. The unit-cell dimensions as shown in Fig. 1 are $a=10.5459(9)$ Å, $b=10.4664(10)$ Å, and $c=6.9265(21)$ Å at 20 K below T_C .¹⁸ Unless otherwise stated we will use a coordinate system with axes (x, y, z) parallel to the axes of the ferroelectric unit cell a , b , and c . This will be referred to as the ferroelectric coordinate system as shown in Fig. 1. The standard coordinate system for the paraelectric phase is rotated by 45° around the common z axis compared to the ferroelectric coordinate system. The structural change in KDP at T_C is explained by the double-well potential of the hydrogen bond between the oxygen atoms that link the PO_4 groups. This is discussed in the review article by Nelmes.¹⁹ Above T_C , the hydrogen atoms move freely between the two potential minima. Below it, the thermal energy of the hydrogen atoms is not sufficient to overcome the potential barrier and hence they remain on one side or the other. As a consequence, the hydrogen bonds become asymmetric, which affects the internal structure of the phosphate groups as well as the position of the potassium ion. The structural changes in turn affect the unit cell, which undergoes shear deformation (in the paraelectric coordinate system). The displacement of the phosphor and potassium atoms results in a permanent dipole moment along the c axis. The dipole moments in the

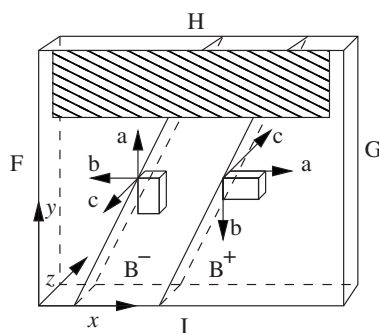


FIG. 1. Sample geometry. The sample was coated with gold electrodes as indicated by the shaded box close to surface H. The orthorhombic unit cell dimensions (a , b , and c) are drawn for the two studied domain types. Sample surfaces are marked as F, G, H, and I.

A^+ and B^+ domains are in the same direction, which is opposite to the direction of the dipole moments in the A^- and B^- domains.

II. EXPERIMENTAL SETUP

The experiment was carried out at beamline D611 at the MAX-laboratory synchrotron facility in Lund (Sweden), which provides x rays in the range 3–10 keV. A double-crystal Si (111) monochromator was used to obtain 4.3 keV x rays with a bandwidth of $\Delta E/E=2.0 \times 10^{-4}$. The x-ray footprint on the sample was $1 \times 0.2 \text{ mm}^2$. The KDP sample had dimensions of $10 \times 10 \times 1 \text{ mm}^3$ along the a , b , and c axes, respectively, and was mounted on a cryogenically cooled manipulation stage so that the position in all three spatial directions, and the incidence angle could be changed. The crystal was cooled to about 3 K below T_C which is known to be 123 K. The temperature was measured by a diode-based temperature sensor mounted in contact with the sample. The measured fluctuations were less than 0.2 K. Any systematic dependence from applying the electric pulses was less than that. However, it is difficult to measure the absolute temperature, so all temperatures are given relative to T_C . The KDP 220 Bragg reflection was studied, where the Miller indices are given in the paraelectric $\bar{4}2d$ basis corresponding to the 400 reflection in the ferroelectric $Fdd2$ basis. This is henceforth referred to as the 400 reflection. The sample was symmetrically cut, i.e., the probed reciprocal-lattice vector was parallel to the surface normal. The Bragg angle was 30° . In this setup the x-ray penetration depth was $6 \mu\text{m}$, limited mainly by absorption.

An electrical field was applied parallel to the c axis by means of gold electrodes which were evaporated directly onto the crystal. Square voltage pulses were applied with a duration of $1 \mu\text{s}$ at a 500 Hz repetition rate. The rise time of the high voltage was on the order of 100 ns. An avalanche photodiode (APD S5343LC5, Hamamatsu) with a time resolution of about 1 ns and active area of 1 mm^2 was used to detect the x rays reflected off the KDP crystal. The x-ray energy was scanned and the diffracted intensity was recorded as a function of time for each energy step using a LeCroy WaveMaster 8500 oscilloscope. Each such transient building up the time-resolved energy scan is the average of 570 events. Scanning the energy is a convenient way of recording a rocking curve as long as there are no absorption edges nearby and the scanning range is small. Scanning the diffraction angle would require scanning of the small fast detector.

III. EXPERIMENTAL METHOD

As can be seen in Fig. 2 the single paraelectric peak splits into four separate peaks in the ferroelectric phase. This is due to the fourfold rotation-inversion ($\bar{4}$) symmetry axis of the paraelectric phase. Thus, there are four different ways in which the structure can be transformed, and hence four possible domain types with a permanent dipole moment can exist below T_C . These domains are termed A^+ , A^- , B^+ , and B^- according to the definition used by Bornarel.²⁰ Below T_C , the 400 reciprocal-lattice vectors of the four domain types

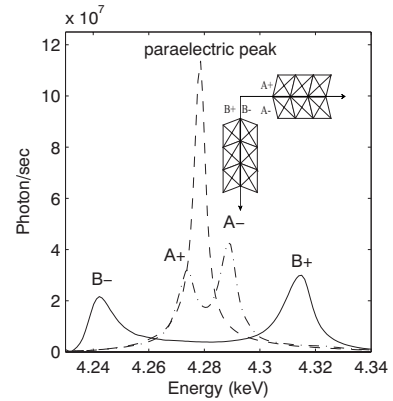


FIG. 2. X-ray energy scan. A paraelectric peak at room temperature (dashed line), B^+ and B^- peaks (solid lines), A^+ and A^- peaks (dashed-dotted line). We also show the domain orientation for the four main domain types (Ref. 20). The representation is in the paraelectric coordinate system.

have different orientations and magnitudes (see Fig. 3). Each of the domains fulfills the Bragg condition at a different x-ray energy for a certain angle of incidence. Figure 2 shows three energy scans at the same angle of incidence. One scan was taken above T_C and shows the paraelectric peak. The other two scans were recorded below T_C and show the ferroelectric peaks. In these two scans the sample has been conditioned by cycling the temperature and by applying a dc field in order to produce either A^+ and A^- domains or B^+ and B^- domains, Fig. 3.

We use the relative intensity of the peaks to measure the volume ratio of the different domain types. The interpretation of the intensity as a measure of the volume ratio is unam-

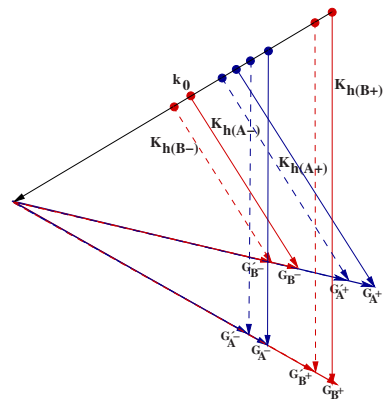


FIG. 3. (Color online) Vector representation of Bragg's law for the different domain types in KDP. The incoming wave vector (K_0) is shown together with the scattered wave vectors ($K_h(B^+)$, $K_h(B^-)$, $K_h(A^+)$, $K_h(A^-)$). The 400 reciprocal-lattice vectors for the different domain types are also drawn as solid lines. A strain modifies the lattice vectors (shown as dashed lines) and thereby the scattering vectors.

biguous under our conditions. First, we have observed experimentally that domains are much smaller than the x-ray footprint on the sample which confirms previous measurements of domain size to be about $10\ \mu\text{m}$ by Bonarel⁶ and others.^{21,22} This excludes the possibility that the intensity variation is due a few large domains moving in and out from the 1 mm probe area. Second there are no effects from x-ray scattering efficiency changes. Since we are making energy scans and the integrated intensity is evaluated, shifts cannot significantly change the intensity of the scattered radiation. Shifts of 5 eV can change the structure factor by only by 0.5% whereas the changes observed are as large as 50%.

IV. MODEL

Applying a homogeneous electric field to a KDP crystal results in homogeneous stress due to the converse piezoelectric effect, giving rise to a homogeneous strain defined by²³

$$\eta_i = d_{ji}E_j, \quad (1)$$

where d_{ji} is the piezoelectric modulus and E_j is the applied electric field.

When the electric field is switched on and off, the relaxation of the piezoelectric stress generates Rayleigh waves that emanate from the corners of the crystal and propagate along the surfaces. In the paraelectric coordinate system the pure shear strain for the initially applied electric field (6 kV/cm) is calculated to be 9×10^{-4} using Eq. (1) and the piezoelectric tensor given by Lüdy.²⁴ In the ferroelectric coordinate system, it corresponds to a tensile strain of 4.5×10^{-4} . The temporal profiles of the acoustic wave essentially mimic the temporal evolution of the electrical pulse. In order to fully understand the acoustic conditions in the experiments, two-dimensional simulations were carried out using the finite element method (FEM). The simulations take into account the piezoelectric and elastic tensors of KDP, the size and orientation of the crystal and the size of the gold coating. Waves propagating along the c axis had been neglected in order to reduce the computational costs. The simulation shows that on the probed surface a Rayleigh surface wave propagates. As expected, we observe that the displacement of the wave is rotating and that the direction of rotation differs between the waves emanating from either edge. At the center of the probed surface, where interference of the two waves occurs the horizontal parts cancel out and a vertical displacement giving rise to a vertical strain remains. The time evolution of the strain at the center of the probed surface is plotted in Fig. 4. The full movie showing the strain propagation is available online.²⁵ The velocity of Rayleigh waves in KDP has been found to be 1500 m/s (Ref. 26) which means that the strain pulses are only 1.5 mm long. The simulations also show that the electric pulses induce bell-mode oscillations in KDP, i.e., resonance of the crystal as a whole. The displacement of an atom by these bell modes can be significant but the strain (the gradient of the displacement) is small for these long-wavelength modes. The strain-generation mechanism is quite similar to the work by Thomsen *et al.*²⁷ who studied laser-induced low-dispersion waves using optical techniques. Later such low-dispersion strain waves have

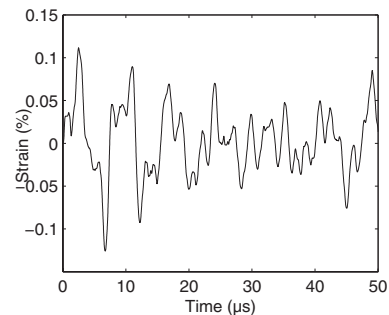


FIG. 4. Simulated evolution of the strain in the probe region from an FEM model. It is in good agreement with the measured shift of the B^+ and B^- peaks.

been extensively studied by x-ray scattering techniques,^{28–32} and the probing techniques for measuring these propagating waves are nearly identical to the work described here.

The strain can experimentally be observed in the energy scans as shifts of the peaks representing the different domain types. As seen in the FEM simulations, the excited acoustic waves do not induce any significant rotation of lattice planes in the middle of the surface H where they are probed. So the change in peak position can be readily used to evaluate the strain.

The tensile stress, σ , can be calculated from the strain using Hook's law and the elastic tensor, C , for the ferroelectric phase

$$\sigma = C\eta. \quad (2)$$

For the geometry employed in this experiment, strain in y direction (η_y) is parallel to the normal of surface H. The stress in y direction is negligible due to the free surface. The strain η_y can be calculated from the tensile stress along the x axis using the elastic tensor using Eq. (2).

Care must be taken not to induce temperature effects via the applied electric field. However, no dc peak shift was observed when applying the pulsed voltage to the sample, which agrees with the temperature sensor measurement. Furthermore the signature is different as a temperature change moves the ferroelectric peaks closer or further away from the center of gravity whereas the acoustic wave moves them in the same direction (toward higher or lower energy, depending on whether it is expansive or compressive strain).

V. MEASUREMENTS AND RESULTS

A time-resolved energy scan showing the effect of the acoustic waves is shown in Fig. 5. The diffracted intensity is coded in false color. The data were obtained by probing the center of the sample. Due to the conditioning of the sample the probe volume consists of only two domain types, B^+ and B^- . The B^+ domains have diffraction peaks at higher energy. The B^+ signal is stronger, indicating that there is a larger volume fraction of B^+ domains in the probe volume. When a voltage of 6 kV/cm is applied with a polarity which we will refer to as positive, an initial shift of each peak is observed.

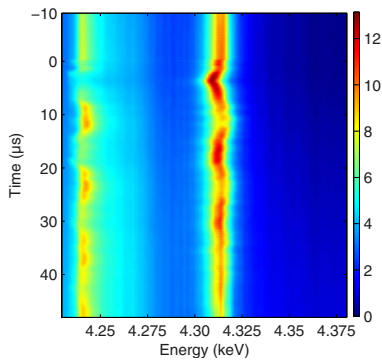


FIG. 5. (Color online) Diffracted intensity as a function of time and x-ray energy. The signal at 4.24 keV corresponds to the B⁻ domain and the signal at 4.31 keV comes from the B⁺ domains. The data were recorded following a positive 600 V pulse with 1 μ s duration starting at time $t=0$. The center of the crystal was probed.

This shift follows the 1 μ s pulse shape of the electrical pulse. This is consistent with a longitudinal wave propagating from the H surface (Fig. 1). Approximately 3 μ s later, a shift is observed which is twice as large. This arises from the interfering Rayleigh waves emanating from the corners. When these waves are reflected at the respective opposite surfaces their phase changes from expansion to compression, and as they travel back to the probe area a shift in the opposite direction is seen. This is repeated several times with a period of 13 μ s determined by the propagation time in the crystal. Knowing the dimensions of the crystal, the speed of the waves in the crystal was calculated to be 1500 m/s, which is in agreement with the room temperature measurement by Bakos *et al.*²⁶ Another striking feature of the data is that expansive strain is accompanied by enhancement of the B⁺ integrated peak intensity and a corresponding decrease in the B⁻ peak, indicating a smaller fraction of B⁻ domains. Similarly, compressive strain induces enhancement of the B⁻ signal at the expense of B⁺ intensity.

In order to understand these observations and to analyze them quantitatively we note that in a ferroelastic material, strain is made up from two contributions. The first is a contribution proportional to the stress and the second one comes from domain reversal. In KDP a full domain reversal corresponds to a 0.76% change in strain. We will from here on refer to these contributions as the linear strain and the ferroelastic strain, respectively. Hence, the amplitude of the linear strain can be evaluated from the shift in the energy of each peak and the amplitude of the ferroelastic strain can be evaluated by the relative integrated peak intensities from the two domain types as shown in Fig. 6. As discussed in the experimental methods section, the integrated intensity of each domain peak is a measure of the fraction of that particular domain type in the probe volume.

Since the electric field is applied along the crystallographic c axis the only nonzero element of the piezoelectric modulus is d_{36} . The matrix element, d_{36} , in the tetragonal paraelectric coordinates couples the electric field along the crystallographic c axis to linear pure shear strain in the plane

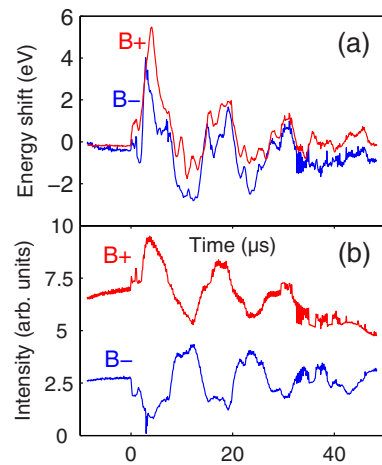


FIG. 6. (Color online) (a) Position and (b) integrated intensity of the diffraction peaks of the B⁺ and B⁻ domains derived from the data in Fig. 5.

normal to the c axis. The piezoelectric modulus, d_{36} has been investigated by Lüdy.²⁴ It shows an anomaly and increases from 23.2 pC/N at 20 °C to 1470 pC/N at T_C which is the value used in our calculations since the temperature variation in d_{36} below T_C is small. The linear shear strain at the applied field of 6 kV/cm can be calculated, and it corresponds to a linear tensile strain of 4.5×10^{-4} corresponding to a tensile stress of 620 N/cm² in the rotated ferroelectric coordinate system. This is in excellent agreement with the present experimental study, where the initial strain from the shift in the energy was found to be 5×10^{-4} . The strain after 3 μ s is twice as large (10^{-3}) since we probed the center of the upper surface, where Rayleigh waves emanating from the top corners of the crystal interfere constructively. Near the surface, this corresponds to a tensile stress perpendicular to the strain which is 3100 N/cm². When probing an area off-center by more than 0.75 mm, where no interference can occur, the peak energy shifts and changes in x-ray intensity are less prominent and more complex due to the rotary displacement vectors which are present. Attempts to induce higher stress by increasing the voltage resulted in sample damage, which was manifested as a crack in the exact center of the crystal where the interference occurred.

The stress-strain relation for ferroelastic materials is described by a hysteresis loop.³³ As shown above, the stress can be calculated from the linear strain. The ferroelastic strain can be derived from the relative integrated peak intensities of the two domain types. Hence we can plot the stress-strain relation from the data in Figs. 5 and 6.

The measured stress-strain relationship of KDP is shown in Fig. 7. The stress was not sufficient to observe actual hysteresis. However, the deviation from linear behavior is obvious. The points in Fig. 7 are experimental data and are built up by all the time points in Fig. 6. The stress (x axis in the Fig. 7) was calculated from the linear strain which was directly measured by the shift in peak energy of the B⁺ domains using Eq. (2). The integrated peak intensities were

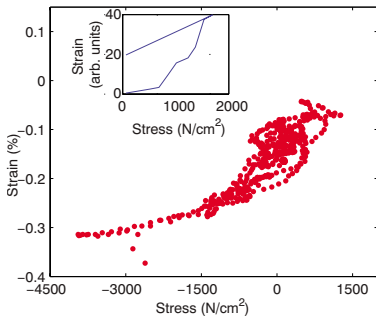


FIG. 7. (Color online) Measured stress-strain relation for KDP at $T_C=3$ K. The data from Ref. 34 is added as an inset.

determined for each time point. They provide the ferroelastic strain which is the main contribution to the strain in Fig. 7. The deviation from a linear stress-strain relation is an indication of ferroelastic hysteresis, although we do not observe a significant difference in strain depending on if stress is increasing or decreasing. The only ferroelastic measurement previously carried out for this brittle material has been added for comparison. That measurement was carried out using electron paramagnetic resonance in Cr^{+3} -doped KDP.³⁴ We show the data from Ref. 35 as an inset to Fig. 7 since the strain scale was arbitrary in that paper.

VI. DISCUSSION

The switching process can be understood from the ideas of Slater⁹ and Yosama and Nagamiya.¹⁰ The Gibbs free energy can be written as

$$U = \frac{1}{2}Na\eta^2 - \varepsilon^s N - \beta\eta(N^+ - N^-) - (N^+ - N^-)\mu E - TS, \quad (3)$$

where N^+ and N^- denote the number of $(\text{H}_2\text{PO}_4)^-$ dipoles in the unit cells belonging to domains with polarity parallel or antiparallel to the c axis, a is a number proportional to the normal elastic constant, and N is the total number of dipoles. The first term stands for the elastic energy, which is the same for both domain types. The second term represents the interaction of dipoles with each other, where ε^s is a constant

parameter. The third term was introduced by Yosama and Nagamiya.¹⁰ It describes a correction to the elastic energy which has opposite signs for the two domain types and β is a constant. This term is the most important when discussing ferroelastic switching. The fourth term was introduced by Slater⁹ to account for the reorientation of domains of dipole moment μ in an external electric field (E). T is the temperature and S is the entropy which is a function of N , N^+ , and N^- .

The domain ratio follows from the minimization of the free energy. In the absence of external fields or forces the crystal will have an equal fraction of domains with opposing polarization in order to compensate the depolarizing fields. In the presence of an external field or forces the equilibrium ratio changes and domain switching occurs in order to minimize the free energy. Domain switching in ferroelectric materials has been studied extensively and has been found to occur in different ways: through nucleation of a reverse polarization domain, through domain propagation in the direction of the electric field, and through domain growth in the direction perpendicular to the electric field.^{15,35}

In our experiment the field is turned off after 1 μs by grounding both electrodes, and the electrodes will rapidly redistribute the surface charges to compensate for the polarization induced by the piezoelectric effect as the strain waves propagate. This means that there is no macroscopic external field present. In Eq. (3), the term including the electric field is zero while the ferroelastic term is independent of the field. Hence, we find that the mechanism responsible for domain switching is ferroelastic rather than ferroelectric. We have experimentally observed that expansive strain is accompanied by the increase in B^+ domains and compressive by that of B^- . This is consistent with the fact that the factor β in Eq. (3) is positive as predicted by the original calculations.¹⁰ In conclusion, we have generated and observed high-amplitude strain waves in the ferroelectric phase of KDP, and that these waves drive domain polarization switching in the absence of an electric field.

ACKNOWLEDGMENTS

The authors would like to thank the Swedish Research Council (VR), the Knut and Alice Wallenberg Foundation, the Crafoord Foundation, the Carl Trygger Foundation, and the European Commission via the Marie Curie Program, for their financial support.

*jörgen.larsson@fysik.lth.se

¹H. Ishiwara, M. Okuyama, and Y. Arimoto, *Ferroelectric Random Access Memories: Fundamentals and Applications* (Springer, New York, 2004).

²S. Liu and X. Min, *Appl. Phys. Lett.* **88**, 143512 (2006).

³D. A. Scrymgeour and V. Gopalan, *Phys. Rev. B* **72**, 024103 (2005).

⁴P. Murali, *J. Micromech. Microeng.* **10**, 136 (2000).

⁵J. Bornarel and R. Cach, *Phys. Rev. B* **60**, 3806 (1999).

⁶J. Bornarel, *J. Appl. Phys.* **43**, 845 (1972).

⁷J. Bornarel and J. Lajzerowicz, *Ferroelectrics* **4**, 177 (1972).

⁸P. Bastie, J. Bornarel, J. Lajzerowicz, M. Vallade, and J. R. Schneider, *Phys. Rev. B* **12**, 5112 (1975).

⁹J. Slater, *J. Chem. Phys.* **9**, 16 (1941).

¹⁰S. Yosama and T. Nagamiya, *Prog. Theor. Phys.* **4**, 263 (1949).

¹¹M. Vallade, *Phys. Rev. B* **12**, 3755 (1975).

¹²K. Ståhl, Å. Kvikic, and S. C. Abrahams, *Acta Crystallogr., Sect. A: Found. Crystallogr.* **46**, 478 (1990).

- ¹³R. C. DuVarney and R. P. Kohin, *Phys. Rev. Lett.* **20**, 259 (1968).
- ¹⁴N. Pérès, M. Souhassou, B. Wyncke, G. Gavoille, A. Cousson, and W. Paulus, *J. Phys.: Condens. Matter* **9**, 6555 (1997).
- ¹⁵S. J. van Reeuwijk, A. Puig-Molina, O. Mathon, R. Tucoulou, and H. Graafsma, *J. Appl. Phys.* **94**, 6708 (2003).
- ¹⁶A. Grigoriev, D.-H. Do, D. M. Kim, C.-B. Eom, B. Adams, E. M. Dufresne, and P. G. Evans, *Phys. Rev. Lett.* **96**, 187601 (2006).
- ¹⁷A. Grigoriev, R. Sichel, H. N. Lee, E. C. Landahl, B. Adams, E. M. Dufresne, and P. G. Evans, *Phys. Rev. Lett.* **100**, 027604 (2008).
- ¹⁸R. J. Nelmes, Z. Tun, and W. F. Kuhs, *Ferroelectrics* **71**, 125 (1987).
- ¹⁹R. J. Nelmes, *Ferroelectrics* **71**, 87 (1987).
- ²⁰J. Bornarel, *Ferroelectrics* **71**, 255 (1987).
- ²¹R. M. Hill and S. K. Ichiki, *Phys. Rev.* **135**, A1640 (1964).
- ²²J. Bornarel and J. Lajzerowicz, *J. Appl. Phys.* **39**, 4339 (1968).
- ²³J. F. Nye, *Physical Properties of Crystals* (Clarendon Press, Oxford, 1957).
- ²⁴W. Lüdy, *Z. Phys.* **113**, 302 (1939).
- ²⁵See supplementary material at <http://link.aps.org/supplemental/10.1103/PhysRevB.81.024113> for a movie showing the strain evolution in the crystal.
- ²⁶J. S. Bakos Zs. Sörlei, Cs. Kuti, and S. Szikora, *Appl. Phys. A: Mater. Sci. Process.* **19**, 59 (1979).
- ²⁷C. Thomsen, H. T. Grahn, H. J. Maris, and J. Tauc, *Phys. Rev. B* **34**, 4129 (1986).
- ²⁸C. Rose-Petruck, R. Jimenez, T. Guo, A. Cavalleri, C. W. Siders, F. Raksi, J. A. Squier, B. C. Walker, K. R. Wilson, and C. P. J. Barty, *Nature (London)* **398**, 310 (1999).
- ²⁹A. M. Lindenberg, I. Kang, S. L. Johnson, T. Missalla, P. A. Heimann, Z. Chang, J. Larsson, P. H. Bucksbaum, H. C. Kapteyn, H. A. Padmore, R. W. Lee, J. S. Wark, and R. W. Falcone, *Phys. Rev. Lett.* **84**, 111 (2000).
- ³⁰P. Sondhauss, O. Synnergren, T. N. Hansen, S. E. Canton, H. Enquist, A. Srivastava, and J. Larsson, *Phys. Rev. B* **78**, 115202 (2008).
- ³¹J. Larsson, A. Allen, P. H. Bucksbaum, R. W. Falcone, A. Lindenberg, G. Naylor, T. Missalla, D. A. Reis, K. Scheidt, A. Sjögren, P. Sondhauss, M. Wulff, and J. S. Wark, *Appl. Phys. A: Mater. Sci. Process.* **75**, 467 (2002).
- ³²P. Sondhauss, J. Larsson, M. Harbst, G. A. Naylor, A. Plech, K. Scheidt, O. Synnergren, M. Wulff, and J. S. Wark, *Phys. Rev. Lett.* **94**, 125509 (2005).
- ³³E. K. H. Salje, *Phase Transition in Ferroelastic and Co-elastic Crystals* (Cambridge University Press, Cambridge, 1990).
- ³⁴T. Kobayashi, *J. Phys. Soc. Jpn.* **35**, 558 (1973).
- ³⁵E. Fatuzzo, *Phys. Rev.* **127**, 1999 (1962).

Paper III

X-ray diffraction from the ripple structures created by femtosecond laser pulses

A. Jurgilaitis · R. Nüske · H. Enquist · H. Navirian ·
P. Sondhauss · J. Larsson

Received: 14 August 2009 / Accepted: 11 January 2010 / Published online: 16 March 2010
© Springer-Verlag 2010

Abstract In this paper, we present the investigation and characterization of the laser-induced surface structure on an asymmetrically cut InSb crystal. We describe diffraction from the ripple surface and present a theoretical model that can be used to simulate X-ray energy scans. The asymmetrically cut InSb sample was irradiated with short-pulse radiation centred at 800 nm, with fluences ranging from 10 to 80 mJ/cm². The irradiated sample surface profile was investigated using optical and atomic force microscopy. We have investigated how laser-induced ripples influence the possibility of studying repetitive melting of solids using X-ray diffraction. The main effects arise from variations in local asymmetry angles, which reduce the attenuation length and increase the X-ray diffraction efficiency.

1 Introduction

Laser-matter interaction has been studied since the 1960s. During the past decade, investigations of time-resolved structural changes in solids using ultrafast X-ray techniques have become an important research field. Laser-induced ultrafast non-thermal melting induced by a laser has been studied using X-ray probes [1–3]. Coherent acoustic phonons [4–6], optical phonons [7] and folded phonon modes in the layered semiconductor structures [8, 9] have also been investigated. Due to insufficient flux of present-day X-ray sources, many of these studies have to be carried

out in repetitive mode. When a laser beam interacts with matter, a series of complex events is triggered. Laser irradiation can excite the solid to a state far from equilibrium. Interesting surface behaviour was observed by Birnbaum [10] when the laser fluence was close to the melting threshold of the material. Spontaneous, highly periodic permanent surface structures or “ripples” can be created on the surface of a solid material irradiated with pulsed or CW light.

Several explanations of the mechanism behind these ripples have been proposed. Emmony et al. [11] first suggested that these ripples were the result of the interference between an incident wave and the wave scattered from imperfections such as dust particles or scratches on the surface. A mechanism for ripple formation from the liquid phase was later proposed by Kerr et al. [12]. According to Sipe et al. [13], the transverse transport of energy following melting with laser radiation is slow. Hence the solid-liquid interface maps the inhomogeneous energy deposition due to interference, reflecting the sine like shape. Laser-induced ripples are classified as S^+ , S^- and c fringes and occur preferentially with three different periodic spacing, given by:

$$\Lambda_{\pm} = \lambda / (1 \pm \sin \theta) \quad \text{and} \quad \Lambda_C = \lambda / \cos \theta, \quad (1)$$

where θ is the angle of incidence of the laser with respect to the surface, and λ is the wavelength of the laser radiation [13]. The wavelength, polarization and incident angle of the laser radiation determine the spatial period. The S^+ and S^- ripples occur perpendicularly to the polarization and have a period given by (1). S^- is usually dominant [14]. The c -type fringes are rarely formed and run parallel to the direction of polarization. It has been found that the ripple structures do not depend on surface orientation, and follow only the laser irradiation direction [15]. The ripple structure is independent of the atmosphere, and is most pronounced

A. Jurgilaitis · R. Nüske · H. Enquist · H. Navirian ·
P. Sondhauss · J. Larsson (✉)
Department of Physics, Lund University, P.O. Box 118,
221 00 Lund, Sweden
e-mail: jorgen.larsson@fysik.lth.se
Fax: +46-46-2224250

at fluences close to the melting threshold [16, 17]. Ripple formation can be directly applied in hard material micromachining due to its precision and lack of ablation, and can also be used to manufacture gratings [18]. The general conclusions in this paper are true for repetitive diffraction studies of opaque materials subjected to high-intensity laser radiation near the damage-threshold.

In the present work, we have studied InSb, which has a narrow bandgap of 0.17 eV at 300 K. The electron mobility is the highest of all semiconductors; typically a factor of 10 higher than that of GaAs [19]. It is therefore a promising candidate for high-speed field effect transistors (FETs) operating at very low supply voltages [20] or as IR emitters and detectors [21–23]. These attractive properties make it important to study and understand InSb.

In a recent study, we investigated the formation of ripples using time-resolved X-ray diffraction, and reported on the conditions under which the melting dynamics of InSb could be studied without being influenced by the ripples. In the present study, we investigated the effect of ripples on X-ray diffraction efficiency and the probe depth in the material at higher fluences and longer exposure times. The measurements were compared with an X-ray diffraction model. This model takes many phenomena into account, including local variations in the asymmetry angle, diffraction from finite crystal sizes, amorphous surface layers and specular reflection from the surface. The model successfully explains diffraction intensity variations in repetitively melted structures [24].

2 Experimental set-up

The experiment was carried out at beam line D611 at the MAX II electron storage ring in Lund, Sweden. Beam line D611 is dedicated to laser-pump/X-ray probe experiments. It has a double-crystal Si monochromator with a bandwidth of $\Delta E/E = 2 \times 10^{-4}$, which operates in the spectral range between 2.5 and 12 keV. A $400 \times 200 \mu\text{m}^2$ X-ray focal spot size can be obtained with $7 \times 0.7 \text{ mrad}^2$ divergence (horizontal \times vertical). The X-ray angle of incidence on the sample was $0.8^\circ \pm 0.05^\circ$ with respect to the surface. The angle was chosen to be similar to that in a non-thermal melting experiment where such a grazing angle is used to reduce the probe depth to match the laser pump depth by absorption in the molten layer. In our experiment, the main benefit of the grazing angle was that the probe was more sensitive to structural changes near the surface. The probe depth is defined as the depth over which the intensity of the incoming X-rays is attenuated by a factor $1/e$. In the scattering geometry used in this study, the absorption depth was 25 nm while the extinction depth was 10 nm. The short laser pulses were generated by a passively mode-locked, titanium-doped sapphire oscillator followed by a cryogenically cooled $\text{Ti:Al}_2\text{O}_3$ multipass

laser amplifier. The amplifier was operated at 4.25 kHz and an average power of 4 W. The wavelength was centred on 800 nm, and the pulse duration was measured and found to be 70 fs. Laser pulses with fluences up to 80 mJ/cm^2 were used to excite the InSb sample, which was mounted on a sample holder, with five degrees of motional freedom. The diffracted signal from the sample was collected with a silicon PIN photodiode. At very high laser fluence, the pattern is deep and can be rather complex, and in this paper we therefore only describe the analysis of data obtained at fluences below 50 mJ/cm^2 .

Laser-induced surface structures on the InSb sample were studied with optical microscopy (OM), atomic force microscopy (AFM) and X-ray diffraction. AFM images were obtained using a commercial scanning probe microscope in tapping mode. The system had a scanning spatial range of $90 \times 90 \mu\text{m}^2$. Our sample topography limited the scan range to $15 \times 15 \mu\text{m}^2$. AFM scans were performed at a low scan rate of 0.2 Hz over a wide area ($10 \times 10 \mu\text{m}^2$ and $15 \times 15 \mu\text{m}^2$). The average time required to obtain one image was about 20 min.

3 Experimental method

Periodic surface structures were created on asymmetrically cut (17° to the (111) plane) InSb samples. The InSb samples were exposed to the laser beam for 60 s. The experimental sample geometry is shown in Fig. 1. X-rays at grazing incidence do not penetrate deep into the crystal and are thus more sensitive to changes in a thin surface layer than X-rays at a steep angle of incidence. The InSb sample was placed in the vacuum chamber and exposed to femtosecond laser pulses at an incidence angle of 15° . The laser beam was p-polarized and had a spot size of $0.6 \times 0.4 \text{ mm}^2$. The beam was scanned over the surface of the sample to irradiate an area of $4 \times 0.4 \text{ mm}^2$. To avoid contaminants such as water deposition, the sample was kept under vacuum between laser exposure and X-ray examination. The X-ray reflectivity was measured in the energy interval 5.1–5.3 keV, while the diffraction angle was kept constant. At laser fluences above the

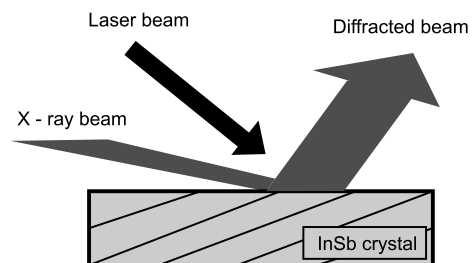


Fig. 1 X-ray diffraction geometry

melting threshold, which is about 30 mJ/cm^2 for InSb, the laser non-thermally melts a thin surface layer on the sample [25]. The molten InSb can resolidify in a crystal structure or freeze in an amorphous phase. X-ray diffraction measurements of laser-irradiated areas show higher peak reflectivity values when the laser fluence approaches the melting threshold. With very high intensity pulses and sufficiently long exposure times the crystal structure is completely destroyed, and the diffracted beam disappears. A study by Harbst et al. showed that under suitable conditions the molten InSb can regrow to form a crystal after femtosecond laser irradiation [24]. The present study confirms this, based on the X-ray diffraction measurements.

4 Results

The ripple structures seen in the OM and AFM images agree qualitatively with known ripple formation models. Ripples started to grow at irradiation fluences above 25 mJ/cm^2 . Figure 2 shows AFM images of some laser-induced surface structures created on InSb irradiated with fluences of 30 mJ/cm^2 and 50 mJ/cm^2 at a laser incidence angle of 15° . At low fluence we observed the pattern shown in Fig. 2(a), which is consistent with that reported by Navirian et al. [25]. At higher fluences these short-period ripples were overgrown by a structure with a periodicity of $6 \mu\text{m}$, as can be seen in Fig. 2(b). This periodicity does not match any of the fringes described in (1) above. However, the periodicity corresponds to a quarter of the S^- periodicity. Ripples of this periodicity have been observed previously [25, 26]. It has been found that the model on which the equation is based is best suited for CW laser exposure, and is less accurate for femtosecond laser pulses [14, 15, 27]. Since the surface structures formed have different heights and periodicities, both OM and AFM were used to extract surface properties such as periodicity, ripple height and surface roughness.

The X-ray reflectivity recorded from an unexposed sample/area was lower than that after laser irradiation with fluences up to 40 mJ/cm^2 . This could be due to the removal of an oxide layer on the crystal surface by the laser pulses. Alternative explanations could be laser annealing, or effects resulting from the periodic surface profile after laser exposure. In the X-ray diffraction energy scans, we observed asymmetric curves on areas with rippled surface structures, while the X-ray diffraction curves from non-irradiated areas were symmetric. Figure 3 shows experimental diffraction curves after laser irradiation at an incidence angle of 15° .

At fluences above 50 mJ/cm^2 , the reflectivity again starts to decrease. This decrease in reflectivity may be due to amorphous surface material and the large number of imperfections arising during crystal regrowth [28]. At laser fluences above 80 mJ/cm^2 , the X-ray reflectivity decreases

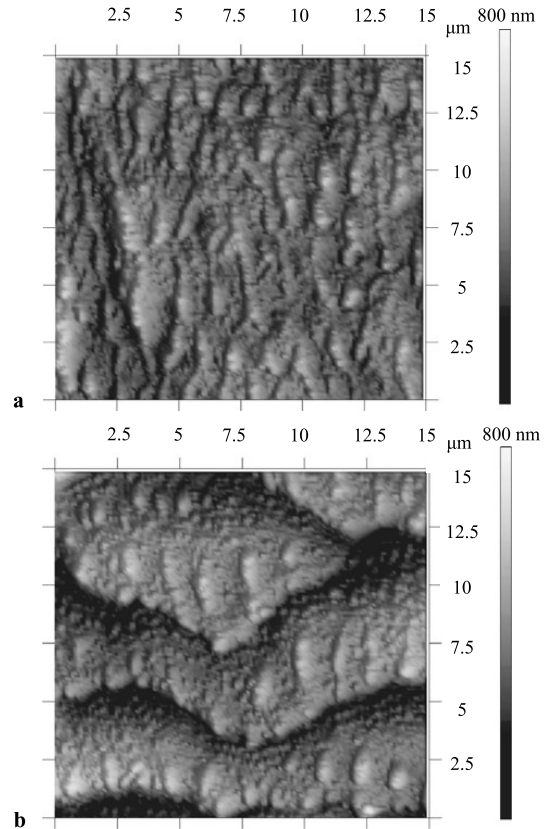


Fig. 2 AFM images showing laser-induced surface structures created by femtosecond laser pulses with fluences of (a) 30 mJ/cm^2 and (b) 50 mJ/cm^2 and a 15° incidence angle. The laser irradiation direction is from the bottom upwards

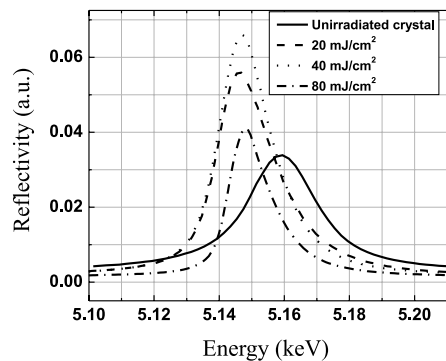


Fig. 3 Measured X-ray diffraction reflection curves (energy scanned at constant angle) from the laser-irradiated area. The sample was irradiated with laser fluences of 20, 40 and 80 mJ/cm^2

even more and disappears due to a thick amorphous layer on top of the surface, and poor InSb surface crystal structure after the laser irradiation.

5 X-ray diffraction modelling

The X-ray energy scans show a much different shape and width compared to the virgin wafer. In order to understand the observed asymmetric curves, the exact shape of the ripples within the probe area had to be taken into account. The procedure for the analysis and modelling is given as a flow-chart in Fig. 4. The details of the modelling are given after a short overview. First, the atomic force microscope was used to obtain a 3D map over the probe area. Second, a computer algorithm was used to extract the local asymmetry of each point on the probe area. A histogram over the asymmetry angles was derived for use in the fourth step. In the third step, X-ray energy scans were simulated for an X-ray energy of 5.12 keV and for the asymmetry angles which were found in step two. In the fourth step, the X-ray energy scans were weighted corresponding to the fraction of the surface with that angle. Finally, the absolute reflectivity was matched by assuming an amorphous layer on top. We now discuss the modelling in detail.

OM and AFM images were used in the first step to create a 3D map of the wafer surface. The AFM provided the local structure of a fraction of the investigated area while the OM provided an overview of the probed sample area. The combined OM and AFM image in Fig. 5 shows the distribution of the ripples over the X-ray-probed area. The surface periodicity and amplitude were obtained directly from the AFM measurements and was used as an input for the modelling. We found the ripple periodicity in this data set to be 6 μm , and the ripple height to be 70 nm. From the OM image, one can see that the ripples do not cover the whole surface, and thus diffraction from both rippled and non-rippled surfaces must be taken into account. Our estimate is that 45% of the surface was covered by ripples.

As a second step of our modelling effort, surface data from the rippled area were extracted from AFM measurements, while the surface that appeared smooth was found to be flat. The transition from rippled to flat surface was modelled by gradually decreasing the ripple height from 70 to 0 nm. To simulate the energy scan, a MATLAB code was developed to perform the calculation and find out the distribution of angles between the laser-modified surface and the incoming X-ray beam. It was found that the angle can vary by up to 10°, depending on the ripple height and periodicity.

The third step of modelling involved X-ray diffraction simulations. The X-ray reflectivity from the virgin wafer was obtained by simulating X-ray energy scans for an X-ray energy of 5.12 keV and a 17° angle of asymmetry, i.e. the

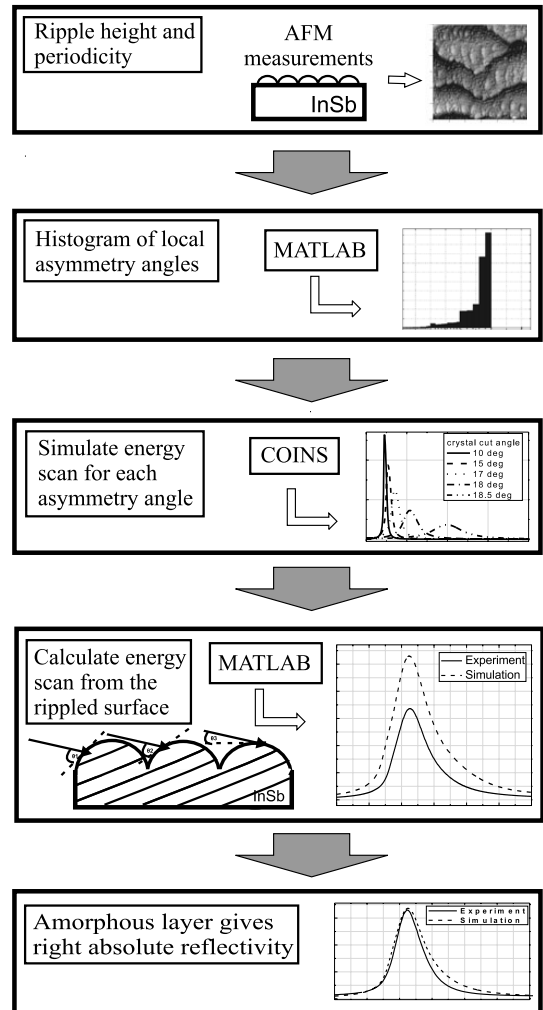


Fig. 4 A flow chart describing the steps in the X-ray diffraction modelling. The surface structure was measured by AFM, subsequently the distribution of asymmetry angles were calculated. Energy scans were calculated for a range of asymmetry angles and these scans were weighted in order to obtain energy scans which could be compared to the experimental data. To match the absolute reflectivity an amorphous layer on the top was introduced

angle of Bragg planes with respect to the surface. X-ray diffraction from perfect or distorted crystals can be described by the Takagi–Taupin equations [29, 30]. These equations are derived from Maxwell’s equations in the periodic structure of a crystal, and are valid for a wide range of distortions and diffraction geometries. The program COINS was used for these simulations. It is based on the dynamical theory of diffraction and uses generalized Takagi–Taupin equations [31].

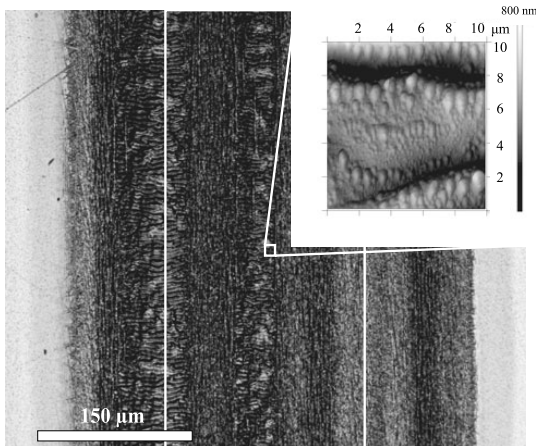


Fig. 5 OM image and AFM image (*inset*) showing the X-ray probed area which was irradiated with a laser fluence of 40 mJ/cm^2 at an incident angle of 15°

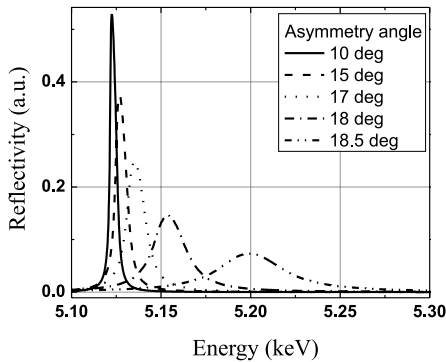


Fig. 6 Simulated energy scans from a perfect InSb crystal for different asymmetry angles

In order to simulate the effects of the laser-induced rippled structure, X-ray reflectivity from perfect InSb crystal was simulated (COINS) with varying angles of asymmetry. Figure 6 shows the evolution of the reflection curve as the angle of asymmetry changes/increases. Based on the distribution of the X-ray incidence angle, energy scans were simulated for asymmetry angles between 0° and 18.6° , where 0° corresponds to InSb lattice planes parallel to the sample surface. Asymmetry angles larger than the Bragg angle (18.6°) were not modelled since in this case, the diffracted X-rays cannot leave the sample. The reflection peak moves to the low-energy side and becomes narrower as the asymmetry angle becomes smaller. At grazing incidence the amplitude falls due to X-ray absorption, and the peak moves to the high-energy side due to refraction at the surface. Above 17° broadening of the curve is observed, which is directly related

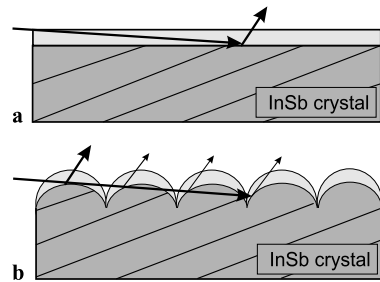


Fig. 7 (a) X-ray path through a flat crystal with a molten surface layer. (b) X-ray path through a crystal with ripples with a molten surface layer, showing multiple diffraction from consecutive ripples

to the X-ray penetration depth. The smaller the penetration depth, i.e. the thinner the diffracting layer, the broader the diffraction peak.

In the fourth step of modelling, the contribution from the different asymmetry angles were weighted according to the ripple map obtained from the AFM measurement using a MATLAB post-processor which resulted in energy scans which could be directly compared to the experimental data. The MATLAB code was designed as a ray-tracing code in order to include other effects which influence the absolute integrated reflectivity such as losses by specular reflection and attenuation of X-rays as they propagate through one ripple to be reflected by the next one (compare Fig. 7(a) and 7(b)). X-ray beams which were attenuated by propagation through three or more ripples were neglected.

Another effect which influences the absolute reflectivity is the formation of an amorphous or poly-crystalline layer on the top of the crystal. The thickness of the amorphous layer is difficult to measure directly. Therefore, the inverse problem was solved, i.e. the thickness of the amorphous layer required to reproduce the measured absolute integrated X-ray reflectivity was determined. For an incidence angle of 15° and a laser fluence of 40 mJ/cm^2 , the thickness was 20 nm. For fluences between 15 mJ/cm^2 and 60 mJ/cm^2 , thicknesses between 0 and 30 nm were found, which is in good agreement with other studies [24].

After this fifth step, good agreement between model and data was found as seen in Fig. 8. In Fig. 8(a), it can be seen that the ripples actually increase the integrated X-ray reflectivity. Figure 8(b) shows the comparison between the simulations and experimental data.

6 Interpretation

The simulations suggest that the shape of the energy scan from the laser-irradiated sample is determined mainly by local variations in the asymmetry angle. The X-ray reflectivity is reduced mainly by the presence of an amorphous surface

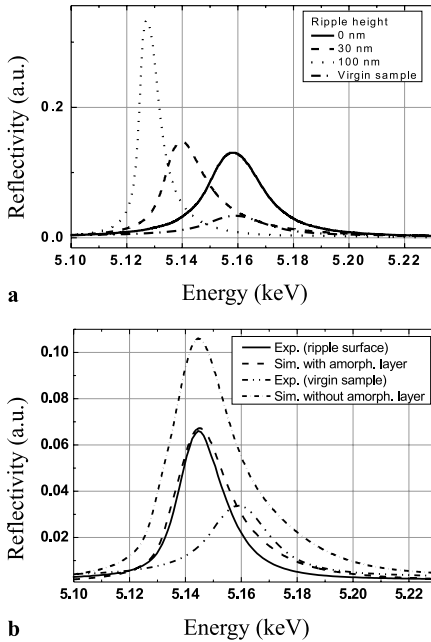


Fig. 8 (a) Simulated energy scans from rippled InSb crystal surfaces with different ripple heights. (b) Simulated and measured energy scans for a wafer exposed to a laser fluence of 40 mJ/cm² at an incident angle of 15°

layer. At higher laser fluence (>50 mJ/cm²) the amorphous layer becomes thicker, and thus the X-ray reflectivity decreases. The obtained experimental X-ray reflection curves were also asymmetric and fit the simulated weighted average curve well. Since the ripple height increases with irradiation fluence, a situation will arise where every X-ray beam passes through several ripples before being reflected. In a grazing geometry, this occurs when the height of the ripples is greater than 30 nm. The effects of laser generated ripples on X-ray diffraction are undesirable in many laser-pump/X-ray probe experiments with high laser fluence. An example is non-thermal melting of InSb in repetitive mode, i.e. if the sample is melted and regrown thousands (or even millions) of times. X-ray studies on non-thermal melting rely on the X-rays being attenuated by the molten layer. The asymmetrically cut crystal helps by increasing the path length through the molten layer, hence increasing X-ray attenuation. At the beginning of the exposure, the sample is flat, and a large X-ray path length can be achieved. After prolonged exposure, ripples are formed. Since this changes the asymmetry angle locally, a higher sample reflectivity is obtained at the expense of the sensitivity to the molten layer. The laser-induced local asymmetry variations thus reduce the surface sensitivity. Figure 9 illustrates this effect. The simulation of diffraction from a flat, asymmetrically cut (17°) InSb sample

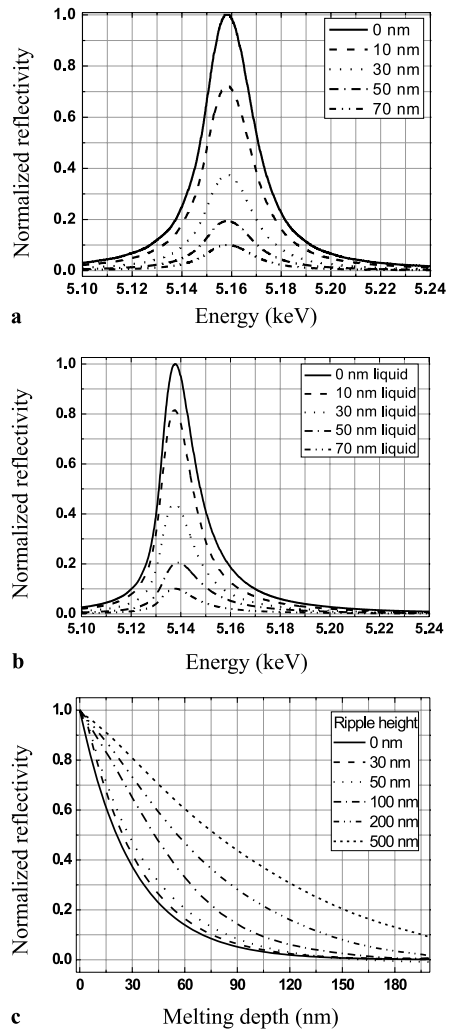


Fig. 9 Simulated energy scans from the asymmetrically cut InSb surfaces with a liquid top layer: (a) shows the expected reflectivity for a smooth surface; (b) shows the expected reflectivity if the surface is modulated by 30 nm high ripples; (c) shows the simulated X-ray reflectivity as a function of melting depth

is shown in Fig. 9(a). To determine whether melting could be detected by monitoring the X-ray intensity, a molten layer with a thickness varying from 0 to 70 nm was added. A similar simulation for a sample with sinusoidal ripples on the surface is shown in Fig. 9(b). The integrated reflectivity as function of melting depth for different ripple heights is shown in Fig. 9(c). The total attenuations was modelled by averaging the attenuation over all local asymmetry angles in

the probed area taking into account the absorption by propagation through multiple ripples before diffraction.

Non-thermal melting occurs within 1 ps and melts about 30–50 nm depending on the laser fluence. Due to high enthalpy of the InSb there is a thick (about 100 nm) layer of hot InSb beneath the molten layer. A part of this layer melts thermally at later times. Hence the sensitivity for non-thermal melting will be significantly reduced by the ripples, whereas the slower non-thermal melting which is deeper is less sensitive. Since the ripple height grows with integrated exposure time, the integration time in a repetitive non-thermal melting experiment will be limited. The maximum exposure time will depend on the laser fluence and the X-ray diffraction geometry.

7 Conclusions

We have observed how surface structures created by femtosecond laser pulses influence the surface sensitivity in an X-ray diffraction measurement. The laser-induced ripples were studied with AFM, OM and X-ray diffraction. The surface properties extracted from the AFM measurements were used as input to X-ray diffraction simulations. The main conclusion is when the local asymmetry angles vary, the surface sensitivity is decreased. It is important to keep track of laser-induced periodic structures in order to facilitate laser-pump/X-ray probe measurements in repetitive mode. In our measurements on InSb, the experimental results show that the strongest ripple growth occurs when the laser fluence is close to the melting threshold, i.e. $> 30 \text{ mJ/cm}^2$. At higher fluences ($> 50 \text{ mJ/cm}^2$) an amorphous layer is formed reducing the X-ray reflectivity. The measured X-ray reflection curves were asymmetric. This effect could be explained by local variations in the angle between the surface and incident X-ray beam due to the ripple structure. For fluences below 30 mJ/cm^2 , the lattice regrows and the crystal is restored, even after many millions of shots. This allows non-thermal melting experiments to be carried out in repetitive mode, but care must be taken as ripples exceeding 30 nm influence the surface sensitivity.

Acknowledgements The authors acknowledge the Swedish Research Council (VR), the Knut and Alice Wallenberg Foundation, the Crafoord Foundation, the Carl Trygger Foundation and the European Commission via the Marie Curie Programme, for their financial support.

References

1. A. Rousse, C. Rischel, S. Fourmaux, I. Uschmann, S. Sebban, G. Grillon, Ph. Balcou, E. Förster, J.P. Geindre, P. Audebert, J.C. Gauthier, D. Hulin, *Nature (Lond.)* **410**, 65 (2001)

2. A.M. Lindenberg, J. Larsson, K. Sokolowski-Tinten, K.J. Gaffney, C. Blome, O. Synnergren, J. Sheppard, C. Coleman, A.G. MacPhee, D. Weinstein, D.P. Lowney, T.K. Allison, T. Matthews, R.W. Falcone, A.L. Cavalieri, D.M. Fritz, S.H. Lee, P.H. Bucksbaum, D.A. Reis, J. Rudati, P.H. Fuoss, C.C. Kao, D.P. Siddons, R. Pahl, J. Als-Nielsen, S. Duesterer, R. Ischebeck, H. Schlarb, H. Schulte-Schrepping, Th. Tschentscher, J. Schneider, D. von der Linde, O. Hignette, F. Sette, H.N. Chapman, R.W. Lee, T.N. Hansen, S. Techert, J.S. Wark, M. Bergh, G. Hultdt, D. van der Spoel, N. Timneanu, J. Hajdu, R.A. Akre, E. Bong, P. Krejčík, J. Arthur, S. Brennan, K. Luening, J.B. Hastings, *Science* **308**, 392 (2005)
3. C.W. Siders, A. Cavalleri, K. Sokolowski-Tinten, Cs. Tóth, T. Guo, M. Kammler, M. Horn von Hoegen, K.R. Wilson, D. von der Linde, C.P.J. Barty, *Science* **286**, 1340 (1999)
4. C. Thomsen, H.T. Grahn, H.J. Maris, J. Tauc, *Phys. Rev. B* **34**, 4129 (1986)
5. A.M. Lindenberg, I. Kang, S.L. Johnson, T. Missalla, P.A. Heimann, Z. Chang, J. Larsson, P.H. Bucksbaum, H.C. Kapteyn, H.A. Padmore, R.W. Lee, J.S. Wark, R.W. Falcone, *Phys. Rev. Lett.* **84**, 111 (2000)
6. J. Larsson, A. Allen, P.H. Bucksbaum, R.W. Falcone, A. Lindenberg, G. Naylor, T. Missalla, D.A. Reis, K. Scheidt, A. Sjogren, M. Wulff, P. Sondhauss, J.S. Wark, *Appl. Phys. A* **75**, 467 (2002)
7. K. Sokolowski-Tinten, C. Blome, J. Blums, A. Cavalleri, C. Dietrich, A. Tarasevitch, I. Uschmann, E. Förster, M. Kammler, M. Horn-von-Hoegen, D. von der Linde, *Nature (Lond.)* **422**, 287 (2003)
8. M. Bargheer, N. Zhavoronkov, Y. Gritsai, J.C. Woo, D.S. Kim, M. Woerner, T. Elsaesser, *Science* **306**, 1771 (2004)
9. P. Sondhauss, J. Larsson, M. Harbst, G.A. Naylor, A. Plech, K. Scheidt, O. Synnergren, M. Wulff, J.S. Wark, *Phys. Rev. Lett.* **94**, 125509 (2005)
10. M. Birnbaum, *J. Appl. Phys.* **36**, 3688 (1965)
11. D.C. Emmony, R.P. Hawson, L.J. Willis, *Appl. Phys. Lett.* **23**, 598 (1973)
12. N.C. Kerr, B.A. Omar, S.E. Clark, D.C. Emmony, *J. Appl. Phys.* **23**, 884 (1990)
13. J.E. Sipe, J.F. Young, J.S. Preston, H.M. van Driel, *Phys. Rev. B* **27**, 1141 (1983)
14. X.C. Wang, G.C. Lim, F.L. Ng, W. Liu, S.J. Chua, *Appl. Surf. Sci.* **252**, 1492 (2005)
15. H.J. Leamy, G.A. Rozgonyi, T.T. Sheng, G.K. Celler, *Appl. Phys. Lett.* **32**, 535 (1978)
16. A.K. Jain, V.N. Kulkarni, D.K. Sood, J.S. Uppal, *J. Appl. Phys.* **52**, 4882 (1981)
17. Z. Guosheng, P.M. Fauchet, A.E. Siegman, *Phys. Rev. B* **26**, 5366 (1982)
18. A.Y. Vorobyev, C. Guo, *Appl. Phys. Lett.* **92**, 041914 (2008)
19. B.R. Bennet, R. Magno, J.B. Boos, W. Kruppa, M.G. Ancona, *Solid. State Electron.* **49**, 1875 (2005)
20. T. Ashley, A.B. Dean, C.T. Elliott, G.J. Pryce, A.D. Johnson, H. Willis, *Appl. Phys. Lett.* **66**, 481 (1995)
21. D.G. Avery, D.W. Goodwin, A.E. Rennie, *J. Sci. Inst.* **34**, 394 (1957)
22. A.N. Vystavkin, Yu.I. Kolesov, N.N. Listvin, A.Ya. Smirnov, *IEEE Trans. Microwave Theory Tech.* **22**, 1041 (1974)
23. I. Kimukin, N. Biyikli, E. Ozbay, *J. Appl. Phys.* **94**, 5414 (2003)
24. M. Harbst, T.N. Hansen, C. Coleman, W.K. Fullagar, P. Jonsson, P. Sondhauss, O. Synnergren, J. Larsson, *Appl. Phys. A* **81**, 893 (2005)

25. H. Navirian, H. Enquist, T.N. Hansen, A. Mikkelsen, P. Sondhauss, A. Srivastava, A.A. Zakharov, J. Larsson, *J. Appl. Phys.* **103**, 103510 (2008)
26. R. Wagner, J. Gottmann, A. Horn, E.W. Kreutz, *Appl. Surf. Sci.* **252**, 8576 (2006)
27. J. Bonse, M. Munz, H. Sturm, *J. Appl. Phys.* **97**, 013538 (2005)
28. I.L. Shumay, U. Hofer, *Phys. Rev. B* **53**, 15878 (1996)
29. S. Takagi, *J. Phys. Soc. Jpn.* **26**, 1239 (1969)
30. D. Taupin, *Bull. Soc. Fr. Mineral. Crystalogr.* **87**, 469 (1964)
31. P. Sondhauss, J.S. Wark, *Acta Cryst. A* **59**, 7 (2003)

Paper IV

Subpicosecond hard x-ray streak camera using single-photon counting

Henrik Enquist,^{1,2} Hengameh Navirian,¹ Ralf Nüske,¹ Clemens von Korff Schmising,¹ Andrius Jurgilaitis,¹ Marc Herzog,³ Matias Bargheer,³ Peter Sondhaus,² and Jörgen Larsson^{1,*}

¹Atomic Physics Division, Department of Physics, Lund University, P.O. Box 118, SE-221 00 Lund, Sweden

²MAX-lab, Lund University, Lund, Sweden

³Institut für Physik und Astronomie, Universität Potsdam, Potsdam, Germany

*Corresponding author: jorgen.larsson@fysik.lth.se

Received June 7, 2010; revised August 19, 2010; accepted August 24, 2010;
posted September 7, 2010 (Doc. ID 129590); published September 22, 2010

We have developed and characterized a hard x-ray accumulating streak camera that achieves subpicosecond time resolution by using single-photon counting. A high repetition rate of 2 kHz was achieved by use of a readout camera with built-in image processing capabilities. The effects of sweep jitter were removed by using a UV timing reference. The use of single-photon counting allows the camera to reach a high quantum efficiency by not limiting the divergence of the photoelectrons. © 2010 Optical Society of America

OCIS codes: 040.1490, 040.7480, 100.0118, 150.6044, 340.6720.

Time-resolved x-ray diffraction has become a standard tool for studies of the dynamics of laser excited solids [1]. Synchrotron radiation sources operating in standard mode produce high brilliance x-ray beams, but the time duration of the pulses is in the 50–500 ps range. Any experiment requiring better time resolution will need to rely on a fast detector. Streak cameras have been reported to give a time resolution down to 233 fs [2] for UV radiation in the accumulating mode and 350 fs using 1.5 keV x rays [3] in the single-shot mode. This time resolution is, however, not yet reached for hard x rays. The fastest streak cameras rely on limiting the divergence of the photoelectrons [4]. This implies a severe reduction in quantum efficiency.

In time-resolved x-ray diffraction experiments carried out at third-generation electron storage rings, the number of photons per pulse is relatively small and operation in the accumulating mode is necessary. The mechanisms limiting the time resolution of a streak camera are described in detail elsewhere [3–5]. The main factors are the sweep speed, the size of the input slit, the aberrations of the electron optics, and the energy spread of the photoelectrons. The field generated by the sweep plates also introduces additional dispersion [4,6].

In this Letter we describe an x-ray streak camera that uses single-photon counting to reduce the effects of dispersion and imperfect imaging. Images are analyzed in real time, and a UV timing reference is used to track and compensate the sweep jitter. The use of a readout camera with built-in image processing capabilities reduces the bandwidth required to transfer data to the host computer. Thus a frame rate of 2 kHz can be reached. The concept of a single-photon counting camera was first proposed by Murnane *et al.* [7], and a proof-of-principle demonstration was published by Larsson [8], who improved the time resolution of a commercial streak camera from 5 to 1.5 ps.

A set of experiments to demonstrate the performance of the streak camera was conducted at beamline D611 at the MAX-lab synchrotron radiation facility. This bending magnet beamline is designed for laser pump–x-ray probe experiments and produces about 5000 photons per pulse and

0.02% bandwidth. The pulse duration is 500 ps. A Ti:Al₂O₃ femtosecond laser system, operating at a repetition rate of 4.25 kHz, with a 790 nm center wavelength and 45 fs pulse duration was used for the measurements. The laser beam was split into three arms. Laser pulses with an energy of 100 μJ were used to trigger a photoconducting switch that generates the high voltage sweep ramp for the streak camera. Part of the pulse (200 μJ) was used to generate the third harmonic, which was sent onto the photocathode as a timing reference. Up to 700 μJ was available to pump the sample. The streak camera was mounted with a 100-μm-wide CsI photocathode in a 6° grazing incidence configuration [9]. Electrons were accelerated, using a mesh with a >90% open area ratio, to 8 kV over a gap of 2 mm. Subsequently, electrons were imaged from the cathode to a microchannel plate (MCP) with gain larger than 10⁸, enabling a single photoelectron emitted from the cathode to be detected by the readout camera. Thus, the overall quantum efficiency of the streak camera equals that of the photocathode. The quantum efficiency was deduced by measuring the photon flux using a calibrated x-ray diode and comparing it with the single-photon count rate and was found to be larger than 10%. The readout camera (Mikrotron MC1364) uses a complementary metal-oxide semiconductor sensor and has an embedded FPGA image processor that can perform a large part of the image analysis. This enables images to be analyzed in real time at frame rates of several kilohertz.

We will now discuss how single-photon counting in the accumulating mode can increase the temporal resolution compared to the single-shot mode [7,8]. The x rays are sent onto the photocathode together with a UV pulse derived from the same laser that is used to pump the sample. Each incident x-ray photon generates up to 20 photoelectrons [10]. If the aperture of the streak camera is not constrained, many of the photoelectrons can propagate to the MCP. Because of dispersion and imaging errors, electrons will travel individual trajectories and be imaged as a spot that can be irregular in shape. The idea behind single-photon counting is that the center of each spot can be determined with an accuracy smaller than the spot size. The uncertainty of the center position depends on the number

of detected photoelectrons per photon, and, hence, it is important to keep as many as possible to minimize statistical variations. Typically four photoelectrons per x-ray photon are detected. Each sweep generates an image in which all spots corresponding to photon events are found, and their center of gravity is determined. The UV pulse consists of several hundred photoelectrons, and its position can be determined with high precision and is used as a timing fiducial. As this pulse has a known fixed delay relative to the pump pulse, the position of this pulse can be used to remove the shot-to-shot jitter in the processed data.

To test the system, a second UV pulse was generated by splitting off part of the power in the reference beam. This second beam was then used as a simulated x-ray signal at a fixed delay of 8 ps. Figure 1(a) shows a gray scale image averaged for 1 s at a repetition rate of 4.25 kHz. The time resolution in this particular image is 2.5 ps. When the pulses are accumulated using the single-photon counting mode, the time resolution measured as the FWHM is 280 fs. The vast improvement can be seen in Fig. 1(b).

In the following we demonstrate the effective time resolution of our streak camera for hard x-ray pulses by repeating three previously performed ultrafast diffraction experiments.

The structural rearrangements associated to ultrafast melting of semiconductors, such as InSb, has previously been studied [11,12]. The disordering can be detected as a fast drop of x-ray diffraction efficiency [12]. An asymmetrically cut InSb sample was illuminated with laser pulses with a fluence of 38 mJ/cm^2 . The incidence angle between laser and sample surface was 15° . The disordering was probed by x rays with a photon energy of 3.15 keV at an incidence angle of 0.9° and a bandwidth of 2%. The intensity of the (111) reflection was recorded. The sample was continuously translated to exchange the surface in order to avoid effects from ripple formation [13]. At the translation speed of 1 mm/s, the ripples did not reach a high enough amplitude to influence the measurement. This limited the data acquisition time to 30 s. Figure 2 shows the drop in x-ray diffraction as recorded by the streak camera in the single-photon counting mode. The curve was fitted to an error function, yielding an upper bound of 640 fs for the 90% to 10% fall time. The fall time of the (111) reflection has been measured at 430 fs [12]. A

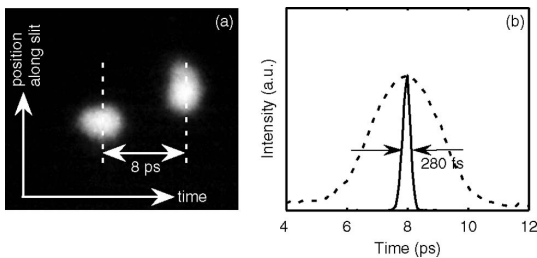


Fig. 1. Images showing two UV pulses separated by 8 ps. (a) Gray scale image of averaging mode and (b) lineout in averaging mode (dashed curve) and photon counting mode (solid curve). In the photon counting mode, the smearing effects of jitter and imaging are removed, yielding a time resolution of 280 fs.

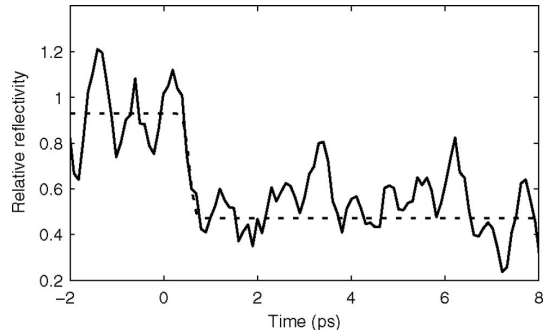


Fig. 2. Time-resolved drop in x-ray diffraction induced by nonthermal melting of InSb. The dashed line shows the fitted error function.

quadratic deconvolution yielded the time resolution of the streak camera to be 480 fs.

Laser excitation of bismuth (Bi) leads to the excitation of optical phonons [14]. The (111) reflection in Bi is very close to being forbidden. Excitation of the A_{1g} phonon mode induces a drop in the x-ray reflectivity followed by an oscillation. The period of the oscillation depends on temperature and excitation strength and is 340 fs for weak excitation [15] and 467 fs for stronger excitation [14]. A symmetric thin-film Bi sample was illuminated by laser pulses with a fluence of 4 mJ/cm^2 at an incidence angle of 45° . The phonons were probed by x rays with a photon energy of 3.2 keV. Figure 3 shows the drop in x-ray reflectivity associated with the excitation of the optical phonons. The accumulation time was 40 min. Fitting an error function yields an upper bound for the time resolution of 660 fs, which is large compared to the expected 170 fs fall time.

When a superlattice of SrTiO_3 (STO) and SrRuO_3 (SRO) is excited by a short laser pulse, large-amplitude coherent acoustic superlattice phonons can be generated. For an excited superlattice consisting of ten bilayers of 17.9 nm of STO and 6.3 nm of SRO, the (00116) reflection shows a strong oscillating reduction of the reflectivity, with a period of 3 ps [16]. The sample was excited at a fluence of 30 mJ/cm^2 , and the phonons were probed by x rays with a photon energy of 5.8 keV, and a bandwidth of 2×10^{-4} . Directly after excitation the reflectivity drops, followed by a damped oscillation, as shown in Fig. 4. This oscillation was compared to measurements done using a laser

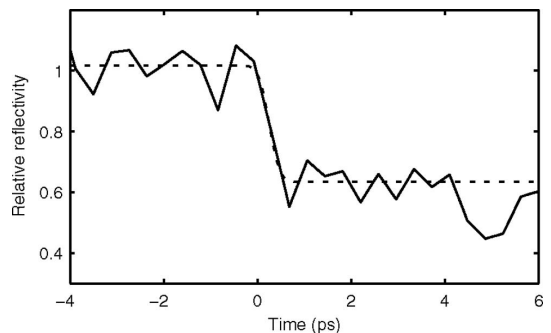


Fig. 3. Time-resolved diffraction of bismuth following laser excitation. The fitted error function is shown as a dashed line.

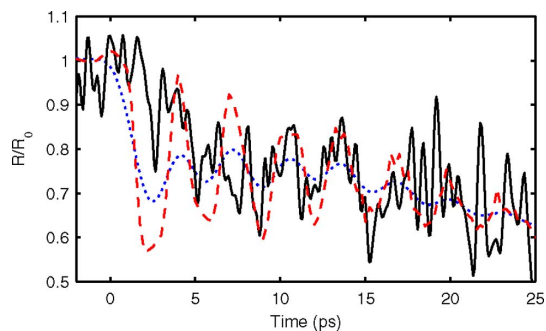


Fig. 4. (Color online) Oscillations in the x-ray reflectivity of the $\text{SrTiO}_3/\text{SrRuO}_3$ superlattice as recorded by the streak camera (solid curve) and from [16] (dashed curve). The dotted curve shows data from [16] filtered to simulate a time resolution of 2 ps.

plasma x-ray source at a time resolution of ~ 200 fs [17]. The comparison shows that the amplitude of the oscillation is unaffected by the temporal resolution of the streak camera. This is consistent with a resolution in the 400–600 fs range, as found in the studies of nonthermal melting and optical phonons in Bi. For a temporal resolution lower than 2 ps, the oscillation amplitude of the convoluted data is reduced, as illustrated in Fig. 4.

In conclusion, we have developed a hard x-ray streak camera capable of achieving subpicosecond resolution using single-photon counting. The performance has been demonstrated by reproducing three well-characterized experiments. The temporal spread due to jitter is removed by using a UV reference, and the single-photon counting compensates for smearing due to imperfect imaging and energy spread of the photoelectrons.

Streak cameras with subpicosecond time resolution will have a significant impact on the field of time-resolved science at synchrotron radiation facilities. They will also play a role at x-ray free-electron lasers. When lasers are synchronized to the accelerator it is essential to have a user-controlled diagnostic to track the delay between laser and x rays. By using a streak camera this can be measured directly at the position of the sample.

The authors thank the Swedish Research Council (VR), the Knut and Alice Wallenberg Foundation, the Crafoord Foundation, and the Carl Trygger Foundation for financial support. We also acknowledge the support of the European Commission via the Marie-Curie Program and the IRUVX-PP project.

References

1. D. Reis, K. Gaffney, G. Gilmer, and B. Torralva, *Mat. Res. Bull.* **31**, 601 (2006).
2. J. Feng, H. J. Shin, J. R. Nasiatka, W. Wan, A. T. Young, G. Huang, A. Comin, J. Byrd, and H. A. Padmore, *Appl. Phys. Lett.* **91**, 134102 (2007).
3. P. Gallant, P. Forget, F. Dorchie, Z. Jiang, J. C. Kieffer, P. A. Jaanimagi, J. C. Rebuffie, C. Goulmy, J. F. Pelletier, and M. Sutton, *Rev. Sci. Instrum.* **71**, 3627 (2000).
4. M. M. Shakya and Z. Chang, *Appl. Phys. Lett.* **87**, 041103 (2005).
5. D. Bradley, A. Roddie, W. Sibbett, M. Key, M. Lamb, C. Lewis, and P. Sachsenmaier, *Opt. Commun.* **15**, 231 (1975).
6. G. Huang, J. Byrd, J. Feng, H. A. Padmore, J. Qiang, and W. Wan, in *Proceedings of EPAC 2006, Edinburgh, Scotland* (2006), pp. 1250–1252.
7. M. Murnane, H. Kapteyn, and R. Falcone, *Appl. Phys. Lett.* **56**, 1948 (1990).
8. J. Larsson, *Opt. Lett.* **26**, 295 (2001).
9. D. Lowney, P. Heimann, H. Padmore, E. Gullikson, A. MacPhee, and R. Falcone, *Rev. Sci. Instrum.* **75**, 3131 (2004).
10. C. Ortiz and C. Coleman, *J. Phys. Chem. C* **111**, 17442 (2007).
11. A. Rousse, C. Rischel, and J. Gauthier, *Rev. Modern Phys.* **73**, 17 (2001).
12. A. Lindenberg, J. Larsson, K. Sokolowski-Tinten, K. Gaffney, C. Blome, O. Synnergren, J. Sheppard, C. Coleman, A. MacPhee, D. Weinstein, D. Lowney, T. Allison, T. Matthews, R. Falcone, A. Cavalleri, D. Fritz, S. Lee, P. Bucksbaum, D. Reis, J. Rudati, P. Fuoss, C. Kao, D. Siddons, R. Pahl, J. Als-Nielsen, S. Duesterer, R. Ischebeck, H. Schlarb, H. Schulte-Schrepping, T. Tschentscher, J. Schneider, D. von der Linde, O. Hignette, F. Sette, H. Chapman, R. Lee, T. Hansen, S. Techert, J. Wark, M. Bergh, G. Hultdt, D. van der Spoel, N. Timneanu, J. Hajdu, R. Akre, E. Bong, P. Krejcik, J. Arthur, S. Brennan, K. Luening, and J. Hastings, *Science* **308**, 392 (2005).
13. A. Jurgilaitis, R. Nüske, H. Enquist, H. Navirian, P. Sondhaus, and J. Larsson, *Appl. Phys. A* **100**, 105 (2010).
14. K. Sokolowski-Tinten, C. Blome, J. Blurns, A. Cavalleri, C. Dietrich, A. Tarasevitch, I. Uschmann, E. Forster, M. Kammler, M. Horn-von Hoegen, and D. von der Linde, *Nature* **422**, 287 (2003).
15. M. Hase, K. Mizoguchi, H. Harima, S. Nakashima, M. Tani, K. Sakai, and M. Hangyo, *Appl. Phys. Lett.* **69**, 2474 (1996).
16. C. von Korff Schmising, M. Bargheer, M. Kiel, N. Zhavoronkov, M. Woerner, T. Elsaesser, I. Vrejoiu, D. Hesse, and M. Alexe, *Appl. Phys. B* **88**, 1 (2007).
17. C. von Korff Schmising, A. Harpoeth, N. Zhavoronkov, Z. Ansari, C. Aku-Leh, M. Woerner, T. Elsaesser, M. Bargheer, M. Schmidbauer, I. Vrejoiu, D. Hesse, and M. Alexe, *Phys. Rev. B* **78**, 060404 (2008).

Paper V

Picosecond time-resolved x-ray reflectivity of a laser-heated amorphous carbon thin film

R. Nüske,¹ A. Jurgilaitis,¹ S. Dastjani Farahani,³ M. Harb,¹ C. v. Korff Schmising,¹ H. Enquist,² J. Gaudin,³ M. Störmer,⁵ Laurent Guerin,⁴ Michael Wulff,⁴ and J. Larsson^{1*}

¹Department of Physics, Lund University, P.O. Box 118, 22100 Lund, Sweden

²MAX-lab, Lund University, P.O. Box 118, 221 00 Lund, Sweden

³European XFEL GmbH, Albert-Einstein-Ring 19, D-22761 Hamburg, Germany

⁴European Synchrotron Radiation Facility, 6 rue Jules Horowitz, BP220, F-38043, Grenoble CEDEX, France

⁵Helmholtz-Zentrum Geesthacht, Zentrum für Material- und Küstenforschung GmbH, Max-Planck-Straße 1, 21502 Geesthacht

We demonstrate thin film x-ray reflectivity measurements with picosecond time resolution. Amorphous carbon films with a thickness of 46 nm were excited with laser pulses characterized by 100 fs duration, a wavelength of 800 nm and a fluence of 70 mJ/cm². The laser-induced stress caused a rapid expansion of the thin film followed by a relaxation of the films thickness as the heat diffused into the silicon substrate. We were able to measure changes in film thickness as small as 0.2 nm. The relaxation dynamics is consistent with a model accounting for carrier-enhanced substrate heat diffusivity.

PACS numbers: 46.80.+j, 62.20.-x, 62.25.-g, 62.25.Fg, 62.30.+d, 62.40.+i, 62.20.de, 65.40.-b, 66.10.cd, 68.35.Ct, 68.35.Ja
Keywords: x-ray reflectivity, x-ray reflectometry, time-resolved, thin film, amorphous carbon, diamond-like carbon

X-ray reflectivity is an established technique for the characterization of the structure of thin films and multilayers¹. Layer thicknesses, densities and surface roughness can be inferred from measured x-ray reflectivity curves. The layer morphology is a crucial parameter for the performance of thin film based devices. Until now, time-resolved x-ray reflectivity studies have focused on slowly varying states with a time-resolution from minutes to milliseconds^{2, 3, 4}. We have extended the technique to the ultrafast domain by recording the x-ray reflectivity of an amorphous carbon thin film with picosecond time-resolution using the pump-probe scheme in repetitive mode. In the present experiment we have used 46 nm thick amorphous carbon films coated on a silicon wafer. These are test substrates for the X-ray mirrors at the European X-FEL. Structural changes and thermal expansion of the thin films on this timescale are of importance for the beam quality of the X-ray FEL radiation, and more generally for other thin-film based coatings for use in the optical range.

The experiment was performed at beamline ID09B located at the ESRF. This beamline is dedicated to time-resolved x-ray diffraction and scattering techniques⁵. A high speed chopper system isolated single x-ray pulses at a rate of 986.3 Hz. A titanium:sapphire-based laser system provided excitation pulses with 100 fs duration at 800 nm center wavelength with up to 2 mJ pulse energy. The laser was synchronized to the x-ray source with a jitter of approximately 100 ps when the present experiment was performed. The x-ray pulse duration in 16-bunch mode was about 100 ps, which together with the timing jitter set the limit for the time-resolution in this experiment. The sample was a 46 nm thin film of amorphous sp³ rich carbon on a single-crystal silicon substrate⁶. The amorphous carbon film had 20% sp³ bonds. The laser was focused under normal incidence on the sample to a spot size of 0.2×8.2mm², where the elongated direction was parallel to the x-ray propagation direction. The induced time-resolution limit due to the crossed-beam geometry was about 30 ps, which was well below the x-ray pulse duration. The laser fluence was set to 70 mJ/cm². The damage

threshold of the amorphous carbon film was found to be 100 mJ/cm^2 , which is similar to what has been reported previously for amorphous carbon^{7, 8}. At this fluence we found no significant graphitization, which would have manifested itself as a permanent change in density and film thickness up to 20%^{9, 10}. In our measurement, the permanent density change was less than 0.1 %. Thus, the measurements could be performed below the damage threshold, in repetitive mode. The critical angle for total external reflection for the used x-ray energy of 18 keV is 0.092° . In order to match the laser and x-ray footprints on the sample when the x-rays were incident at angles near the critical angle, the x-ray focus size was set to $0.18 \times 0.02 \text{ mm}^2$ (horizontal \times vertical) by closing the vertical x-ray sample slits. The incident x-ray flux was $2.4 \cdot 10^9$ photons/s. X-ray reflectivity measurements were performed by scanning the x-ray incidence angle and the delay between x-ray and laser pulses, while the x-ray energy was kept constant. The specular reflected x-ray signal was recorded using a calibrated x-ray photodiode.

Knowledge about the film can be extracted from x-ray reflectivity measurements. The period of the fringes is determined by the film thickness. The fringe contrast depends on the density of film and substrate. As the roughness increase, a drop of intensity for high-q values is observed. In our experiment the changes of film parameters were subtle and not evident obvious from visual inspection of plots like the ones in Fig.1. However the parameters could be extracted with high accuracy using a fitting procedure from the raw data. The specular x-ray reflectivity for a thin film system can be calculated using the matrix based method described by Gibaud et al. in Ref. 1. Using nonlinear regression, the films average thickness, density and root-mean-square (rms) surface roughness could be extracted for each delay. The time-dependence of these parameters is displayed in Fig 2. The films thickness and density have been chosen as independent parameters in the fitting process. We find that the product of

the thickness and density of the film is approximately constant for all delays. This shows that the laser excited the film below the threshold for permanent damage. Following excitation, the film expands rapidly by 0.3% accompanied by a corresponding decrease in density. From the measurement, we can set an upper limit for the timescale of this expansion process of 200 ps, which was the temporal resolution at the beamline during the experiment. Subsequently, the film thickness and density relax within 2 ns. We also observe an increase of surface roughness of the film from 0.1 nm to 0.4 nm after laser excitation. The surface roughness is given as the root mean square. The surface roughness of the thin film does not recover within the observed time frame of 10 ns. We interpret the results as follows. After absorption of the pulsed laser radiation, the carrier and lattice temperature equalize within a few picoseconds in the thin film and in the substrate. The interface between film and substrate acts as a barrier for carriers generated in the thin film, similar to what has been reported by Cavalleri et al.¹¹. According to Thomsen et al.¹², the initial temperature increase $\Delta T(z)$ following laser excitation in the film is given by:

$$\Delta T(z) = (1 - R) \frac{F}{C\xi} e^{-z/\xi} \quad (1)$$

where F is the laser fluence (energy per unit area), C is the heat capacity, ξ is the attenuation length, z is the distance from the surface, and R is the reflectivity of the surface at the boundary between air and amorphous carbon. The reflectivity at the boundary between amorphous carbon and Si is below 4 % and has been neglected in our simulations. Since the thickness of the film is smaller than the 200 nm laser absorption depth (800 nm)⁹, the excitation of the underlying substrate is substantial. We calculate the initial temperature distribution using Eq. (1). The initial temperature rise at the amorphous carbon top surface is calculated to be 1400 K, leaving the film well below the melting point, which is above

3000 K. The initial increase of the temperature of silicon at the interface is 150 K. The

$$\rho C \frac{\partial T}{\partial t} = \frac{\partial}{\partial z} k \frac{\partial T}{\partial z} \quad (2)$$

$$\frac{\partial^2 u}{\partial t^2} = \frac{\partial \sigma}{\partial z} \quad (3)$$

$$\sigma = 3 \frac{1 - \nu}{1 + \nu} B \varepsilon - 3 B \beta (T - T_0) \quad (4)$$

generated temperature profile in the thin film and substrate produces thermal stress, which is released as a strain wave starting at the sample surface and at the interface between Si and amorphous carbon. Since the speed of sound in amorphous carbon is about 10 km/s¹³, the timescale of this expansion process is estimated to be about 5 ps. This timescale is significantly faster than the 200 ps temporal resolution, meaning that the waves have propagated out of the probed depth and the observed expansion is governed by temperature. Finally, the film thickness decreases due to heat diffusion into the substrate. The timescale of this process is determined by the heat conductivity and capacity of both the film and the substrate.

Below, a model to simulate the temporal evolution of the film thickness and density following laser excitation is described. Since the excitation depth ξ is negligible compared to its lateral size, the problem can be considered quasi one-dimensional. The initial stress and following expansion will only be z dependent. The system is determined by the heat equation and the elastic equations:

In equations (2)-(4), T denotes the temperature, σ the stress, u the displacement, and $\varepsilon = \partial u / \partial z$ denotes the strain. The parameter k is the heat conductivity, ρ the density, B the bulk modulus, ν is Poisson's ratio, and β is the linear expansion coefficient of the medium. The calculated initial temperature profile $T(z, t=0)$ sets the initial condition for the simulation.

The displacement $u(z, t)$ and temperature $T(z, t)$ values are calculated numerically from Eqs. (2-4) using the finite-element method (FEM). The model system is a 46.3 nm thin amorphous carbon film on a bulk silicon substrate. The calculated time-dependent film thickness and density are plotted together with experimental values in Fig. 2. The dashed line displays the simulation results assuming the material parameters of silicon and amorphous carbon under equilibrium condition as reported in literature^{9, 14-18}. From this simulation, a time constant of about 3 ns is predicted for the film thickness and density relaxation. Experimentally, the thin film relaxation process is found to be about a factor 2 faster. We assign this discrepancy to the increase of ambipolar thermal diffusivity for high carrier densities in the silicon substrate as reported by Young et al.¹⁹. The authors calculate an increase of thermal diffusivity above a carrier density of 10^{19} cm^{-3} . The photo-induced carrier density in the silicon substrate is estimated to be $7 \cdot 10^{20} \text{ cm}^{-3}$. We find, that a five-fold or higher increase in the substrate thermal diffusivity can reproduce the thin-film relaxation dynamics more accurately. This is in good agreement with Ref. 19. The dynamics of the thin film thickness when the increase in thermal diffusivity has been included is displayed in Fig 2 (solid line).

The relaxation process of the surface roughness shows a substantially different behavior. We observe a rapid increase of roughness following laser excitation, which does not relax within 10 ns. The surface roughness is sensitive to lateral excitation inhomogeneity of both film and substrate. The total expansion of the substrate is estimated to be about 4 nm at a delay of 600 ps. This is much more than the increase in film thickness. A 10 % variation in the lateral laser beam intensity is sufficient to induce the observed 0.4 nm roughness. The variation could be due to a non-uniform laser beam profile, or fringes arising from interference between the incident and reflected laser light fields^{20,21}. The heat conduction process within the substrate is slow compared to the film due to much smaller temperature gradients. This

explains the observed slow roughness relaxation. From the experimental data, we can set a lower limit of 10 ns required for the thin film roughness to recover under the used excitation conditions.

In conclusion, we have shown that x-ray reflectivity measurements of thin films can be performed with picosecond resolution. Thermal stress generated by laser excitation causes the film to rapidly expand and increases the surface roughness substantially. The subsequent relaxation of the films thickness is determined by heat diffusion into the substrate. This process is accelerated by photo-induced carriers in the substrate.

Acknowledgments

The authors would like to thank the Swedish Research Council (VR), the Knut and Alice Wallenberg Foundation, the Crafoord Foundation and the Carl Trygger Foundation for financial support. M. H. acknowledges financial support from the Natural Sciences and Engineering Research Council of Canada.

References

- ¹ A. Gibaud and S. Hazra, *Curr. Sci.* 78, 1467 (2000).
- ² M. Gonzalez-Silveira, J. Rodriguez-Viejo, M. T. Clavaguera-Mora, T. Bigault, and J. L. Labar, *Phys. Rev. B* 75, 075419 (2007).
- ³ A. G. Richter, M. K. Durbin, C. J. Yu, and L. Dutta, *Langmuir* 14, 5980 (1998).
- ⁴ T. Matsushita, E. Arakawa, Y. Niwa, Y. Inada, T. Hatano, T. Harada, Y. Higashi, K. Hirano, K. Sakurai, M. Ishii, et al., *Eur. Phys. J.-Spec. Top.* 167, 113 (2009).
- ⁵ M. Wulff, F. Schotte, G. Naylor, D. Bourgeois, K. Moffat, and G. Mourou, *Nucl. Instrum. Methods Phys. Res. Sect. A-Accel. Spectrom. Dect. Assoc. Equip.* 398, 69 (1997).

- ⁶ M. Störmer, C. Horstmann, F. Siewert, F. Scholze, M- Krumrey, F. Hertlein, M- Matiaske, J. Wiesmann, and J. Gaudin, Single-layer mirrors for advanced research light sources Single-layer mirrors for advanced research light sources, AIP Conf. Proc. 1234, 756 (2010)
- ⁷ R. Koter and M. Weise and A. Hertwig and U. Beck and J. Kruger, J. Optoelectron. Adv. Mater., 12, 663 (2010)
- ⁸ T. V. Kononenko, S. M.Pimenov, V. V. Kononenko, E. V. Zavedeev, V. I. Konov, G. Dumitru, V. Romano, Appl. Phys. A 79, 543 (2004).
- ⁹ J. Robertson, Mater. Sci. Eng. R-Rep. 37, 129 (2002).
- ¹⁰ A. C. Ferrari, B. Kleinsorge, N. A. Morrison, A. Hart, V. Stolojan, J. Robertson, J. Appl. Phys., 85, 7191 (1999)
- ¹¹ A. Cavalleri, C. W. Siders, F. L. H. Brown, D. M. Leitner, C. Toth, J. A. Squier, C. P. J. Barty, K. R. Wilson, K. Sokolowski-Tinten, M. H. von Hoegen, et al., Phys. Rev. Lett. 85, 586 (2000).
- ¹² C. Thomsen, H. T. Grahn, H. J. Maris, and J. Tauc, Phys. Rev. B 34, 4129 (1986).
- ¹³ A. J. Bullen, K. E. O'Hara, D. G. Cahill, O. Monteiro, and A. von Keudell, J. Appl. Phys. 88, 6317 (2000).
- ¹⁴ R. F. Wood and G. E. Giles, Phys. Rev. B 23, 2923 (1981).
- ¹⁵ A. Champi, R. G. Lacerda, G. A. Viana, and F. C. Marques, J. Non-Cryst. Solids 338, 499 (2004).
- ¹⁶ M. Hakovirta, J. E.Vuorinen, X. M. He, M. Nastasi, and R. B. Schwarz, Appl. Phys. Lett. 77, 2340 (2000).
- ¹⁷ S. Cho, I. Chasiotis, T. A. Friedmann, and J. P. Sullivan, J. Micromech. Microeng. 15, 728 (2005).
- ¹⁸ M. Shamsa, W. L. Liu, A. A. Balandin, C. Casiraghi, W. I. Milne, and A. C. Ferrari,

Appl. Phys. Lett. 89, 161921 (2006).

¹⁹ J. F. Young and H. M. van Driel, Phys. Rev. B 26, 2147 (1982).

²⁰ P. M. Fauchet and A. E. Siegman, Appl. Phys. Lett. 40, 824 (1982)

²¹ J. F. Young, J. S. Preston, H. M. Van Driel, and J. E. Sipe, Phys. Rev. B 27, 1424 (1983)

Figure Captions

FIG. 1: X-ray reflectivity of an amorphous carbon thin film as a function of incidence angle and delays between laser excitation and x-ray probe (curves are offset for clarity). The solid lines are fits using the thin film reflectivity model.

FIG. 2: Time-evolution of the amorphous carbon thin film thickness(a), density(b), and surface roughness(c) following laser excitation. Theoretically calculated dynamics using a thermo-elastic model: for equilibrium heat conductivity (dashed line) and modified heat conductivity (solid line), see text. The dotted line is a guide for the eye.

Figures

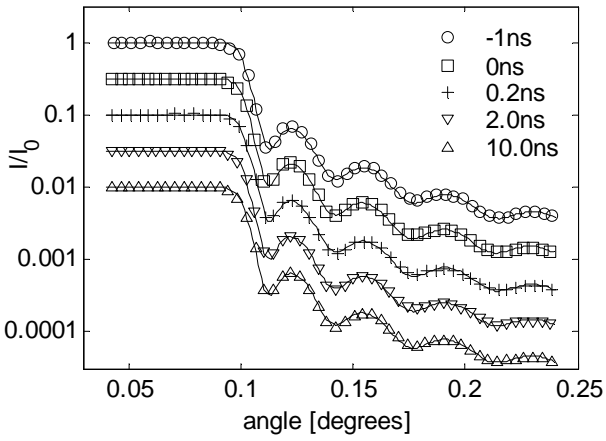


Fig 1.

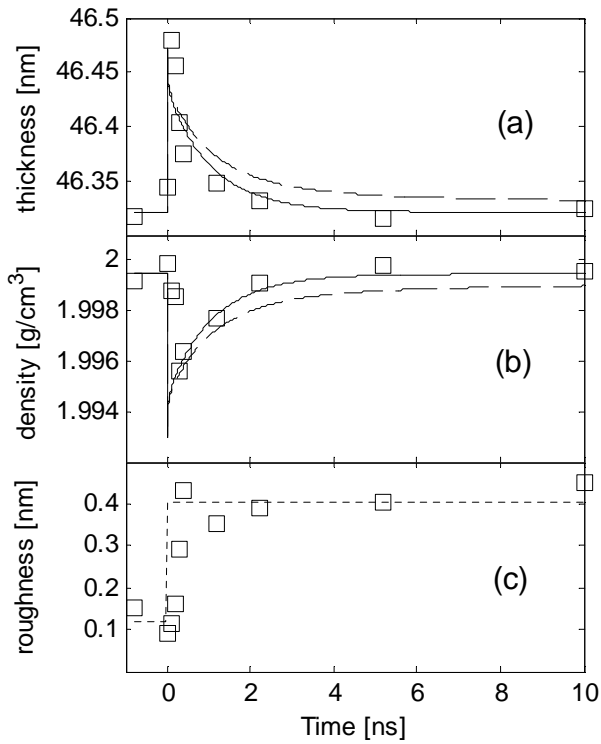


Fig. 2

Paper VI

Formation of nanoscale diamond by femtosecond laser-driven shock

R. Nüske¹, A. Jurgilaitis¹, H. Enquist¹, Maher Harb¹, Yurui Fang^{2,3}, Ulf Håkanson², J. Larsson^{1*}

¹Atomic Physics Division, Department of Physics, Lund University, P.O. Box 118, SE-221 00 Lund, Sweden

²Division of Solid State Physics/The Nanometer Structure Consortium at Lund University (nmC@LU), P.O. Box 118, S-221 00 Lund, Sweden

³Beijing National Laboratory for Condensed Matter Physics, Institute of Physics, Chinese Academy of Sciences, P.O. Box 603-146, 100190 Beijing, China

* Corresponding author: jorgen.larsson@fysik.lth.se

Abstract

Formation of cubic diamond from graphite following irradiation by a single, intense, ultra-short laser pulse has been studied. Highly oriented pyrolytic graphite (HOPG) samples were irradiated by 100 fs pulses at a wavelength of 800 nm. Following laser exposure, the highly oriented pyrolytic graphite samples have been studied using Raman spectroscopy of the sample surface. In the laser-irradiated areas, nanoscale cubic diamond crystals have been formed. We have also studied the exposed areas using grazing incidence powder diffraction. We observed a restacking of planes from hexagonal graphite to rhombohedral graphite. The intensity of the rhombohedral graphite powder peaks get more pronounced as the fluence is increased due to restacking at larger depths.

Introduction

The types of bonds in Carbon materials range from the extremely strong sp^3 -type bonds in diamond, to weak van der Waals bonds in graphite. As a result of many types of bonds a large variety of natural and manmade allotropes of carbon exist. Finding controlled pathways between these allotropes and

in particular to be able to transform graphite to diamond has been a subject that has fascinated scientists and engineers for a century. The first report of manmade diamonds was reported by Bundy et al. in 1955 [A1]. They synthesized diamond by subjecting graphite to high temperature and pressure. Today CVD grown diamonds rival the quality of natural diamonds, but the topic of transforming the material is intriguing. There are also emerging technical applications for nanodiamonds which recently were reviewed by Baidakova and Vul' [A2]. The wide range of applications has triggered many methods for syntheses. These methods include high-pressure, high temperature transformation during detonation of carbon-based explosives [A3], charged particle beam bombardment of graphite onions or graphite [A4, A5] and pulsed-laser induced interfacial reaction (PLIIR) in liquids. Yang et al have reported on synthesis of nano-diamond particles consisting of both hexagonal and cubic diamond from hexagonal graphite using a pulsed-laser induced interfacial reaction (PLIIR)[A6] with rhombohedral graphite as an intermediate. [A6]. So far, electron and ion bombardment of graphite [A4, A5] has proven to give an unprecedented control of size and position of the nanodiamonds, making it possible to write patterns on a surface

The interaction of short-laser pulses with graphite has over the last decade been studied in order understand a range of processes [A7] including laser ablation of graphite in order to isolate graphene [A8, A9]. It has also been suggested that hexagonal diamond can be created by laser-irradiation of highly oriented pyrolythic graphite [A10]. Hexagonal diamond has been predicted to be even harder than cubic diamond [A11] and methods to directly synthesize it would be of great importance. Work related to direct light-actuated transformation of graphite to diamond on the surface has been carried out by Raman et al who have reported on transient sp³ bonded structures in laser excited graphite [A12] and Kanasaki et al. who observed sp³ bonded structures on graphite with transmission electron microscopy following exposure by approximately 10⁴ pulses [A13].

In the present experiment, we have irradiated the sample with short laser pulses and created structures on the surface which contains nanodiamonds thereby opening a path to making diamond patterns on graphite with μm precision. We observe laser-driven restacking of hexagonal graphite to

rhombohedral graphite and the formation of cubic diamond nanocrystals. We observe the restacking with X-ray diffraction and the diamond formation with Raman spectroscopy.

Experimental methods

An HOPG sample (12× mm * 12× mm * 2 mm, ZYA grade with mosaic spread of 0.4°) was used in this study. It was irradiated by single laser pulses. The laser was a titanium-sapphire laser with wavelength centered around 800 nm. The duration of the laser pulses was 100 fs. The laser radiation was focused to a peak intensity of up to 2.1×10^{15} W/cm². The fluence range 80-210 J/cm² was investigated. After laser irradiation, the crystal structure was analyzed using grazing incidence x-ray powder diffraction performed at beamline D611 at the MAX-laboratory synchrotron radiation facility in Lund. The X-ray spot size on the sample was 0.2*2.5 mm² at the incidence angle of 0.8° used in the experiment. This footprint is comparable to the spatial extent of the array of single laser –pulse irradiated spots which has a size of 0.15*3.0 mm². Each individual laser spot size was 0.15*0.15 mm². The separation between the laser spots was 0.25 mm. The laser spot-size was measured by a knife-edge scan whereas the X-ray spot was measured using a phosphor and a CCD camera. The photon energy of the X-rays was 9 keV and the bandwidth $\Delta E/E=0.1\%$. X-rays incident on a phosphor screen were imaged onto a CCD camera. The images were recorded and analyzed in order to produce the powder patterns. The set-up was calibrated with silicon powder. The set-up allowed for coverage of a q-range from (2.9-4.4 Å⁻¹) with a q-resolution of (0.02 Å⁻¹). The samples were also inspected by optical microscopes, a scanning electron microscope (SEM), and using Raman spectroscopy. A fiber-coupled Raman microscope system was used to study the phonon characteristics of the irradiated samples. The system is equipped with an imaging CCD and a motorized stage allowing for simple identification of the laser-irradiated spots. Raman spectra were obtained in a backscattering configuration using a 100x objective (NA 0.8) and a 632.8 nm HeNe laser (~2 mW at the sample). For system details see Chen et al. [A14]. It provides a spatial resolution of 1 μm and a probing depth of about 100 nm.

Results-Raman spectroscopy

Raman spectroscopy was used to investigate the sample surface. This method provides high spatial resolution and surface sensitivity. The Raman spectra from both pristine and laser-irradiated HOPG are shown in Figure 1. Within the laser-exposed area, the measured Raman spectra vary locally. This is shown in Figure 1 with two typical spectra from different spots within area exposed to a single laser pulse with a incident fluence of 90 mJ/cm^2 . The most striking difference is the peak at 1332 cm^{-1} , which is the characteristic Raman peak for the T_{2g} phonon mode in cubic diamond [A15]. This clearly shows formation of nanodiamonds in the laser-exposed area. The feature at 1580 cm^{-1} can be identified as the E_{2g} mode of graphite and is present in all spectra [A16]. In laser irradiated areas we find a broad feature at 1360 cm^{-1} , which originates from the graphite A_{1g} mode. This mode becomes Raman active due to laser-induced disorder in the graphite structure [A17, A18]. The linewidth of the measured diamond peak is 20 cm^{-1} . Yoshikawa et al. reported on the effect of crystal size on the linewidth of Raman spectra of cubic diamond [A19]. According to this model, which accounts for homogeneous broadening of the Raman line due to phonon confinement and damping, the cubic diamond crystals found in our experiment are at least 8 nm in size. Other broadening mechanisms such as strain induced by the rapid quenching may be present. Hence, the crystal may in fact be larger than 8 nm. The area, over which the diamond peak is visible in the spectra, is several micrometers in size which is an upper limit of the size of the diamond.

Results-Grazing incidence X-ray diffraction

The result of the Raman measurement was in disagreement with a recent powder diffraction study by Sano et al. The authors claimed that they could see a powder diffraction pattern from hexagonal diamond but no powder peaks from cubic diamond was seen [A10]. In order to resolve the disagreement we investigated our samples using X-ray powder diffraction. The result can be seen in Figure 2 where we show powder diffraction data from laser-exposed areas as well as from areas with pristine HOPG. As can be seen, all peaks can be identified as reflections from either hexagonal or

rhombohedral graphite. The rhombohedral modification of graphite can be found only after the laser irradiation. The structure of rhombohedral graphite (ABCABC) can be understood as an extended stacking fault of the hexagonal configuration (ABAB), and is known to be generated when hexagonal graphite is deformed mechanically [A20]. In Figure 3, we show the relative amplitude of the rhombohedral graphite as function of fluence. What is clear is that a single laser pulse can restack the graphite and the higher the fluence the larger volume fraction of the restacked material is obtained. No reflections from hexagonal diamond are present in the powder diffraction data. Since the result was different from that reported by Sano et al [A10], we reinvestigated their data. The authors showed x-ray powder diffraction data covering a q -range range of 2.8 \AA^{-1} to 3.6 \AA^{-1} with a resolution of 0.03 \AA^{-1} . Table 1 summarizes results obtained from their diffraction data, values for hexagonal and cubic diamond [A21], and hexagonal and rhombohedral graphite [A20][A22] and the results from this study. The reflection of the 100 plane of hexagonal diamond at 2.87 \AA is not present in their data. Furthermore, the peaks at 3.01 \AA and 3.20 \AA are better matched with reflections from rhombohedral graphite.

This comparison shows that the data presented in their work can be better explained with the hexagonal and rhombohedral modification of graphite. Based on the powder diffraction data, one may draw the conclusion that nano-diamonds are not created. However, one should note that due to the small total area covered with cubic diamonds in our work they are not expected to be seen in the powder-diffraction data. Similarly nano-diamonds created by PLIIR described by Wang and Yang [A6] were observed with electron diffraction whereas it was not possible to observe them with X-ray powder diffraction.

Possible mechanism for diamond formation

There are different potential mechanisms for the diamond formation. The first is similar to the mechanism in a shock-wave experiment. Within a few picoseconds after laser excitation, the temperature will rise to the melting temperature. When the topmost layer is molten, the graphite will start to expand towards the density of liquid carbon. As this occurs, a pressure is formed at the

boundary between the solid and liquid material. This launches a strain wave into the material. Experiments investigating such waves generated by ultrafast melting have been carried out in Si [A23] and InSb [A24]. As the density of liquid carbon which is 1.6 g/cm^3 [A25] differs significantly from that of graphite (2.26 g/cm^3), the shock wave amplitude is large. The amplitude can be calculated by solving the elastic equations, similar to Thomsen et al [A25], if the density, compressibility and speed of sound are known for the solid and liquid. The compressibility of liquid carbon is 150 GPa [A25]. The density mismatch between the solid and liquid corresponds to a strain of 38% in the liquid. The stress at the solid liquid boundary is then $150 \text{ GPa} / 2 * 0.38 (1 - 0.46)$, where the 46% reflectivity of the stress wave has been taken into account and the factor of 2 originates from the fact that two counter-propagating waves are created. The sum of the static strain and the two counter propagating waves must be zero at the time of generation to fulfill the initial condition of zero strain. A boundary condition is that the stress must be equal on the two sides of the solid-liquid boundary [A24]. Thus, the amplitude of the stress wave in graphite is 15 GPa and due to laser heating, the temperature will be close to the melting temperature of graphite. Under traditional shock experiments the transformation has been shown to be martensitic below 2000 K and hexagonal diamond is created. Cubic diamond which has been found experimentally is believed to be created from hexagonal diamond. At temperatures above 4000 K only cubic carbon is formed [A27]. It should be noted that in our study, the high pressure would last only for 5-10 ps.

In the study by Kanasaki et al [A13], the formation of sp^3 bonds at the surface of the HOPG sample was induced using much lower laser fluence. The mechanism in this case cannot be pressure driven. The authors speculate on a restacking to AAA graphite followed by buckling of planes and formation of sp^3 bonds. Such restacking has been predicted by tight binding molecular dynamics (TBMD) calculations [A28]. Their work did not show any diamond formation.

A third possibility, which cannot be ruled out, is that diamonds are formed during rapid quenching [A29].

Conclusion

In conclusion, we find that intense, short laser pulses can transform graphite to nanoscale cubic diamond. We find that the surrounding material to a large extent has restacked from hexagonal graphite to rhombohedral graphite. The restacking has in PLIR experiments been shown to coincide with the transformation from graphite to diamond [A6]. There is no indication of hexagonal diamond which would manifest itself as a Raman peak between 1319 cm^{-1} and 1326 cm^{-1} [A31] and in the powder diffraction pattern. This indicates a pathway from hexagonal graphite via an intermediate restacked graphite phase to cubic diamond.

Acknowledgements

The authors would like to thank the Swedish Research Council (VR), the Knut and Alice Wallenberg Foundation, the Crafoord Foundation and the Carl Trygger Foundation for financial support. M. H. acknowledges financial support from the Natural Sciences and Engineering Research Council of Canada.

References

- A1 F.P. BUNDY, H.T. HALL, H.M. STRONG, *NATURE* 176, 51 (1955)
- A2 M. BAIDAKOVA AND A. VUL', *J. PHYS. D: APPL. PHYS.* 40, 6300 (2007)
- A3 M. Van Thiel, F.H. Ree, *J. Appl. Phys.* 62, 1761 (1987)
- A4 F. BANHART, P. M. AJAYAN, *NATURE* 382, 433 (1996)
- A5 A. DUNLOP, G. JASKIEROWICZ, P. M. OSSI, S. DELLA-NEGRA, *PHYS.REV. B* 76, 155403 (2007)
- A6 G.W. YANG, J.B.WANG, *APPL. PHYS. A* 72, 475 (2001)
- A7 M.D. SHIRK AND P.A. MOLIAN, *CARBON* 39, 1183 (2001)
- A8 M. LENNER, A. KAPLAN, R. E. PALMER, *APPL. PHYS. LETT.* 90, 153119 (2007)

- A9 M. LENNER, A. KAPLAN, CH. HUCHON, R. E. PALMER, *PHYS. REV. B* 79, 184105 (2009)
- A10 T. SANO, K. TAKAHASHI, O. SAKATA, M. OKOSHI, N. INOUE, K. F. KOBAYASHI, A. HIROSE, *J. PHYS. CONF. SER.* 165, 012019 (2009)
- A11 ZICHENG PAN, HONG SUN, YI ZHANG, AND CHANGFENG CHEN, *PHYS. REV. LETT.* 102, 055503 (2009)
- A12 R. K. RAMAN, Y. MUROOKA, C.-Y. RUAN, T YANG, S. BERBER, D. TOMÁNEK. *PHYS. REV.LETT.* 101, 077401 (2008)
- A13 J. KANASAKI, E. INAMI, K. TANIMURA, H. OHNISHI, K. NASU, *PHYS. REV. LETT.* 102, 087402 (2009)
- A14 J. CHEN, G. CONACHE, M. PISTOL, S. GRAY, M. T. BORGSTRÖM, H. XU, H.Q. XU, L. SAMUELSON, U. HÅKANSON, *NANO LETT.* 10, 1280 (2010)
- A15 A. C. FERRARI, J. ROBERTSON, *PHYS. REV. B* 61, 14095 (2000)
- A16 Y. WANG, D. C. ALSMEYER, R. L. MCCREERY, *CHEM. MAT.* 2, 557 (1990)
- A17 T. C. CHIEU, M. S. DRESSELHAUS, M. ENDO, *PHYS. REV. B* 26, 5867 (1982)
- A18 F. TUINSTRA, J. L. KOENIG, *J. CHEM. PHYS.* 53, 1126 (1970)
- A19 M. YOSHIKAWA, Y. MORI, M. MAEGAWA, G. KATAGIRI, H. ISHIDA, A. ISHITANI, *APPL. PHYS. LETT.* 62, 3114 (1993)
- A20 G. E. BACON, *ACTA. CRYSTALLOGR.* 3, 320 (1950)
- A21 F. P. BUNDY, J. S. KASPER, *J. CHEM. PHYS.* 46, 3437 (1967)
- A22 H. LIPSON, A. R. STOKES, *PROC. R. SOC. LOND. A-MATH. PHYS. SCI.* 181, 0101 (1942)
- A23 K. SOKOLOWSKI-TINTEN, C. BLOME, C. DIETRICH, A. TARASEVITCH, A. CAVALLERI, J. SQUIER, M. KAMMLER, M. HORN VON HOEGEN, D. VON DER LINDE, *PHYS. REV. LETT.* 87, 225701(2001)

A24 H. ENQUIST, H. NAVIRIAN, T. N. HANSEN, A. M. LINDENBERG, P. SONDDHAUSS, O. SYNNERGREN, J. S.

WARK, J. LARSSON, *PHYS. REV. LETT.* 98, 225502 (2007)

A25 J. STEINBECK, G. DRESSSELHAUS, M. S. DRESSSELHAUS, *INT. J. THERMOPHYS.* 11, 789 (1990)

A26 C. THOMSEN, H. T. GRAHN, H. J. MARIS, AND J. TAUC, *PHYS. REV. B* 34, 4129 (1986)

A27 D. J. ERSKINE, W. J. NELLIS, *NATURE* 349, 317 (1991)

A28 M. E. GARCIA, T. DUMITRICA, H. O. JESCHKE, *APPL. PHYS. A* 79, 855 (2004)

A29 A. Yu. Basharin, V. S. Dozhdikov, V. T. Dubinchuk, A. V. Kirillin, Y. Lysenko, *Tech. Phys. Lett.*

35, 428 (2009)

A30 D. S. Knight, W. B. White, *J. Mater. Res.* 4, 391 (1989)

Figure captions

Figure 1: Raman spectra of HOPG after femtosecond laser irradiation and pristine HOPG in comparison. Peak positions for graphite G- and D-peaks, and the diamond peak are marked as reference.

Figure 2: grazing incidence powder XRD pattern of single laser pulse irradiated HOPG. The laser peak intensity: 2.1×10^{15} W/cm², x-ray energy 9 keV, x-ray grazing angle: 0.2°. Δ, o : before and after laser exposure; hG: hexagonal graphite, rG: rhombohedral graphite, hD: hexagonal diamond, cD: cubic diamond .

Figure 3: integrated x-ray intensity of the rhombohedral graphite reflections 100 (squares), 110 (triangles), and 211 (circles) as function of excitation laser fluence.

Table captions

Table 1: Powder diffraction peak positions from this study, compared to results from [A10], hexagonal graphite, rhombohedral graphite [A20] [A22], hexagonal diamond [A21], and cubic diamond.

Figure 1

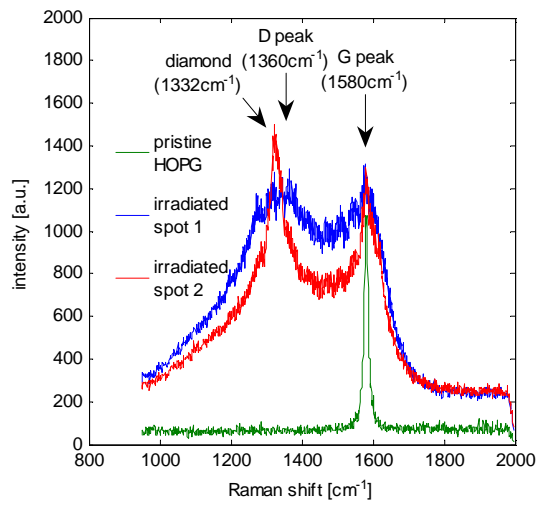


Figure 2

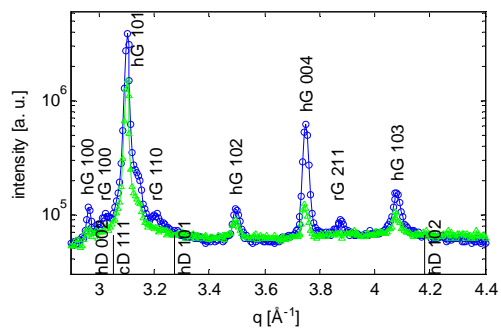


Figure 3.

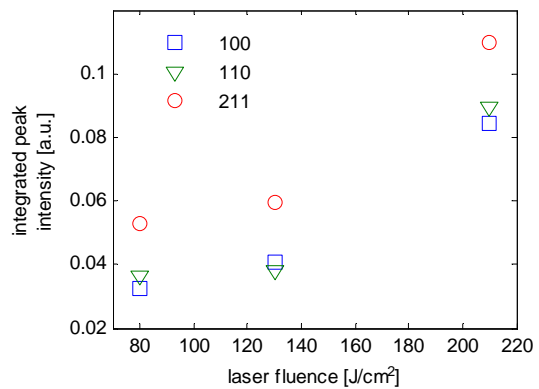


Table 1

this study q [\AA^{-1}]	Sano et al.[A10] q [\AA^{-1}]	hexagonal graphite [A22] q [\AA^{-1}]	hexagonal diamond [A21] q [\AA^{-1}]	rhombohedral graphite [A20] q [\AA^{-1}]	cubic diamond q [\AA^{-1}]
2.96	2.95	2.95	2.87		
3.02	3.01		3.05	3.02	3.05
3.10	3.09	3.10			
3.21	3.20		3.27	3.21	
3.49	3.50	3.50			
3.75		3.75		3.75	
3.88				3.87	
4.08		4.08			

Paper VII

Picosecond Dynamics of Laser-Induced Strains in Graphite

M. Harb¹, A. Jurgilaitis¹, H. Enquist², R. Nüske¹, C. v. Korff Schmising¹, J. Gaudin³,
S. L. Johnson⁴, C. J. Milne⁵, P. Beaud⁴, E. Vorobeva⁴, A. Caviezel⁴, S. Mariager⁴, G. Ingold⁴, and
J. Larsson^{1*}

¹*Atomic Physics Division, Department of Physics, Lund University, P.O. Box 118, 22100 Lund, Sweden*

²*MAX-lab, Lund University, P.O. Box 118, Lund, Sweden*

³*European XFEL GmbH, Albert-Einstein-Ring 19, D-22761 Hamburg, Germany*

⁴*Swiss Light Source, Paul Scherrer Institut, 5232 Villigen PSI, Switzerland*

⁵*Laboratoire de Spectroscopie Ultrarapide, Ecole Polytechnique Fédérale de Lausanne, 1015 Lausanne,
Switzerland*

Abstract

We report on the use of grazing-incidence time resolved x-ray diffraction to investigate the evolution of strain in natural graphite excited by femtosecond laser pulses in the fluence range of 6-35 mJ/cm². Strains corresponding to up to ~2.8% *c*-axis expansion were observed. We show that the experimental data is in good agreement with calculations based on the Thomsen strain model in conjunction with dynamical diffraction theory. Furthermore, we find no evidence of non-thermal lattice expansion as reported in recent ultrafast electron diffraction studies of laser-excited graphite conducted under comparable excitation conditions.

PACS numbers: 63.20.dd, 61.05.cp, 78.47.J-

Ever since the discovery of fullerenes there has been an explosive interest in the synthesis of carbon-based materials, placing these materials at the forefront of the nanoscience revolution.

Today, carbon-based materials are the basis for numerous novel technologies including graphene based nanoelectronics [1] and nanofluidics in carbon nanotubes [2]. At the most basic level, the existence of different carbon allotropes with rich and often exotic material properties owes to the variety of bonding types that a carbon atom can form. Graphite is characterized by the weak van der Waals bonding between the interlayer planes and the strong covalent sp^2 hybridized bonds in-plane. This bonding structure is responsible for the high anisotropy in the electronic, optical, and mechanical properties of graphite. The ability to modify the bonding configuration in graphite through irradiation by a laser pulse has been exploited to synthesize novel carbon structures such as nanodiamonds [3-4] and sp^3 -rich carbon nanofoams [5]. The ablation of intact layers of graphene off graphite has been also predicted [6] and demonstrated [7]. While a detailed understanding of the processes leading to the change in the bonding configuration in laser-excited graphite is still lacking, it is believed that three key mechanisms are involved: the abrupt change in the electronic configuration due to the excitation of the π electrons, the ensuing launch of large amplitude coherent optical phonons, and the thermal strains that develop at relatively later times. The strain wave dynamics studied in this paper are sensitive to the interlayer binding strength and should lead to an improved understanding of thermal stress and strain effects in graphite. Given the important role of strain in modulating the electronic properties of graphene [8], understating of stress and strain effects is essential to the successful application of graphene in the next generation of electronics. To further our understanding of strain wave dynamics and other laser-induced electron-phonon processes, one would like to gain a glimpse of the dynamics that follow optical excitation from an atomic perspective and on the relevant femtosecond to picosecond timescales. Capturing transient atomic structures with such unprecedented time resolution became recently possible due to advances in time resolved x-ray and electron diffraction techniques [9-16]. These techniques, with the ability to directly probe the structure of the

perturbed lattice, offer extraordinary insights into the complex and competing channels of relaxation that follow the interaction of laser with matter.

In a recent study by Carbone *et al.*, laser-excited graphite was investigated using ultrafast electron diffraction (UED) in reflection geometry [15]. Carbone and coworkers observed contraction of the graphite lattice along the *c*-axis at the onset of excitation, followed by expansion of up to 1.25% of the interlayer distance at the highest fluence of 44.5 mJ/cm². It was argued that such a large amount of lattice expansion cannot be accounted for by linear thermal expansion alone. Instead, the authors attributed the expansion to non-thermal mechanisms that include the anisotropic population of carriers in the electronic band and the subsequent generation of coherent optical phonons. The results reported by Carbone *et al.* started a debate within the scientific community on whether the observed shifts in the positions of the diffraction spots represent real structural dynamics or are somehow related to transient electric fields generated at the surface of the sample due to the ejection of electrons by the laser pulse. Park *et al.* investigated the effects of transient electric fields on an electron probe pulse both experimentally and through simulations, and concluded that these fields can indeed deflect the electron probe in a way consistent with the dynamics observed in Carbone's work [17]. The claims of Park *et al.*, however, were recently disputed [18-19]. In another graphite study by Raman *et al.*, performed under similar excitation conditions and using the same technique of UED, even larger amounts of shifts in the positions of the diffraction spots were reported, corresponding to 6% expansion of the interlayer distance at an excitation fluence of 40 mJ/cm² [16]. Raman *et al.* attributed the shifts partly to structural dynamics and partly to surface charging of the sample, and presented a model of the surface potential which was used to separate the two effects. It is evident from the forgoing survey of conflicting results that in order to settle the question of whether or not laser

excitation of graphite gives rise to non-thermal strains, an alternative approach to UED is warranted. To this end, here we investigate the structural dynamics of laser irradiated graphite using time resolved x-ray diffraction. X rays make an ideal structural probe in this context as they are insensitive to transient electric fields that may be generated at the surface of the sample.

The experiment was carried out at the Swiss Light Source (SLS). The FEMTO slicing beamline at SLS generates 120 fs x-ray pulses through laser-slicing of the electrons in the insertion device. The overall time resolution of the pump-probe scheme is dictated by the duration of the x-ray probe and laser pump pulses, the timing jitter of the laser system, and the geometrical mismatch angle between pump and probe beams. An overall time resolution of <200 fs has been demonstrated in several recent studies performed at this beamline (e.g. see Ref. [20]). The sample used in our study is a mined natural graphite flake, which was cleaved to produce a surface with high quality flatness. The single-crystalline nature of the sample was verified through static x-ray diffraction measurements carried out at beamline D611 at MAX-lab. For the time resolved measurements, the x-ray source was tuned to an energy of 5.85 KeV with ~1% bandwidth and focused to a spot size of $\sim 300 \times 10 \mu\text{m}$. To match the x-ray penetration depth with the optical absorption depth in graphite, we employ the noncoplanar diffraction geometry with extreme (near critical angle) grazing incidence shown in FIG. 1a. The grazing angle (φ_i) was set by first calculating the corresponding vertical displacement of the specularly reflected x-ray beam relative to the direct beam on a screen positioned at known distance from the sample. An avalanche photodiode (APD) was then placed at the set displacement and the intensity of the specularly reflected x-ray beam was maximized by varying φ_i . Measurements were conducted at two different grazing angles below (0.27°) and above (0.50°) the critical angle of 0.30° . The sample was excited at fluences ranging from $6\text{-}35 \text{ mJ/cm}^2$ with p-polarized 120 fs laser pulses

centered around 800 nm, and incident at 10° relative to the sample surface. The 0.75×4.5 mm footprint of the laser beam on the sample was sufficiently large to cover the 0.3×2 mm x-ray footprint, ensuring homogeneous excitation of the probed area. X-ray rocking curves were recorded at selected time delays in the -10 ps to +100 ps range, by measuring the intensity of the 101 reflection with an APD as function of the sample in plane rotation (θ_i). The respective repetition rates of the x-ray probe and laser pump pulses of 2 KHz and 1 KHz imply that every other x-ray pulse contributes to a reference (unpumped) signal. Figure 1b shows the 101 rocking curve of the unpumped sample at a grazing angle of 0.27° .

Results of time resolved measurements are shown in FIG. 2 in the form of rocking curve differences at selected time points both below (a-f) and above (g-l) critical angle and for an incident excitation fluence of 26 mJ/cm^2 . It is evident from the time-dependent shift of the rocking curves that the graphite lattice is strained. To explain the detailed shape of the curves, modeling of strain-wave propagation and x-ray scattering is needed. We employ the strain model proposed by Thomsen *et al.* [21] in which the laser-excited sample is assumed to develop instantaneous thermal stress of the form $-3B\beta\Delta T(z)$, where B is the bulk modulus, β is the linear expansion coefficient, and $\Delta T(z)$ is the temperature profile along the sample depth (z). The finite coupling time between electrons and lattice can be accounted for by considering the following time dependent temperature profile

$$\Delta T(z,t) = \frac{(1-R)F}{C\delta} [1 - \exp(-t/\tau)] \exp(-z/\delta),$$

where R is the reflectivity, F is the incident fluence, C is the volumetric heat capacity, δ is the optical absorption depth, and τ is the electron-phonon coupling time constant. When the finite coupling time is introduced, the analytical expression for the strain propagation given by

Thomsen *et al.* can no longer be used. Instead, the strain propagation is calculated numerically. The numerical solution of the relevant equations of elasticity is presented in FIG. 3a in the form of a spatio-temporal map of the *c*-axis strain. Note the maximum strain of ~2.5% at the surface corresponding to a ~1000 K temperature change and a *c*-axis thermal expansion coefficient of $27 \times 10^{-6} \text{ K}^{-1}$ [22]. An electron-phonon coupling constant of 8 ps was assumed [15-16]. In addition, we verified by solving the heat diffusion equation that the effects of heat diffusion can be neglected due to the relatively low thermal conductivity along the *c*-axis of graphite [23]. This assumption is also supported by Carbone's study in which following the initial drop in the diffracted intensity no significant changes are observed up to ~1 ns [15].

The spatio-temporal map of strain was used to create a deformed lattice structure of graphite, and subsequently calculate the x-ray diffraction intensity of the deformed structure using dynamical diffraction theory performed on the Stepanov X-ray Server [23]. The ~0.05° divergence of the x-ray beam was accounted for by performing simulations at different grazing angles and weight-averaging the results according to a Gaussian distribution of angles. The 1% bandwidth of the x-ray beam was also accounted for by convoluting the weight-averaged result with a voigt lineshape. The calculated rocking curve for zero strain (unpumped sample) is shown as solid line in FIG. 1b. Calculated rocking curve differences at selected time points are shown as solid lines in FIG. 2a-1. It is evident from the good agreement between measurements and calculations that the Thomsen model provides an accurate description of strain dynamics.

Qualitatively, the time-dependent features of the diffraction profiles can be understood as follows. Below critical angle, the x-ray absorption depth is less than the optical absorption depth of ~140 nm [4]. Strain is initially confined to the surface but evolves over time to mimic the

laser absorption profile. As strain waves propagate deeper into the material, more atomic layers become disturbed but the average strain within the disturbed region is reduced. This is clearly seen by comparing the strain profiles at 50 ps and 100 ps in FIG. 3b. With respect to x-ray diffraction, this simple picture explains both the increase in the intensity of the rocking curve difference with time and the monotonic shift towards smaller angles of the zero-crossing (intersection of rocking curve difference and x -axis) indicating reduced strain. We note that at these shallow angles, strain estimated directly from the raw data, as double the value of the zero-crossing [24], agrees well with calculated strain. The maximum amount of shift of the 101 rocking curve of 0.16° , observed at +10 ps, corresponds to a c -axis expansion of 2.4%. Another interesting feature of the dynamics is the asymmetric character of the rocking curve differences. This complex feature originates from the portion of the x-ray beam that by virtue of its large divergence penetrates deeper into the sample. Above critical angle, the x-ray absorption depth is much larger than the optical absorption depth. The rocking curve difference for these measurements loses the character of a simple shift of a diffraction peak with conserved amplitude and width. For these measurements, strain cannot be directly extracted from the raw data. Nevertheless, employing dynamical diffraction theory faithfully reproduces the observed features as evident in FIG. 2g-l.

A summary of the fluence dependent measurements is shown in FIG. 4 in the form of surface strain at +50 ps as function of incident fluence. Note that the deviation from linearity is similar in character to the saturation of the atomic mean square displacements above $\sim 20 \text{ mJ/cm}^2$ observed by Raman *et al.* [15]. We verified the nonlinearity cannot be attributed to a change in the optical reflectivity of the sample, since the measured reflectivity was found to be constant up to the damage threshold of $\sim 100 \text{ mJ/cm}^2$. However, we cannot rule out the possibility that the

saturation effect is related to an increase in the optical absorption depth with fluence. Evidence for such effect is implied from recent optical pump-probe measurements, in which laser excitation induced a transient increase in the transmittivity of graphene and graphite films [26-27].

We discuss our results in light of the recent UED studies of graphite [15-16]. Carbone *et al.* came to the conclusion of non-thermal strains based on an estimate of the temperature change of the sample of 40 K at 44.5 mJ/cm^2 and a thermal expansion coefficient of $7.9 \times 10^{-6} \text{ K}^{-1}$. First, we note that the relevant thermal expansion coefficient in all of these experiments is not the $7.9 \times 10^{-6} \text{ K}^{-1}$ of isotropic graphite but the $27 \times 10^{-6} \text{ K}^{-1}$ along the *c*-axis of natural graphite [22]. Second, we believe Carbone's estimate of temperature change to be significantly underestimated. Our estimate of temperature change of $\sim 1000 \text{ K}$ at 26 mJ/cm^2 and Raman *et al.* estimate of 950 K at 21 mJ/cm^2 suggest a temperature change of around 2000 K at 44.5 mJ/cm^2 . We note here that a 2000 K temperature change can explain the $\sim 50\%$ drop in the intensity of the 0014 reflection in Carbone's study in accordance with the Debye-Waller effect. Furthermore, Carbone *et al.* argues that the observed non-thermal strains are related to the excitation of the so called strongly coupled optical phonons (SCOP) [28-29]. However, the measured lifetime of SCOP, of 5-7 ps [28-29], does not support the persistence of non-thermal strains up to $\sim 1 \text{ ns}$ as observed in Carbone's work. Based on the above accounts, we believe that the $\sim 1.25\%$ positive strain in Carbone's study is purely thermal in nature. Another interesting feature of the UED studies is the detection of negative strains within picoseconds following excitation. The amount of *c*-axis contraction varies from $\sim 0.03\%$ in Carbone's study to $\sim 5\%$ in Raman's study. In our data, we see no clear evidence of a negative strain component. We have carried out additional simulations to set a limit on the lowest negative strain we can observe. Since the negative stress is short

lived, it gives rise to strain confined to the topmost ~ 5 nm of the sample. Given our surface sensitivity and the signal-to-noise ratio this negative strain component cannot be larger than 0.5% for the 26 mJ/cm^2 measurements.

In conclusion, our experiment supports the measurement of positive strains by Carbone *et al.* enforcing that these strains represent real structural dynamics. However, we disagree with the interpretation of the data suggesting that the observed strains point to a non-thermal contribution to the expansion of the lattice. To the contrary, we believe that the saturation effect in the atomic displacements in our experiment and in Raman's study indicate that the measured positive strains above 20 mJ/cm^2 are smaller than what is expected from thermal expansion. Finally, this work demonstrates time resolved x-ray diffraction in grazing geometry as a tool for resolving structural changes in light elements that do not efficiently scatter x-rays. The new generation of light sources, with their superior beam qualities, will have sufficient surface sensitivity to fully explore the contraction effect that is thought to be limited to the topmost few layers in graphite.

These experiments were performed on the X05LA beamline at the Swiss Light Source, Paul Scherrer Institut, Villigen, Switzerland. The authors thank the Swedish Research Council (VR), the Knut and Alice Wallenberg Foundation, the Crafoord Foundation, and the Carl Trygger Foundation for financial support. M. H. acknowledges financial support from the Natural Sciences and Engineering Research Council of Canada.

* jorgen.larsson@fysik.lth.se

[1] M. Freitag, *Nature Nanotechnology* **3**, 455 (2008).

- [2] A. Noya *et al.*, *Nano Today* **2**, 22 (2007).
- [3] G. W. Yang, and J. B. Wang, *Appl. Phys. A* **72**, 475 (2001).
- [4] A. Hu *et al.*, *Appl. Phys. Lett.* **91**, 131906 (2007).
- [5] A. V. Rode1, E. G. Gamaly, and B. Luther-Davies, *Appl. Phys. A* **70**, 135 (2000).
- [6] H. O. Jeschke, M. E. Garcia, and K. H. Bennemann, *Phys. Rev. Lett.* **87**, 015003 (2001).
- [7] A. Kaplan, M. Lenner, and R. E. Palmer, *Phys. Rev. B* **76**, 073401 (2007).
- [8] V. M. Pereira, and A. H. Castro Neto, *Phys. Rev. Lett.* **103**, 046801 (2009).
- [9] A. Rousse *et al.*, *Nature* **410**, 65 (2001).
- [10] A. M. Lindenberg, *et al.*, *Science* **308**, 392, (2005).
- [11] J. Larsson, *et al.*, *Appl. Phys. A: Mater. Sci. Process.* **75**, 467 (2002).
- [12] R. J. D. Miller *et al.*, *Acta Cryst. A* **66**, 137 (2010).
- [13] M. Harb *et al.*, *Phys. Rev. Lett.* **100**, 155504 (2008).
- [14] J. Cao *et al.*, *Appl. Phys. Lett.* **83**, 1044 (2003).
- [15] F. Carbone *et al.*, *Phys. Rev. Lett.* **100**, 035501 (2008).
- [16] R. K. Raman *et al.*, *Phys. Rev. Lett.* **101**, 077401 (2008).
- [17] H. Park, and J. M. Zuo, *Appl. Phys. Lett.* **94**, 251103 (2009); *Phys. Rev. Lett.* **105**, 059603 (2010).
- [18] F. Carbone *et al.*, *Phys. Rev. Lett.* **105**, 059604 (2010).
- [19] S. Schäfera, W. Lianga, and A. H. Zewail, *Chem. Phys. Lett.* **493**, 11 (2010).
- [20] S. L. Johnson *et al.*, *Phys. Rev. Lett.* **102**, 175503 (2009).
- [21] C. Thomsen *et al.*, *Phys. Rev. B* **34**, 4129 (1986).
- [22] E. A. Kellett, and B. P. Richards, *J. Appl. Cryst.* **4**, 1 (1971).

- [23] K. Sun, M. A. Stroschio, and M. Dutta, *Superlattices and Microstructures* **45**, 60 (2009).
- [24] <http://sergey.gmca.aps.anl.gov/>
- [25] Note that the distance between the maxima and minima of the rocking curve difference is an incorrect measure of the rocking curve shift. This can be easily verified by considering the difference between two Gaussian curves of equal amplitudes and widths shifted by an amount that is much less than the width.
- [26] L. M. Dawlaty *et al.*, *Appl. Phys. Lett.* **92**, 042116 (2008).
- [27] F. Carbone *et al.*, *Chem. Phys. Lett.* In Press (2011).
- [28] T. Kampfrath *et al.*, *Phys. Rev. Lett.* **95**, 187403 (2005).
- [29] H. Yan *et al.* *Phys. Rev. B* **80**, 121403 (2009).

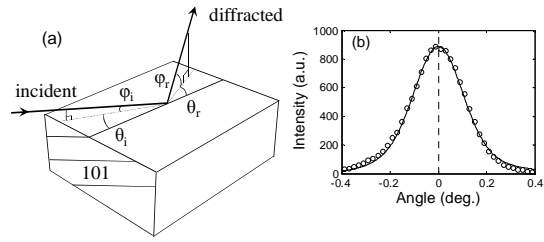


FIG. 1: (a) The noncoplanar diffraction geometry of the experiment. 5.85 KeV x-rays incident at a grazing angle of $<0.5^\circ$ relative to the surface of the crystal diffract off the 101 lattice planes. The diffracted beam is deflected by $\sim 62^\circ$ azimuthally ($\theta_i + \theta_r$) and by $\sim 18^\circ$ relative to the surface of the crystal (φ_r). (b) Measured (open circles) and calculated (solid line) rocking curve of the 101 reflection.

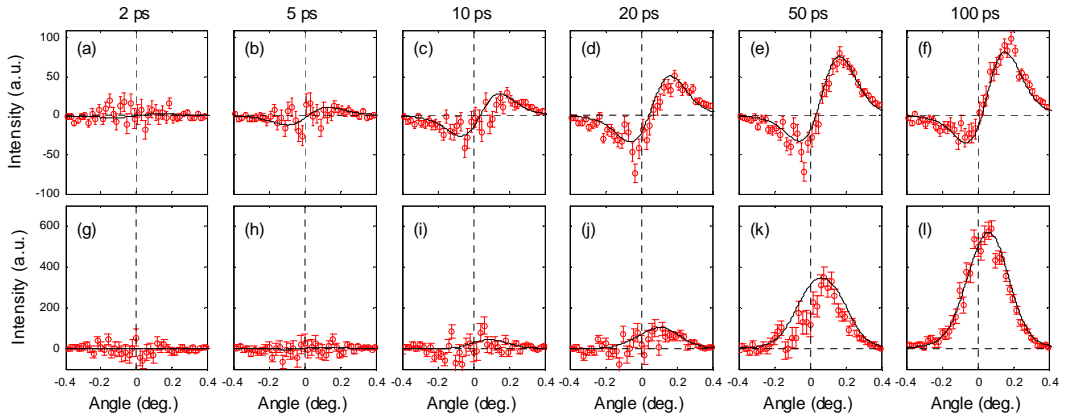


FIG. 2: Rocking curve differences taken at selected time delays relative to laser excitation at 26 mJ/cm^2 . Two sets of measurements were taken: panels a-f are at a grazing angle of 0.27° (below critical angle), and panels g-l are at a grazing angle of 0.5° (above critical angle). Open circles with error bars are experimental data points and solid lines are dynamical diffraction calculations of a thermally strained crystal.

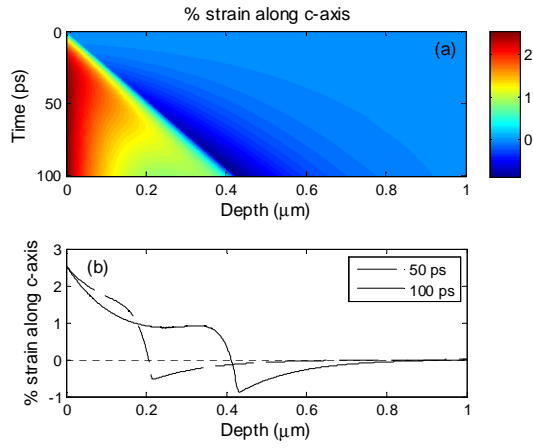


FIG. 3: (a) A spatio-temporal map of the % strain along c -axis of graphite excited at 26 mJ/cm^2 . The strain was numerically calculated according to the Thomsen model [21]. (b) Strain profile at +50 ps (dashed) and +100 ps (solid).

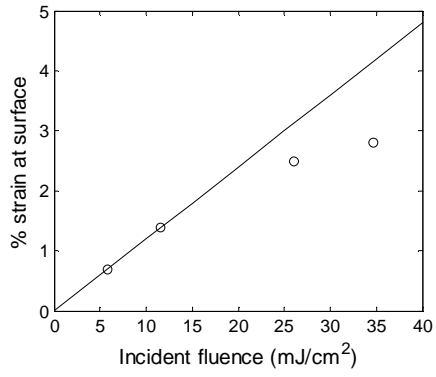


FIG. 4: Measured strain at +50 ps for experiments conducted at different excitation fluences.

Paper VIII

Time-resolved investigation of nanometre scale deformations induced by a high flux x-ray beam

J. Gaudin¹, B. Keitel², A. Jurgilaitis³, R. Nüske³, L. Guerin⁴, J. Larsson³, K. Mann⁵, B. Schäfer⁵, K. Tiedtke², A. Trapp¹, Th. Tschentscher¹, F. Yang¹, M. Wulff⁴, H. Sinn¹ and B. Flöter⁵

¹ European XFEL, Albert-Einstein-Ring 19, D-22761 Hamburg, Germany

² Deutsches Elektronen-Synchrotron, Notkestraße 85, D-22603 Hamburg, Germany

³ Department of Physics, Lund University, P.O. Box 118, 221 00 Lund, Sweden

⁴ European Synchrotron Radiation Facility, 6 rue Jules Horowitz, 38043 Grenoble, France

⁵ Laser-Laboratorium Göttingen, Hans-Adolf-Krebs-Weg 1, D-37077 Göttingen, Germany

E-mail: jerome.gaudin@xfel.eu

Abstract. Up-coming of a new generation of x-ray light sources, namely x-ray Free-Electron Lasers, puts new demanding constraints on the design of x-ray optics. The behaviour of optical devices, mainly mirrors, has to be carefully studied in order to take profit of the unique properties of these sources. In this article, we present results of a time-resolved pump-probe experiment performed at the ESRF ID09 beamline. We investigated the time behaviour of an optical substrate mimicking an x-ray mirror exposed to a high 15keV photon flux. Monitoring the wavefront deformation of an optical laser probe beam allowed measuring the build-up and relaxation of the x-ray induced nanometer heat bump. The results are compared to simulations based on finite element technique.

1. Introduction

Linear accelerator based lasers, so called Free Electron Lasers (FELs), are now becoming a reality as 4th generation x-ray light sources. Based on the SASE (Self Amplified Spontaneous Emission) process, they deliver ultra-short coherent light pulses. After the first successful development of FELs in the soft x-ray region at FLASH (Free-electron LASer in Hamburg [Intro1]), several hard x-ray facilities recently started (LCLS in Stanford [Intro2]) or are under construction (European XFEL in Hamburg and XFEL/SPRING8 in Japan).

The intrinsic properties of FEL beams open up new fields of research, putting, however, high constraints on the optics/beamline design. A key parameter is the wavefront, firstly since it determines the focusing properties of the beam [Intro3], and secondly because a highly distorted wavefront leads to similar effects as coherence loss [Intro4]. A wavefront sensor for soft x-ray radiation, developed for the special requirements of FLASH, was presented in [Intro5, Intro6] and successfully employed to reduce wavefront distortions from misaligned optical elements. However, in addition to alignment issues, both static and dynamic surface properties of the optical elements become more and more crucial when dealing with intense

Time-resolved investigation of nanometre scale deformation induced by high flux x-ray beam

hard x-ray wavelengths in the sub-nanometer range. It has been shown that for 0.1 nm radiation the surface quality should be better than 2 nm over a 800 mm long grazing incidence optics [Intro4]. While the manufacturing related static surface figure can be controlled with extremely high precision using interferometric techniques [Intro7], the in situ performance of FEL optics will also strongly depend on the performance under heat load.

High repetition rate FELs will deliver pulses at MHz rate within trains of a few hundred μ s. The heat load during such a bunch train can be as high as 60 W [Intro8], inducing transient deformations of the optics (mirrors as well as crystal monochromators). These deformations should be lower than the 2 nm value previously determined.

The deformation of x-ray optics under high heat load has already been addressed in the case of synchrotron optics. Measurements have been performed using different techniques, as, for instance, in situ long trace profilers [Intro9], or different types of Hartmann-Shack sensors [Intro10] [Intro11]. These measurements provided sub-micron resolution in terms of height deformation, but only under steady state load. On the other hand, some models have been developed [Intro12] to describe the specific case of a single FEL pulse, providing insight on the kinetics of the deformation. However, no results of time-resolved measurements were published so far. In this article, we report on such kind of time-resolved investigations in the case of a bunch train of x-ray pulses at MHz repetition rate. The experiment was performed at the ID09 beamline at the European Synchrotron Radiation Facility (ESRF). This beamline accomplishes both high x-ray flux and a dedicated set-up for time-resolved studies. The heat bump induced on an optical element was monitored by measuring the deformation of the wavefront of a reflected femtosecond optical laser. The wavefront measurement was performed using a highly sensitive Hartmann-Shack sensor, which had already been employed to monitor wavefront distortions due to thermal lensing in fused silica with sub-nm accuracy [Intro13]. Due to their high relative sensitivity and robustness, Hartmann-type measurements are well suited for photothermal measurements. Actually, the thermal distortion in a collimating objective was one of the very first applications Hartmann presented in his landmark paper on the new wavefront sensing technique in 1900 [Intro14]. Finally we used Finite Element Method (FEM) to model the experiments. This method is routinely used to predict behaviour of x-ray optics under static heat load [Intro15]. In this specific experiment the dynamics behaviour has also been modeled.

After a presentation of the experimental set-up and the measurement method (sect. 2) the procedure to retrieve the bump height from the measured wavefront is described (sect. 3).

Time-resolved experimental results obtained from Si substrate are compared to FEM simulations in sect. 5.

2. Experimental set-up and procedure

a. Description of the set-up

The experiment was performed at the ID09B beamline at the ESRF. This beamline provides quasi-monochromatic intense x-ray pulses (pulse width 50 ps) synchronized with a near infrared (NIR) femtosecond laser ($\lambda=780$ nm), delivering 1 mJ / pulse within 50 fs. The set-up allows performing pump-probe experiments where usually the optical laser represents the pump and x-ray pulses act as probe [SetUp1]. In our specific case a 82 μ s long bunch train of 120 x-ray pulses selected by a fast shutter was used as pump and a single NIR pulse as probe, both running at one kilohertz repetition rate. The experimental set-up is displayed in figure 1.

Figure 1

The undulators were tuned to deliver the peak intensity at 15 keV. The estimated energy per pulse from a calibrated photodiode was 2.7 μ J. The 82 μ s bunch train was focused at normal incidence onto the target within a spot of 125 μ m x 64 μ m (full width half maximum, as measured by a knife-edge scan) in order to maximize the photon flux on the sample. In order to improve its wavefront, the NIR laser beam was spatially filtered using a vacuum pinhole and attenuated to 5 nJ/pulse before reaching the sample. A spherical lens (focal length $f=25$ cm) focused the laser under an incidence angle of 41° onto the sample positioned in the divergent beam 4 cm behind the focal plane. The reflected NIR radiation was monitored by a Hartmann-Shack wavefront sensor located at a distance of 41 cm from the sample. The Hartmann-Shack sensor developed by Laser-Laboratorium Göttingen consists of a digital CCD camera (12 bit, 1280 x 1024 pixels) placed behind an array of plano-convex quartz micro-lenses ($f=40$ mm, pitch 0.3 mm). The camera was synchronized with the NIR pulse. The overall set-up was covered to avoid perturbations of the probe laser beam due to air flow. The experimental geometry introduced here, using a divergent test laser beam, enables the geometrical magnification of wavefront distortions which are laterally smaller than the microlens array pitch. Using a lensless setup behind the sample, the reconstruction of the sample surface profile relies on numerical methods only.

Time-resolved investigation of nanometre scale deformation induced by high flux x-ray beam

The sample consists of a super smooth Si substrate (flatness $\lambda/10$ @ 633 nm, rms roughness 1 Å) coated with a 100 nm thick layer of Platinum. At normal incidence the Platinum coating absorbs 3 % of the incoming radiation, hence being almost transparent for the x-rays. However, the metallic coating acts as a perfect mirror for the NIR laser, avoiding heating of the sample by the test laser beam.

b. Measurement procedure

Before performing the experiment, both spatial and temporal overlap of the pump and probe beams had to be accomplished. Spatial overlap was primarily checked by an optical microscope monitoring the sample surface, making use of the fact that the x-ray flux was high enough to excite luminescence from the platinum coating. The scattered light of the NIR laser, also visible on the microscope, was then simply directed to the position of this luminescence. A fine-adjustment was achieved in an iterative way by monitoring the Hartmann-Shack sensor signal, centering precisely the laser spot on the heat bump. The time delay between x-ray and laser pulse was controlled electronically using a delay generator which shifted the phase of the laser oscillator feedback loop. Temporal overlap at the sample position was obtained monitoring the photodiode signals.

The wavefront distortion measurement was performed in two steps: first the test laser wavefront and intensity pattern were measured at the sensor position without heat load on the sample (non-distorted test beam). Thereafter, a train of 120 x-ray pulses was directed onto the sample, and the delayed NIR pulse reflected from the heated zone of the surface was registered by the Hartmann-Shack sensor at one kilohertz repetition rate (distorted test beam). For each delay 64 camera frames of 25 ms each were recorded and averaged, optimized according to the wavefront stability of the fs laser system. Thus, each wavefront and beam profile reconstruction contains information from 1600 x-ray bursts. After this measurement of the distorted beam, another record of the non-distorted beam was taken to check the remaining wavefront, giving a measure for the confidence level. The procedure was repeated for each delay time.

3. Wavefront and surface profile reconstruction

An absolute wavefront calibration is obtained from a plane wave reference, making use of a 50x expanded HeNe laser. The displacement of the foci produced by the microlens array (21x19 spots) from their reference positions yields the wavefront gradient, from which the

Time-resolved investigation of nanometre scale deformation induced by high flux x-ray beam

wavefront is computed by fitting a set of Zernike polynomials (up to 6th order in the radial coordinate) [Rec01] in a least squares approach. The wavefront reconstruction is described in greater detail in [Rec02] and the Hartmann-Shack sensor in [Rec03].

The surface topology of the sample is computed from the measured wavefronts as follows. We define a mirror coordinate system Σ which is described by the coordinates (ξ, η, ζ) , where $\zeta=0$ is the mirror surface. Let the plane of incidence be given by the ξ and ζ directions and let α be the angle of incidence of the test laser beam. The wavefront sensor-coordinate system S is described by the coordinates (x, y, z) , where the z-axis is the optical axis of the test laser beam after reflection and $z=0$ defines the detector plane. S follows from Σ by a rotation around the η -axis by $-\alpha$ followed by a translation along ζ by the distance L from the mirror to the detector, measured at the beam center.

The scalar complex amplitude of the laser beam after reflection from the sample surface is given by

$$U(\xi, \eta, 0) = U_i(\xi, \eta, 0)T(\xi, \eta) \quad (1)$$

where U_i is the complex amplitude of the incident test laser beam and $T(\xi, \eta)$ the complex phase factor imposed by the sample surface. Since the surface height deviation is small compared to the wavelength and the divergence is moderate, we can use

$$T(\xi, \eta) = \exp(-2ik \cos(\alpha) \delta h(\xi, \eta)) \quad (2)$$

with the wave vector k of the test laser beam and the local surface height deviation from the non-distorted surface $\delta h(\xi, \eta)$.

Employing Huygens-Fresnel principle [Rec01] and neglecting the inclination factor, we write

$$U(x, y, 0) = -\frac{i}{\lambda} \iint d\xi d\eta U(\xi, \eta, 0) \frac{\exp(ikR)}{R} \quad (3)$$

The squared distance $R^2(\xi_0, \eta_0, x_0)$ for a given point $\xi_0 = (\xi_0, \eta_0, 0)$ on the mirror surface (in Σ) and point $\mathbf{x}_0 = (x_0, y_0, 0)$ in the detector plane (in S) is

$$R^2 = (x_0 - \xi_0 \cos \alpha)^2 + (y_0 - \eta_0)^2 + (L - \xi_0 \sin \alpha)^2 \quad (4)$$

R is expanded up to second order in ξ/z and x/z in the exponential and we use $L \approx R$ in the denominator. This yields the Kirchoff-Fresnel-like propagation operator \mathbf{F} for paraxial, quasi-monochromatic coherent beams, adapted for tilt. The back propagation onto the surface is given by $\hat{U}(\xi, \eta, 0) = \mathbf{F}^{-1}(U(x, y, 0))$ with the inverse operator

$$\hat{U}(\xi, \eta, 0) = \mathbf{F}^{-1}(U(x, y, 0)) = \frac{i \cos \alpha}{\lambda L} e^{-ikL} \exp\left(-\frac{ik}{2L}(\xi^2 \cos^2 \alpha + \eta^2)\right) \times \iint dx dy U(x, y, 0) \exp\left(-\frac{ik}{2L}(x^2 + y^2)\right) \exp\left(\frac{ik}{L}(x\xi \cos \alpha + y\eta)\right) \quad (5),$$

where \hat{U} is the complex amplitude less tilt terms.

The phase factor follows from the ratio of the distorted and the non-distorted complex amplitude in the sample plane,

$$T(\xi, \eta) = \frac{\mathbf{F}^{-1}(U_{\text{distorted}}(x, y, 0))}{\mathbf{F}^{-1}(U_{\text{non-distorted}}(x, y, 0))} \quad (6)$$

where the intensities $U_{\text{distorted}}$, $U_{\text{non-distorted}}$ are non-zero.

The integral (5) was solved on a 1500 x 1500 square grid using a Fast Fourier Transform (FFT) algorithm, representing the circular evaluation area (2.85mm radius) of the Hartmann-Shack sensor. The intensity between the individual spots on the CCD was interpolated by bicubic splines.

4. Results

After spatial filtering, the probe laser's wavefront at the Hartmann-Shack sensor position showed a remaining wavefront root-mean-square (w_{rms}) of about 20nm relative to the HeNe reference. Figure 2a shows the shot-to-shot fluctuations of 3.6nm w_{pv} . The relative wavefront of the distorted and non-distorted beam is shown in figures 2b and 2c for a delay of 82 μ s (at the end of the x-ray burst) and 122 μ s. Wavefront peak-to-valley (w_{pv}) at the sensor position grows for each pulse in the x-ray burst up to approximately 24nm. The mean stability of the reference wavefront was determined as described in section 2b and we found 2.1nm w_{pv} with standard deviation 1.1nm.

Figure 2

The wavefront distortion at the sensor position is broader than the distortion on the sample surface due to both diffraction and divergence of the probe laser beam. Thermal distortions for the delays 82 μ s and 122 μ s are plotted in figures 3a and 3b. The actual surface deformation (figures 3a, 3b) shows a Gaussian profile, which corresponds to the lateral dimensions of the x-ray spot and a broader background.

The amplitude of the distortion is determined by fitting a Gaussian function of the form

$$h(\xi, \eta; h_0, h_1, \beta, \xi_0, \eta_0) = h_0 + h_1 \exp\left(-\frac{\xi'(\beta, \xi_0)^2}{2\sigma_\xi^2} - \frac{\eta'(\beta, \eta_0)^2}{2\sigma_\eta^2}\right) \quad (7)$$

where $\xi'(\beta, \xi_0)$ and $\eta'(\beta, \eta_0)$ are the lateral coordinates on the sample surface which allow for decentring (ξ_0, η_0) and rotation (β) in the plane. A cross section along the η -axis is plotted in figure 3c for both the best-fit curve and the computed surface profile. Averaging the bump width over the delays from 0 μ s to 180 μ s yields 127 μ m for ξ' and 72 μ m for η' (FWHM), showing that the lateral extension of the central distortion corresponds to the size of the x-ray focal spot size.

Figure 3.

Finally the bump height (fit parameter h_1) is plotted against the delay in figure 4. We find an exponential decay constant of 31.1 ± 6 μ s, the error bar corresponding to the confidence interval of the fit.

Figure 4

5. FEM modelling

Finite elements simulations were performed to model the experimental conditions. The sample was modelled by a quarter of cylinder of 300 μ m radius and 600 μ m thick as shown in figure 5. We model two cases: one with the bare Si substrate and the same substrate with a 100 nm Pt coating. The heat load was simulated using a 2 dimensional Gaussian distribution reproducing the x-ray beam profile. The profile along the propagation direction follows a

Time-resolved investigation of nanometre scale deformation induced by high flux x-ray beam

regular exponential decay law. The absorbed power per unit of volume P can then be written as follow:

$$P(W \cdot cm^{-3}) = P_0/V \cdot \exp\left(-\frac{x^2}{2\sigma_x^2} - \frac{y^2}{2\sigma_y^2}\right) \cdot \exp\left(-\frac{z}{l_{abs}}\right) \quad (8)$$

Where p_0 is the average power over a full bunch train equal to 3.72 W, $V = \pi\sigma_x \sigma_y l_{abs}$ is the volume where the absorption takes place $\sigma_x=53.2 \mu\text{m}$ and $\sigma_y=27.2 \mu\text{m}$ are the rms value of the Gaussian profile calculated from the FWHM of the measured x-ray spot, and $l_{abs} = 442 \mu\text{m}$ is the absorption depth at 15 keV in Si. In the case of a coated sample, we considered a constant load profile corresponding of 3% of absorption and the same heat load profile in the Si substrate. The relevant thermo-dynamical constants used for the simulation are given in the table 1. As the substrate is monocrystalline, with the surface being oriented along the (111) direction, the constants are then chosen accordingly to the relevant direction from ref [Fem1]. Thin metallic coating are usually polycrystalline, hence we used non dependant direction values. For both materials these values were kept constant as the temperature variation is very weak, as shown in the figure 5.

	Density g/cm ³	Poisson coefficient	Young modulus GPa	Thermal expansion 10 ⁻⁶ /°C	Thermal conductivity W/m°C	Specific heat J/g.°C
Si (111)	2.34	0.26	187	2.56 10 ⁻⁶	163.3	0.703
Pt	21.4	0.36	275	9.0 10 ⁻⁶	71.6	0.133

Table 1 : Thermo-dynamical constants of Si (111) and Pt used in the FEM model.

This figure shows the simulated volume with colour map showing the temperature at the end of the x-ray pulse train corresponding to the maximum bump height in the case of the coated sample. The maximum temperature rise is equal to 9.2K in case of non coated Si and 11.3K for the coated substrate. The maximum displacement is found to be 3.9 nm for the bare substrate and 4.2 nm for the coated substrate. This shows the very weak effect of the coating due to the low absorption of the thin layer. Nevertheless as Pt has a larger thermal expansion, the height of the bump is a slightly larger.

The figure 6 shows the time dependence of this displacement. The time constant for the decay can also be retrieved assuming an exponential decay. The decay constants are then $41.6 \mu\text{s}$ for the bare Si substrate and $40.4 \mu\text{s}$ for the coated Si substrate. Once again the influence of the coating appears to be weak. As can be guessed from the figure 5 the heat gradient is much higher in the radial direction than along the depth. The heat flux is taking place primarily in the radial direction, which leads to the first fast decay of the heat bump. On a longer time scale as the temperature gradient decreases, the heat flux also slow down inducing a long decay of the bump. The simulation has been run until a delay corresponding to $300 \mu\text{s}$. The figure 6 clearly shows that at this delay the heat bump on the substrate has not yet completely disappeared.

Figure 5

Figure 6

6. Discussion and Conclusion

The experiment and the FEM simulations give results in the same order of magnitude in terms of bump height and time constant. Nevertheless there is a noticeable difference between the height of the bump experimentally measured and the one obtained with FEM simulations. This difference can be explained by the high repetition rate of the bunch train. As shown by the FEM results the bump firstly decreases rapidly within 30 to $40 \mu\text{s}$ and then relaxes slowly. Further FEM calculations shows that after 1 ms the bump height is still in the range of 0.5 nm. As described in the section 2, the measurement procedure is done such that the wavefront is averaged over 25 ms, i.e. 25 bunch train at a kilohertz. The broad background, which is present in our measurement but too large to be correctly evaluated and subtracted explain the discrepancy between model and experiment. On the other hand the agreement of the time constant is quite good and reflect the behaviour of heat dissipation largely dependant of the temperature gradient, i.e. the intensity profile of the beam.

In this experiment we have measured the dynamics of a deformation in the nanometer range induced by a bunch train of x-ray pulses. We have shown that the deformation can be modelled with FEM simulations in a reasonable manner. Our results clearly show that nanometre scale deformation can be measured quite accurately which paves the way to practical applications and to further developments. As this technique is robust and easy to implement it can be used for in-situ measurements providing real time deformation of the surface. Moreover as underlined in reference [Intro7], due to the high energy per pulse (in the

Time-resolved investigation of nanometre scale deformation induced by high flux x-ray beam

mJ range) a single pulse of FEL can lead to the deformation of the optic relaxing a nanosecond time scale. It is then questionable if in the case of high repetition rate facility the optical surface can be deformed from pulse to pulse. This fast process could then be studied with the technique we presented here. Apart from the obvious technical interest, more fundamental questions on the behaviour of materials under non equilibrium condition would be addressed and answered.

Acknowledgements

We acknowledge the support from Deutsche Forschungsgemeinschaft within SFB755 “Nanoscale Photonic Imaging”.

References

- [Intro1] Ackermann W et al 2007 *Nat. Photonics* **1** 336
- [Intro2] Emma P et al 2010 *Nat. Photonics* **4** 641
- [Intro3] Barty A et al 2009 *Opt. Express* **17** 15508
- [Intro4] Geloni G et al 2010 *New. J. Phys.* **12** 035021
- [Intro5] Flöter B et al. 2010 *New J. Phys.* **12** 083015
- [Intro6] Flöter B et al. 2010 *Nucl. Instr. and Meth. A* *in press*
Doi:10.1016/j.nima.2010.10.016
- [Intro7] Siewert F et al. 2010 *Nucl. Instr. and Meth. A* **616** 119
- [Intro8] Sinn H et al. 2010 *Proc. of the 32nd FEL Conference Malmö*, <http://srv-fel-0.maxlab.lu.se/TOC/THOCII.PDF>
- [Intro9] Quian S et al 1997 *Appl. Opt.* **36** 3769
- [Intro10] Susini J et al 1995 *Rev. Sci. Instrum.* **68** 2048
- [Intro11] Revesz P and Kazimirov A 2010 *Synchr. Rad. News.* **23** 1
- [Intro12] de Castro ARB, Vasconcellos Ar and Luzzi R 2010 *Rev. Sci. Instrum.* **81** 073102
- [Intro13] Schäfer B, Gloger J, Leinhos U and Mann K 2009 *Opt. Express* **17** 23025
- [Intro14] J. Hartmann, *Z. Instr.* 1900 **20** 47–58.
- [Intro15] Zhang I et al. 2001 *Nucl Instr Meth A* **467** 409
- [SetUp1] Ihee H et al 2009 *Chem Phys Chem* **10** 1958
- [Rec01] M. Born, E. Wolf, *Principles of Optics*, 6th ed., Cambridge University Press, Cambridge, 1985.
- [Rec02] D. R. Neal et al. 1996 *Proc. SPIE* **2870**, 72
- [Rec03] B. Schäfer, and K. Mann, 2000 *Rev. Sci. Instrum.* **71**, 2663
- [Fem1] Wortmann JJ, Evans RA 1965 *Jour. Appl. Phys.* **36** 153

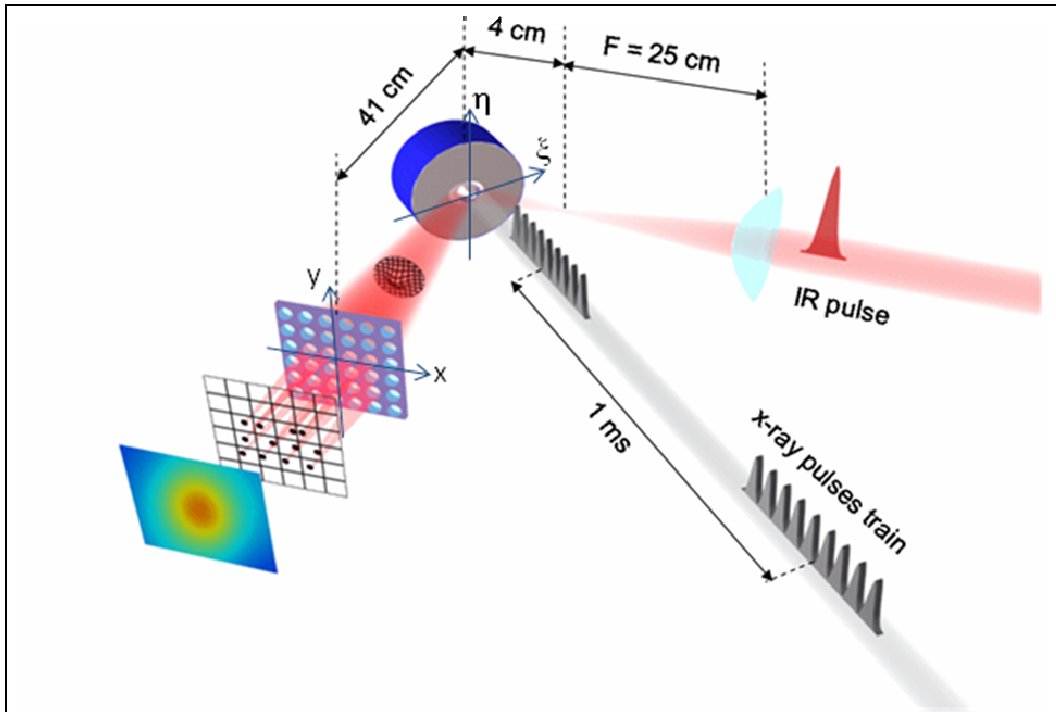


Figure 1: Schematic view of the experimental set-up

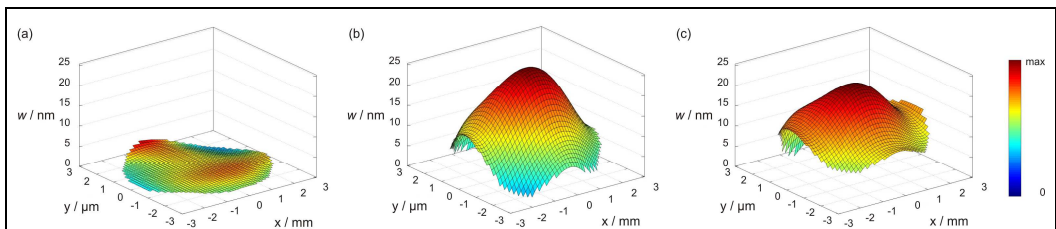


Figure 2. (a) shows residual fluctuations in the wavefront of the test laser beam ($3.6\text{nm } w_{pv}$). The thermally induced wavefront distortion of the test laser at the sensor position is shown in (b) for a delay of $82\mu\text{s}$ ($23.9\text{nm } w_{pv}$) and in (c) for a delay of $122\mu\text{s}$ ($17.7\text{nm } w_{pv}$).

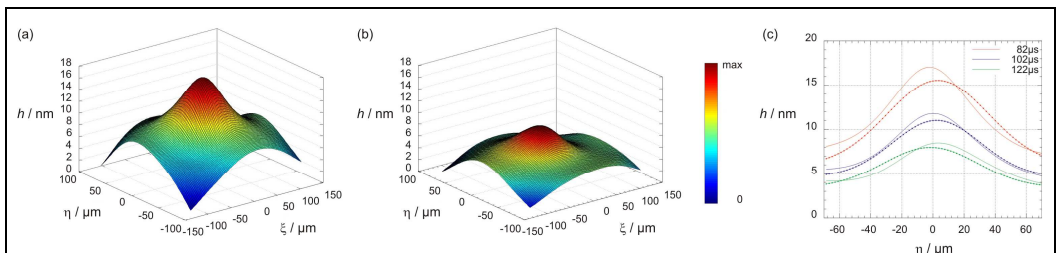


Figure 3. (a) shows the reconstructed surface topology from wavefront measurements for a delay of $82\mu\text{s}$ (peak-to-valley (pv) 17nm) and (b) for a delay of $122\mu\text{s}$ (pv 8.6nm). The surface profiles correspond to the wavefronts shown in figure 2 (b) and (c). Figure (c) shows a crosssection of the surface profile along the η axis (solid lines) together with the three-dimensional Gaussian fit curve (dash-dotted).

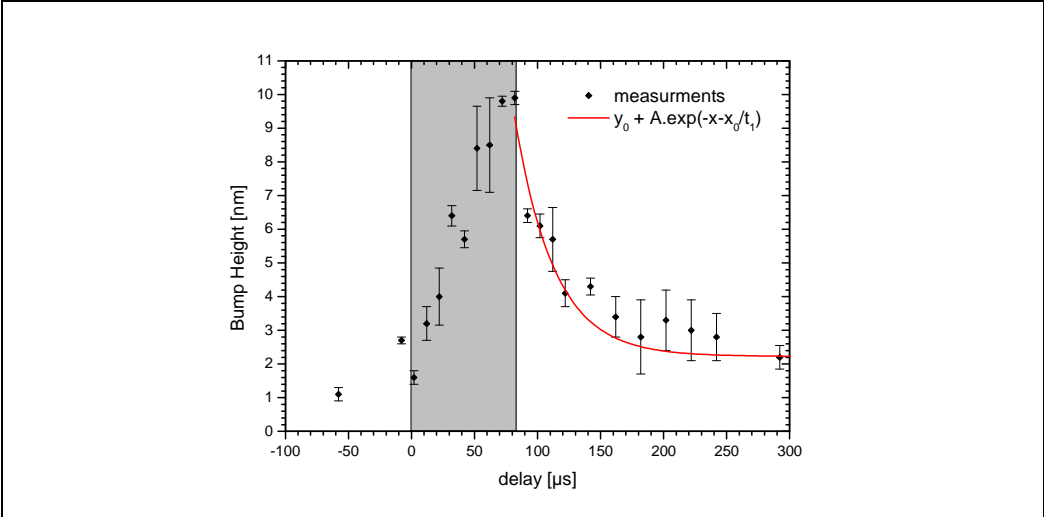


Figure 4. Heat bump dynamics form wavefront measurement. The red line is the exponential decay used to fit the experimental points [$t_1=31.1 \mu\text{s}$].

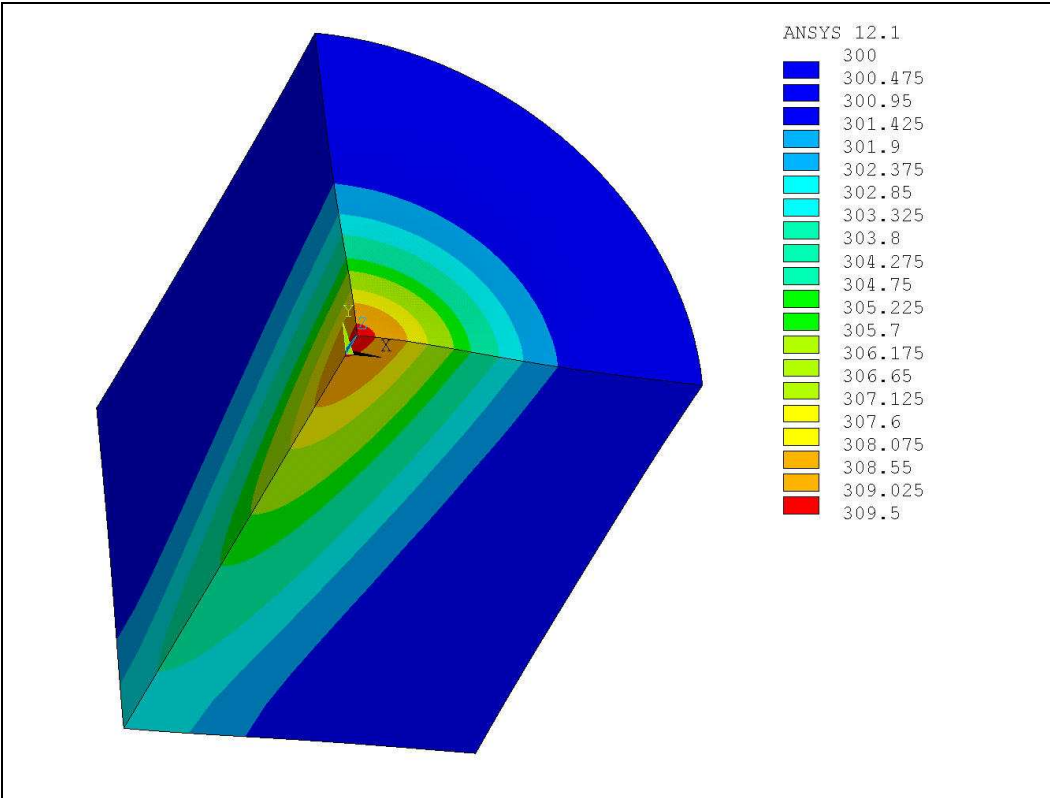


Figure 5: Simulated volume with the FEM. The color shows the temperature at the end of the x-ray pulse train. The picture corresponds to the Si bare substrate.

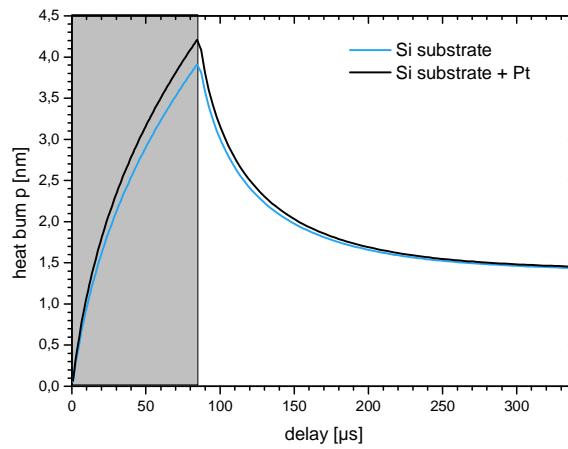


figure 6: Height of the surface point at the center of the simulated volume as a function of time resulting from FEM simulations. The blue curve is for the Si substrate and the black on for the Si + Pt coating.

Part III

Appendix - Matlab scripts

1D heat flow simulation of melting-resolidification

```
%++++++material parameter of InSb++++++
xi = 140E-9; % Penetrationdepth in m
d1 = 60E-9; % initial melt in m
delta_d = 150E-9; % thickness of latent heat layer in m

specificHeat = 293; % J/(kg K)
Density = 5.8e3; % kg/m^3
Enthalpie_m = 1.32e9; % latent heat J/m^3
conductivity = 4.57; % J/m-K-s
k=conductivity/Density/specificHeat; % m^2/s

meltingpoint=800;
offset=800-meltingpoint;

%++++++world creation++++++
s1 = 0; % begin of sample
size=1500E-9; % m
nx=1500; % no of points
dx=size/nx; % m
x=linspace(0,size,nx);
range=200E-9; % s
stop=200E-9;
timesteps=2000000; % no of timesteps
dt=range/timesteps; % s
tmod=100;
time=linspace(0,range,int32(timesteps/tmod));
e = ones(nx,1);
A = spdiags([e -2*e e], -1:1, nx, nx);
A(1,1)=-1;
A(nx,nx)=-1;

%++++++initial condition at t=0++++++
%temperature
T1 = (x>=s1).*(x<s1+d1).*
    meltingpoint/exp(-(s1+d1)/xi).*exp(-x./xi);
T2 = (x>=(s1+d1)).*(x<(delta_d+d1+s1))*meltingpoint;
T3 = meltingpoint/exp(-(s1+d1+delta_d)/xi).*exp(-x./xi).
*(x>=delta_d+d1+s1);
T = T1+T2+T3;
T=T.';
%latent heat
Q1=Enthalpie_m;
C1=Enthalpie_m/(1-exp(-delta_d/xi));
C2=C1-Q1;
Q=(x>=s1).*(x<(s1+d1)).*Q1 + (x>=(s1+d1)).*
(x<(delta_d+d1+s1)).*(C1*exp(-(x-d1)/xi)-C2);
Q=Q.';
%++++++
figure(1);
t=0;
c1=k/(dx^2)*dt;
c2=conductivity/(dx^2)*dt;
counter2=0;
molten=zeros(int32(timesteps/tmod),1);
```

```

for counter=1:timesteps
    t=t+dt;
    test=0;
    test2=0;
    testn=0;
    n1=0;
    n2=0;
    for i=1:nx          %search for liquid-solid interface
        if ((T(i)==meltingpoint) & (test==0)) % found at n1
            n1=i-1;
            test=1;
        end;
        if ((T(i)<meltingpoint) & (test==1))
            n2=i-1;
            test=0;
        end;
        if ((T(i)<meltingpoint) & (test2==0))
            testn=i-1;
            test2=1;
        end;
    end;
    if n2>(n1+1)
        dQ=c2*(T(n1)-T(n1+1));
        Q(n1+1)=Q(n1+1)+dQ;          % change in latent
                                    % heat at interface
        if Q(n1+1)>Enthalpie_m      % continued melting
            n1=n1+1;
        end;
        dQ=c2*(T(n2+1)-T(n2));
        Q(n2-1)=Q(n2-1)+dQ;        % change in latent
                                    % heat at interface
        if Q(n2-1)<0                % resolidification
            n2=n2-1;
        end;

        e1=ones(n1,1);
        e2=zeros(n2-n1,1);
        e3=ones(nx-n2,1);

    else
        n1=testn;
        dQ=c2*(T(n1+1)-T(n1));      % change in latent
                                    % heat at interface
        Q(n1)=Q(n1)+dQ;            % resolidification
        if Q(n1)<0
            n1=n1-1;
        end;

        e1=ones(n1-1,1);
        e2=zeros(1,1);
        e3=ones(nx-n1,1);

    end;
    %+++++calculate diffusion matrix+++++
    K=c1*spdiags([e1;e2;e3],0,nx,nx)*A;

```

```

%+++++calculate new temperature profile+++++
T=T+K*T;

if mod(counter,tmod)==0
    counter2=counter2+1;
    molten(counter2)=dx*1E9*n1;
    subplot(3,1,1);
    plot(x*1E9,T+offset);    % plot temperature profile
    xlabel('x [nm]');
    ylabel('T [K]');
    axis([0 500 0 1100]);
    title(strcat('t=',num2str(t*1E9),'ns'),'FontSize',18);
    subplot(3,1,2);
    plot(x*1E9,Q);          % plot latent heat profile
    xlabel('x [nm]');
    ylabel('latent heat [J/m^3]');
    axis([0 500 0 1.5E9]);
    subplot(3,1,3);
    plot(time*1E9,molten);  % plot thickness of melt
    xlabel('t [ns]');
    ylabel('molten layer [nm]');
    drawnow;
end;
if t > stop
    break;
end;
end;

```


Specular thin film x-ray reflectivity

```
%+++++++ reading data ++++++++
for j = 1:size(tearly,2)
    [header,test] =
        mhdrload(strcat(DataDirectory, prefix, tearly{j}),
            suffix, '.txt');
    Data{j} = [test(:,2), test(:,5)]; % 2 columns: angle, reflectivity
end;

%+++++++ initial guesses ++++++++
angle_offset=-1E3;
I0=1.4E-6;
density=1.99;
dc_offset=3E-9;
thickness=46.5E-9;
sigma1.0E-10;
nsmooth=3;

%+++++++ creating fits ++++++++
timesteps=size(tearly,2);
r=zeros(size(tearly,2),size(Data{1})(:,1));

figure(1);
hold on;
for j = 1:timesteps % loop over all timesteps
    X = Data{j}(:,1); % measured data (angle)
    Y = Data{j}(:,2); % measured data (intensity)

% ++++++++ initial guess ++++++++
fitparams0 = [angle_offset I0 density dc_offset thickness sigma];

%+++++++ determine parameterset using nonlinear regression ++++++++
[fitparams,r(j,:),J] = nlinfit(X', log(Y'), @R_form2, fitparams0);

ci{j} = nlparci(fitparams,r(j,:),J) % fit results

dphi=fitparams(1)*180/pi
dlogY=-log(fitparams(2))

XFIT = X';
YFIT = R_form2(fitparams, XFIT);

subplot(2,2,1)
plot(X+dphi, CdB*(log(Y)+dlogY), plotColors{j});
% plotting measured reflectivity
hold on;
plot(XFIT+dphi, CdB*(YFIT+dlogY), plotColors_sim{j});
% plotting fitted reflectivity
test=ci{j};
result_amplitude(j)=test(2);
result_density(j)=test(3);
```



```

    result_thickness(j)=test(5);
    result_sigma(j)=test(6);
end;

%+++++++ Plotting fitting results ++++++++
xlabel('\theta [\circ]');
ylabel('log(I/I_0)');
axis([min(X+dphi) max(X+dphi) -30 5]);
title(strcat(['Time resolved reflectivity of a-C @ ',
              ParametersFile(10:13), '/cm2']));
legend(T);
hold off;
subplot(2,2,2);
plot(TIME,result_sigma*1E9);
hold on;
axis([-1 10 min(result_sigma*1E9) max(result_sigma*1E9)]);
xlabel('delay time [ns]');      % plotting roughness(TIME)
ylabel('roughness [nm]');
title('Reflected intensity below critical angle');
subplot(2,2,3);
plot(TIME,result_density);      % plotting density(TIME)
hold on;
axis([-1 10 min(result_density) max(result_density)]);
xlabel('delay time [ns]');
ylabel('density [g/cm^3]');
title('Carbon density');
subplot(2,2,4);
plot(TIME,result_thickness*1e9); % plotting thickness(TIME)
hold on
axis([-1 10 min(result_thickness*1e9)
      max(result_thickness*1e9)]);
xlabel('delay time [ns]');
ylabel('thickness [nm]');
title('carbon thickness')

%+++++++function calculating reflectivity ++++++++
function Y = R_form2(params, X); % params: 1=angle_offset
% % % % % % % % % 2=I0 3=density 4=dc_offset 5=thickness 6=sigma

energy=18000; lambda = Energy2lambda(energy);
k0=2*pi/lambda;
n_film = XrayIndexOfRefraction('C', params(3), energy);
      % refractive index of film
n_substrate = XrayIndexOfRefraction('Si', 2.33, energy);
      % refractive index of substrate

%+++++ calculating beam angles
x1 = pi/2-X*pi/180 - params(1);
x2 = asin(sin(x1)*1/n_film);
x3 = asin(sin(x2)*n_film/n_substrate);

%+++++ and wavevector - z-components
k1=cos(x1)*k0;
k2=cos(x2)*k0;
k3=cos(x3)*k0;

```

```

%++++ debye-waller factor describing roughness
r = exp(-k1.*k1*(params(6)^2));

%+++++ phase change in thin film
phase=k2*params(5);

%+++++ setting up matrices
for i=1:size(X);
    R0(:,i)=[k1(i)-k2(i) k1(i)+k2(i) ; k1(i)-k2(i) k1(i)+k2(i)]/(2*k1(i))*r(i);
            % reflection matrix 1

    T1(:,i)=[exp(i*phase(i)) 0 ; 0 exp(-i*phase(i))];
            % propagation matrix

    R1(:,i)=[k2(i)-k3(i) k2(i)+k3(i) ; k2(i)-k3(i) k2(i)+k3(i)]/(2*k2(i));
            % reflection matrix 2

    R(:,i)=R0(:,i)*T1(:,i)*R1(:,i);
            % total matrix

    reflectivity(i)=abs(R(1,2,i)/R(2,2,i))^2;
            % the absolute reflectivity
end;

Y = log(params(4) + params(2)*reflectivity)
    % reflectivity (log scale)
%+++++

```


Analysis of x-ray powder diffraction with detector under oblique angle

```
%+++++++loading powder diffraction data+++++++
path='Z:\ANDOR_CAM\20100126\';
filename='calib.tif';
picture=imread([path filename]);
energy=7; %keV

%+++++++ detector definitons+++++++
center=[458 372 201.72]; %direct beam
cropping=[ 170 750] [410 640] ];
alpha=53*pi/180; %detector angle

%+++++++making q-map for all pixels of detector+++++++
q_space=zeros(1004,1002);
clear s;
for m=cropping(1,1):cropping(1,2)
for l=cropping(2,1):cropping(2,2)
a=m-center(1); %distance in z
b=-(l-center(2))*cos(alpha); % y
c=-(l-center(2))*sin(alpha)+center(3); % x
r=sqrt(a^2+b^2+c^2); %absolute distance
q_space(l,m)=1.0136*energy*sin(acos(c/r)/2);%q
end;
end;

%+++++++binning the data according to their q-value+++++++
q=linspace(0,4.5,101);
for n=1:(length(q)-1)
mask=(q_space<q(n+1)).*(q_space>q(n));
weight=sum(sum(mask));
s(n)=sum(sum(double(picture).*mask));
end;

%+++++++plotting+++++++
figure(1);
imagesc(picture); % measured data
figure(2);
imagesc(q_space); % q-map for detector
figure(3);
plot(q(1:(end-1)),s); % I(q)
```

